Determination of point proton radii of neutron-rich carbon isotopes

by

Pranav Subramaniyam

Submitted in partial fulfillment of the requirements for the degree of Doctor of Philosophy in Applied Science

at

Saint Mary's University
Halifax, Nova Scotia
October 2022

Approved: _____
Prof. Rituparna Kanungo
Supervisor

Approved: _____
Prof. Luigi Gallo
Committee member

Approved: _____
Prof. Greg Christian
Committee member

Approved: _____
Prof. David Hornidge
External Examiner

Date: October 20, 2022

Contents

List of Figures

List of Tables

Abstract

Determination of point proton radii of neutron-rich carbon isotopes
Pranav Subramaniyam

Exotic features like the halo and the (dis)appearance of the magic numbers were revealed by investigating the nuclei towards the neutron-rich region that have a large neutron/proton asymmetry. Investigating the evolution of proton radii together with the matter radii along an isotopic chain will allow us to characterize the halo formation, neutron skin thickness, and shell evolution around the neutron drip-line. The first determination of the point proton radii of neutron-rich carbon isotopes ^{20,22}C is presented in this work. The proton radii of these neutron-rich carbon isotopes were determined from a measurement of the charge-changing cross-section σ_{cc}, defined as the sum of cross sections of reactions that changes the atomic-number (Z). The experiment was performed at the BigRIPS facility at RIKEN Nishina Center in Japan, at a relativistic beam energy around $\sim 200A$ MeV with a carbon target. The proton radii were extracted from the measured σ_{cc} using the finite range Glauber model framework. The proton radii increase for ^{20}C and ^{22}C compared to the previously measured carbon isotopes $^{12-19}$C, showing signatures of the disappearance of shell closures at N =14 and N = 16 along this isotopic chain. The neutron skin thickness (ΔR_{np}) of these neutron-rich carbon isotopes (^{20,22}C) is reported for the first time in this thesis using the proton radii determined in this work and measured matter radii available

from the literature. ΔR_{np} of 1.23 (20) fm is determined for the two-neutron halo, ^{22}C affirming the presence of a halo. The halo radius of 6.6 $\pm$ 1.1 fm in ^{22}C is found to be as large as ^{11}Li. The proton radii are compared to the predictions reported for these neutron-rich carbon isotopes. The experimental proton radii have challenged these predictions.

October 20, 2022.

Acknowledgements

I would like to thank my esteemed supervisor Prof. Rituparna Kanungo for this invaluable supervision, support, patience, ideas, and tutelage during the course of my P.hD. degree. Her immense knowledge and profound understanding of nuclear physics has encouraged me all the time in my academic research and daily life. I am also grateful to her for providing me with the opportunity to work under her supervision. It was a great learning experience.

I would also like to express my sincere gratitude to my committee members Prof. Luigi Gallo, and Prof. Greg Christian for their advice and support during my research.

I would also like to thank the collaborators from the RIBF facility, Japan, and GSI, Germany. I owe my special thanks to Prof. Soumya Bagchi and Dr. Yoshiki Tanaka for their valuable insights and patience during the research group meetings. Thanks for the valuable physics discussion and help during my data analysis.

Thanks to everybody at Saint Mary's University. To Mukhwinder, for all the lively discussions we had whether it was physics, programming, writing and sharing the load.

Finally, a big thank you to my family. Thank you, Mom and Dad, for all of the unconditional love, and constant support, and for encouraging me to pursue new things outside academia. A special thanks to Kewtoo for all of the moral support, love, and care. It would have been a lot harder without you guys to go through Ph.D.

There were so many great people I encountered throughout this journey. It would

have been difficult to come this far without them. I want to thank those people too who helped me in different ways along this journey.

Chapter 1

Introduction

The discovery of the atomic nucleus in 1911 by Rutherford through the alpha scattering experiment from a gold foil opened up an interesting subject, the nuclear force. It has allured both theoretical and experimental physicists. Over the past century, scientists have probed deeper into the structure of the nucleus, to understand the behavior of the nuclear force, and how the nuclei have come into existence. The study of these physical phenomena has led to the development of exotic radioactive beams and the construction of state-of-the-art experimental facilities.

Since Rutherford's scattering experiment, numerous experiments have been carried out to probe the structure of the nuclei and these developments have led to the emergence of different theoretical models needed to describe the structure of a nucleus. These advancements have helped the scientific community substantially by enhancing knowledge about the physical processes occurring in nature and also lead to the development of other fields such as medical physics using radiation for the treatment and diagnostics of diseases, nuclear power plants, materials science and archaeology.

A fundamental question was: how are nucleons held together inside a heavy nucleus despite the Coulomb repulsion of the protons? The nuclear force defined as a

force between nucleons inside a nucleus is a residual effect of the strong force. This strong force is an attractive force that binds the protons and neutrons. Yukawa made the first attempt to provide a microscopic description of the nuclear force as an exchange force originating from the exchange of particles. He hypothesized that the exchange particle for the nuclear force between two nucleons should be a massive charged particle, now known as π meson. According to the uncertainty principle, the massive exchange particle between the nucleons is restricted to a short finite distance $\sim$1 fm. Therefore, the nuclear force acts as a short range force as this range is even smaller than the size of the nucleus. Measured nuclear binding energies evidently proved that the nuclear force saturates, resulting in an approximately constant nucleon density. The liquid drop model [1] investigates different properties appearing in a number of studies such as the binding energy, size and shape of the nucleus. It provides an excellent agreement with the first order measured nuclear binding energies but could not explain the high stability of nuclei with certain proton or neutron numbers which illustrates further the existence of closed shells at these numbers. The number of nucleons required to form a closed shell are referred to as the "magic numbers" i.e. 2, 8, 20, 28, 50, 82 and 126. The Shell model of nucleus explains these magic numbers which considers each nucleon to move independent of others in a symmetric potential produced by all nucleons and classifies the energy levels in terms of quantum numbers analogous to the wavefunctions of individual electrons in atomic physics. The nuclear potential also known as Woods-Saxon potential has the following form for a spherical nucleus [2]:

$$V_{ws}(r) = \frac{-V_0}{1 + e^{(\frac{r-R}{a})}} \tag{1.1}$$

with the potential well depth $V_0 \sim 50$ MeV and the radius parameter $R \sim 1.21\, A^{\frac{1}{3}}$ (fm), where A is the mass number and a is the diffuseness parameter ~ 0.53 fm. Mayer [3] added a spin-orbit interaction term independent of Haxel, Jensen and Suess [4], arising from the interaction between the orbital motion of nucleon and its intrinsic spin. The

Woods-Saxon potential for a spherical nucleus is given by:

$$V_{ws}(r) = \frac{-V_0}{1 + e^{(\frac{r-R}{a})}} + W(r)\vec{L}.\vec{S} \tag{1.2}$$

where $\vec{L}$ and $\vec{S}$ are the orbital and intrinsic spin angular momentum operators, respectively. The spin orbit potential in Equation 1.2 is given by $W(r) = \frac{1}{r}\frac{dV_{ws}(r)}{dr}$. Using Equation 1.2, the energy levels can be found with the splitting due to the spin-orbit coupling as shown in Figure 1.1.

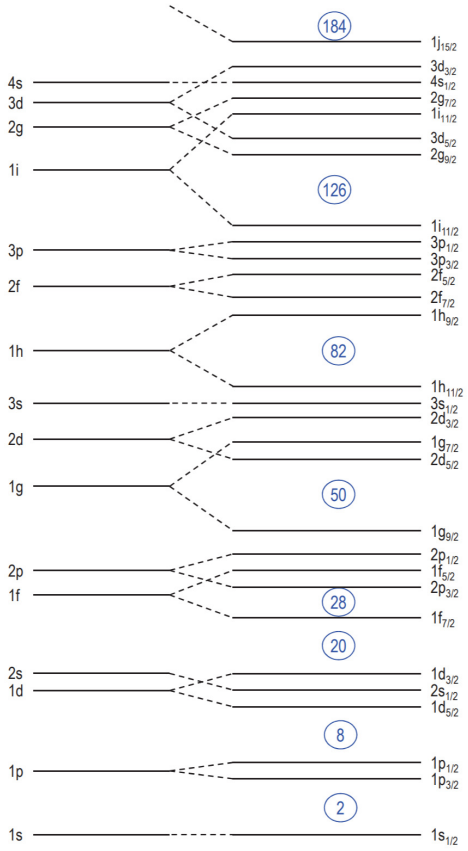

Figure 1.1: The energy levels of a nucleon predicted by nuclear shell model using nuclear potential of a single particle (left) and the splitting due to spin-orbit coupling (right) [5].

The shell model was a huge success because of its excellent reproduction of measured excitation energies, spin/parities for the ground state and low-energy excited states; and for the first time an explanation for particular stability at so called “magic

numbers" were found. The stability of the nucleus at the so-called "magic number" was explained by the shell model but it suffered from many shortcomings. The magnetic dipole moments, disappearance of magic numbers at the drip-line and the emergence of new magic numbers could not be explained by the conventional shell model. The shell model does not account for the collective motion of nucleons as it could not explain the rotational and vibrational levels in deformed nuclei. There is no single theoretical model that can describe the structure of all the nuclei. The nuclear shell model gives a complete description of many medium mass nuclei, mean field approaches describe the heavier nuclei and the few-body cluster models define the lighter nuclei. These nuclear models are not able to explain many important features of nuclei mentioned above, as they were formulated based on data of around 300 stable nuclei.

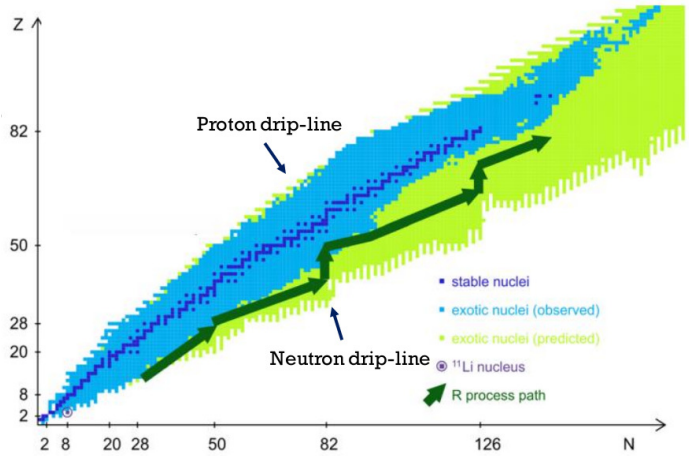

Figure 1.2: The limits of nuclear landscape depicting the experimentally known isotopes, both stable (dark blue squares) and radioactive (light-blue squares). The light-green squares denote those predicted by a theoretical model [6]. The r-process path is indicated by the dark-green arrows [7].

The technological evolution of nuclear physics facilities enabled scientists to produce over 3000 unstable nuclei far from the beta-stability line which is beyond the conventional knowledge of stable nuclei. The evolution of the nuclide chart is shown in Figure 1.2 where the black squares represent the nuclei at the stability line. At the extremities, where the binding energy is not enough to prevent the last nucleon from

"dripping" off the nucleus, the neutron and proton drip-lines form the boundaries of nuclear existence.

This advancement resulted in the discovery of some exotic features of nuclear structure by investigating the nuclei towards the neutron-rich region resulting from the large neutron/proton (N/Z) asymmetry. These nuclei exhibit exotic phenomena like the existence of a neutron halo or skin. A significant contribution was made by Tanihata $et\ al.$ [8], by determining the extraordinary large enhancements of interaction radii R_{int} from the interaction cross-section σ_{int} measurements of the neutron-rich ^{11}Li and ^{14}Be nuclei as shown in Figure 1.3.

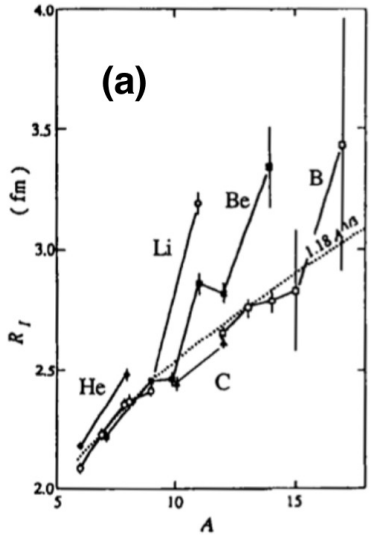

Figure 1.3: Interaction radii (R_{int}) of He, Li, Be and B isotopes [9].

This discovery pointed to the existence of a neutron halo structure in these neutron-rich nuclei. The halo occurrence in light neutron-rich nucleus ^{11}Li ushered a new era in nuclear science and is one of the most intriguing phenomena observed far from the stability that breaks many long-established rules of nuclear structure. The term "halo" refers to one or two weakly bound nucleons (neutrons) forming a low density cloud around the core with normal density distributions of protons and neutrons which is well associated with the contribution of the continuum above the threshold of particle

emission as shown in Figure 1.4.

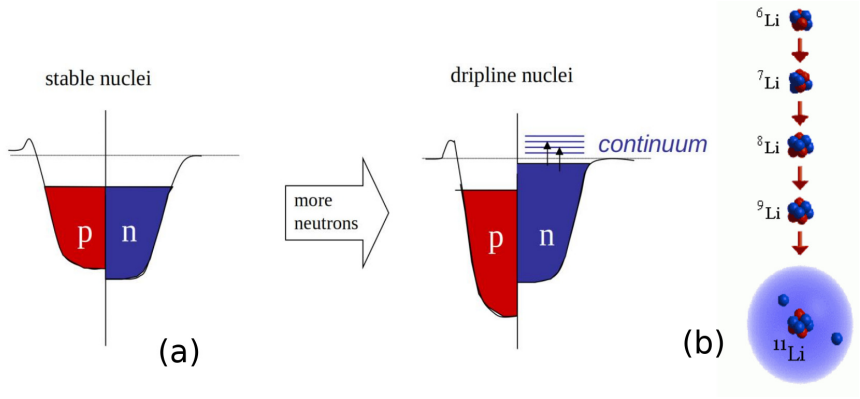

Figure 1.4: (a) A schematic illustration of the contribution of the continuum (b) lithium's isotopic chain [10].

A low angular momentum motion for the valence particle is necessary for the decoupling of the core nucleus and the halo neutrons. The lower the orbital angular momentum, the longer the extended tail in the distribution. Halos are therefore identified by an abruptly large increase in the matter radius compared to the neighboring isotope as shown in Figure 1.3.

The observed characteristic features of a nucleus can be understood by studying the shell structure of a nucleus. Another new phenomenon has emerged in the neutron-rich Na and Mg isotopes, the classic magic number $N = 20$ was found to be non-magic [11–13]. For nuclei in the neutron-rich region, this reveals a considerable modification of the nuclear shell structure. The nucleon radii of light exotic nuclei might exhibit unique shell closure behavior at $N = 16$ which is different from nuclei lying near the stability line [14, 15]. Neutron number (N) dependence of experimentally observed neutron separation energies (S_n) showed an anomaly in $p - sd$ and sd shell nuclei as shown in Figure 1.5. The separation energies of the same isospin ($T_z = N - Z/2$) are connected by the lines, where the kinks represent the magic numbers. Kinks appear clearly for magic numbers $N = 8, 20$ for small T_z nuclei and disappears for large T_z nuclei. The disappearance of nucleon shell closure at $N = 8$ (kink) shows the change

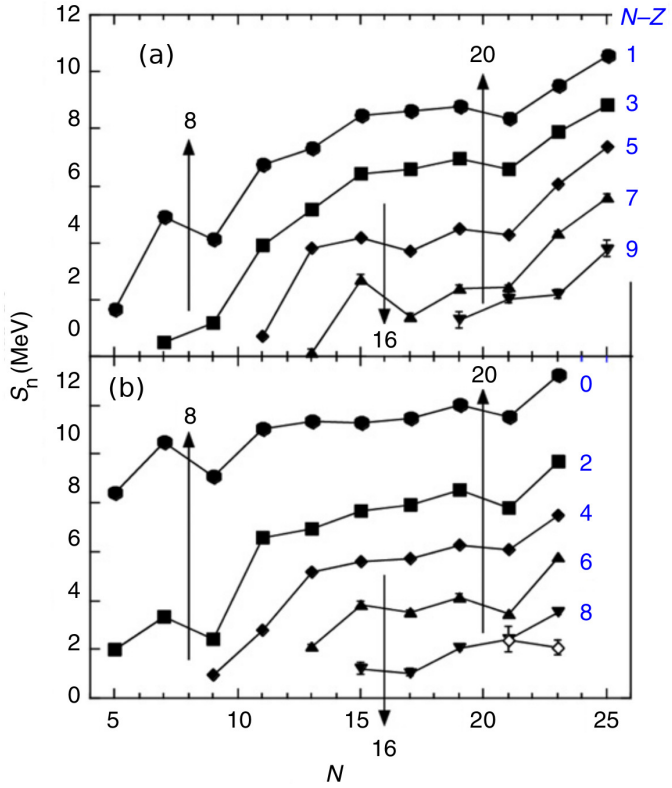

Figure 1.5: Dependence of neutron number with the experimentally observed neutron separation energies (S_n) for nuclei with (a) odd N and even Z (b) even N and odd Z. Numbers next to the line indicate $2T_z$ [14].

of shells for $p - sd$ shell nuclei. A new magic number at $N = 16$ is indicated due to the appearance of a kink for large isospin $(T_z \geq 5/2)$.

Nuclear shapes can vary rather widely across the nuclear landscape. The doubly magic nuclei, with magic numbers for both protons and neutrons prefer spherical symmetry [16]. Recent evidence of momentum distribution from one-neutron removal reaction of ^{24}O revealed the first footprint required to establish ^{24}O as a doubly-closed magic-number nucleus [17]. Momentum distribution is highly sensitive to the single particle(s) orbitals occupied by the valence neutrons. The results show a large neutron spectroscopic factor of 1.74 (19) reflecting the occupation number of the last two neutrons in $2s_{1/2}$ orbital which proves ^{24}O has a spherical shell closure. The spherical nature of this shell closure was affirmed by the small quadrapole deformation parameter β_2 = 0.15 $\pm$ 0.04 of the first excited state of ^{24}O measured using proton inelastic

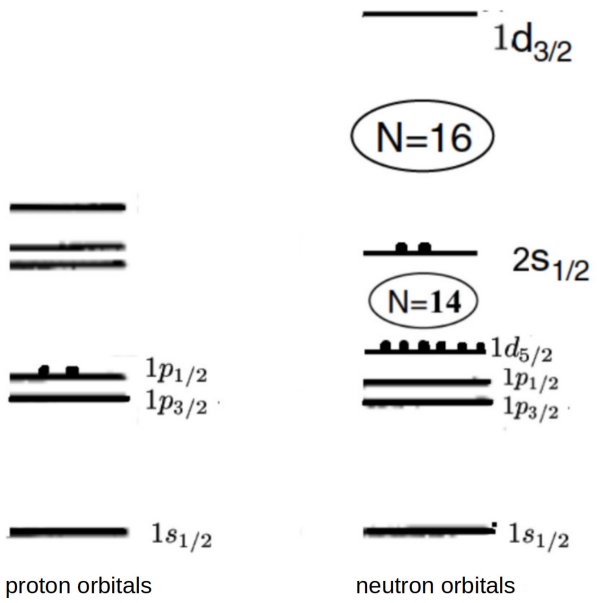

Figure 1.6: Schematic illustration of nuclear orbitals in ^{24}O. The circled number denote the new shell closures in neutron-rich regions.

scattering [18]. The shell closure at N = 16 indicates an increased shell gap between the $2s_{1/2}$ and $1d_{3/2}$ neutron orbits of ^{24}O as shown in Figure 1.6. The large shell gap at N = 16 ($\sim$ 4.8 MeV) between the $2s_{1/2}$ and $1d_{3/2}$ was obtained through the neutron removal reactions from ^{26}F to ^{24}O [19] which asserts the occupation of neutrons in the $2s_{1/2}$ orbit.

The structures of the most neutron-rich carbon isotopes ^{19,20,22}C were studied using single- and two-neutron removal reactions on a carbon target. The narrow momentum distribution of ^{20}C following the two-neutron removal from ^{22}C provided strong evidence for the weakly bound $\nu s^2_{1/2}$ character for the ^{22}C ground state as shown in Figure 1.7 [20]. The contributions from the knockout via the $1/2^+_1$ and $5/2^+_1$ unbound ^{22}C intermediate states are shown by the dashed and dotted-dashed curves, respectively. The individual components from the final states are well in agreement with the data, asserting the dominant configuration of $\nu s^2_{1/2}$ in ^{22}C. The two-neutron removal reaction from the ^{20}C shows a much broader momentum distribution. The agreement of the data with the inclusive cross-section and momentum distribution of

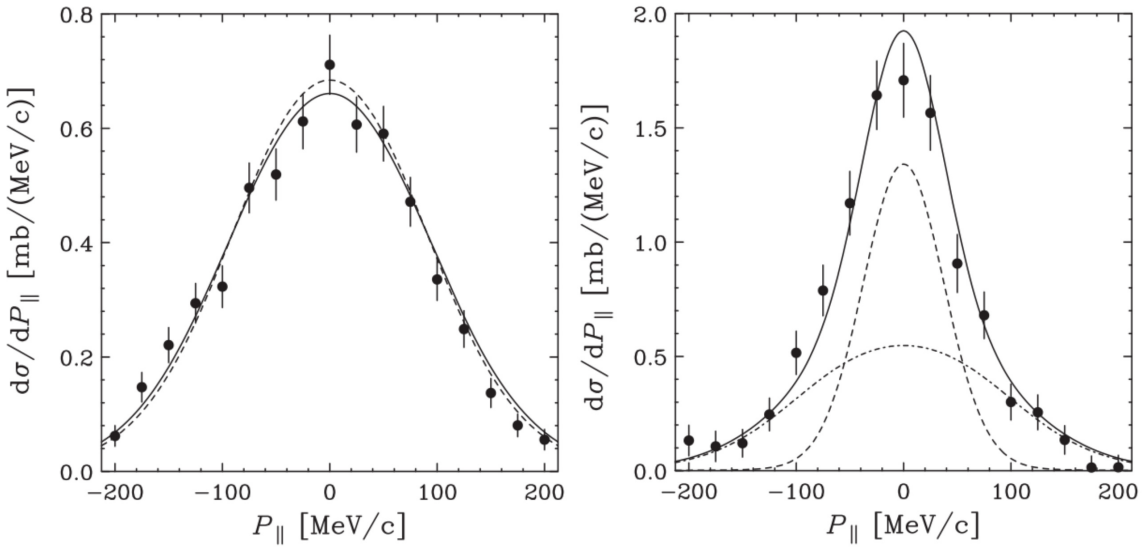

Figure 1.7: (a) The measured inclusive parallel momentum distribution of ^{18}C following the two-neutron removal from the ^{20}C shows a broad momentum distribution. The momentum distribution is compared to the theoretical calculations which are weighted sum of the exclusive calculations of the unbound ^{19}C states. The calculations are predicted for $5/2^+_1$ knockout with a character $l = 2$. (b) The measured inclusive parallel momentum distribution of ^{20}C following the two-neutron removal from the ^{22}C shows a narrow momentum distribution. The momentum distribution is compared to the weighted sum of the exclusive calculations of the unbound ^{21}C states shown by the solid curve. The contributions from the knockout of the $1/2^+$ and $5/2^+$ unbound ^{21}C intermediate states are shown by the dashed and dotted-dashed lines, respectively. The calculations are predicted for $1/2^+_1$ knockout with a character $l = 0$ [20].

^{20}C is good, providing support for the $5/2^+_1$ to be likely unbound.

The formation of neutron halos is closely connected with the evolution of shell structure and changes in nuclear magicities around drip-lines [7]. The integral component for the neutron halo formation is the $2s_{1/2}$ single-particle orbital. Most of the presently known neutron halos from Li-F are related to the $2s_{1/2}$ wave. The relation of interaction cross-sections with the isotopes of Li-F is shown in Figure 1.8. The background color represents the position of each spherical shell orbital. The most striking aspect is the contribution of the s-wave to all the elements near the drip-line and not only in the expected neutron numbers [21]. The s-wave has the lowest orbital angular momentum which in turn reduces the centrifugal barrier of the specific orbital. Therefore, the neutron halos are primarily formed in the s-wave. The halo in ^{22}C is believed to be caused by the valence neutrons in the s-wave [22–26], but the probability am-

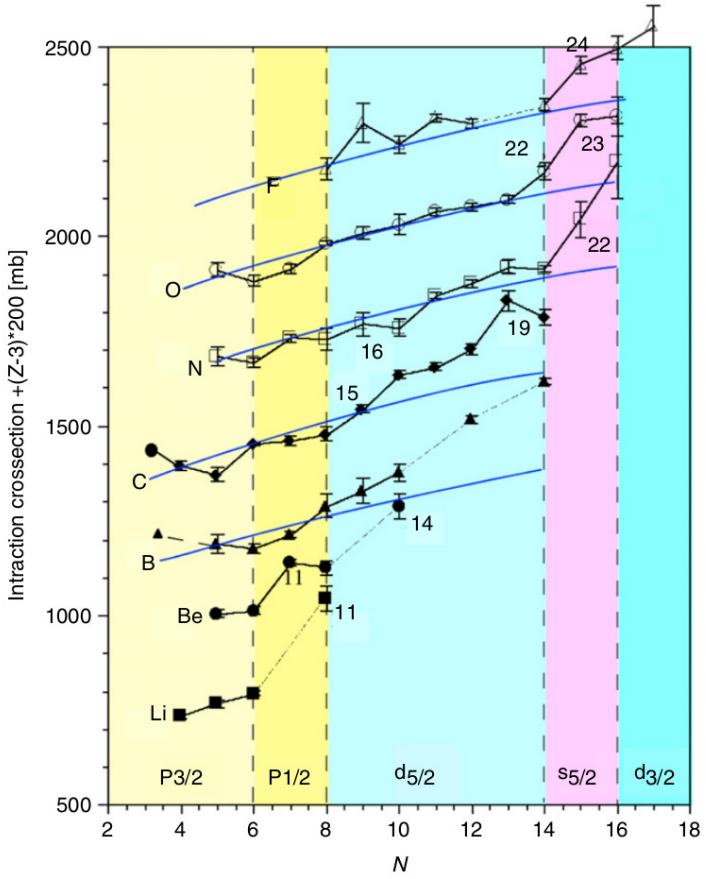

Figure 1.8: Interaction cross-section of light isotopes [27].

plitude of the s-wave is still not well determined. The subshell closure of $N = 14$ and $N = 16$ has been a hot topic in the study of neutron-rich nuclei [23]. This value is closely related to the shell evolution characterized by the inversion of ($\nu s_{1/2}$, $\nu d_{5/2}$) neutron orbits. This inversion has been predicted in $A/Z \sim 3$ nuclei [14]. This competition between the neutron orbits plays a pivotal role in determining the structure of carbon isotopes with $N \geq 9$.

The proton distribution radius is an important parameter for understanding the halo formation in a nucleus and constraining newly developed theoretical structure models and the nuclear interaction. The evolution of proton radii along an isotopic chain for the drip-line isotopes with the knowledge of matter radii which is the radii of distribution of nucleons in nuclei, can show the shell evolution. High precision

measurements of neutron-rich light nuclides have clearly revealed that the presence of halo neutrons enhances the proton distribution radii of the core nuclei as compared to the corresponding nuclei without the halo neutrons as shown for ^{11}Li in Figure 1.9.

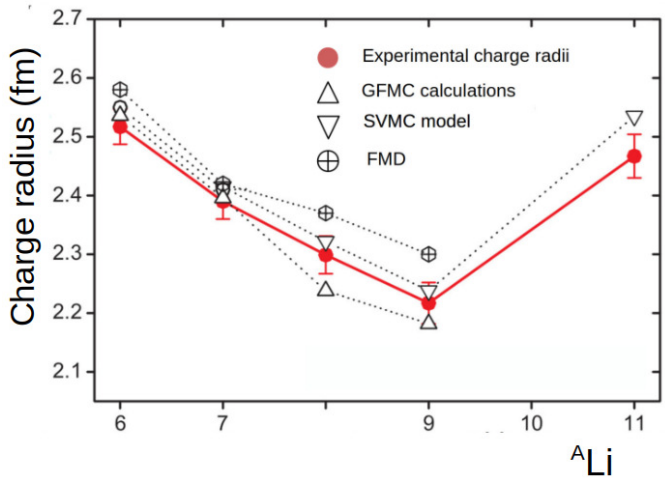

Figure 1.9: Charge radii of Li isotopes [28].

The neutron-rich carbon isotopes ^{20}C and ^{22}C are particularly of interest, with a two neutron halo identified in ^{22}C at the drip-line with a ^{20}C core owing to the large matter radius deduced from interaction cross-section and a small two-neutron separation energy compared to the other carbon isotopes [25,26]. The predictions for the root mean square (rms) radius of protons is almost flat for neutron-rich carbon isotopes as shown in fig 1.10. The closed filled circles represent the root-mean square radii predicted from the relativistic mean-field calculations and the open filled circles represent the dynamical model with core+n model used for the odd isotopes ^{13,15,17,19}C, where the cores are ^{12,14,16,18}C, respectively [31], and a core+2n model is assumed for ^{16,22}C. The nuclear magicities and the collapse of the traditional magicities in certain regions of the nuclear landscape, is largely being investigated. The neutron-rich carbon isotope, ^{20}C was studied using the in-flight double step fragmentation reaction [32]. The evolution of the 2^+ energies upto $N = 14$ for the carbon isotopic chain is shown in Figure 1.11. The similarity between the oxygen and carbon isotopes trend for 2^+ ener-

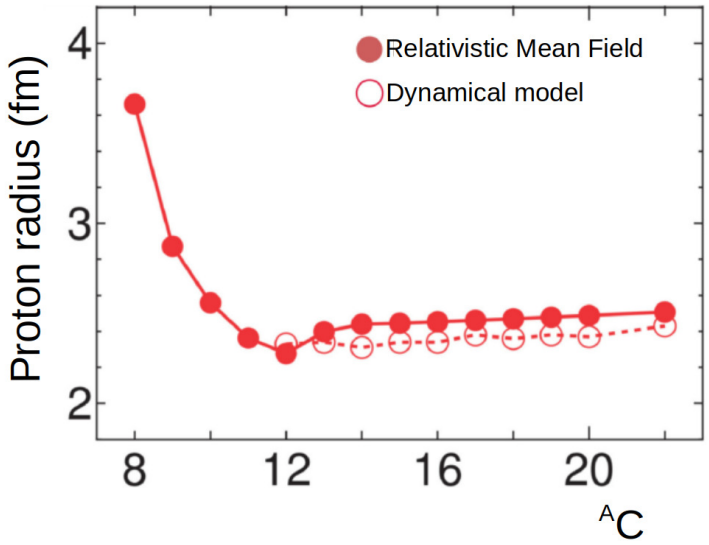

Figure 1.10: Root-mean-square point-proton radii with respect to the mass number of carbon isotopes [29, 30].

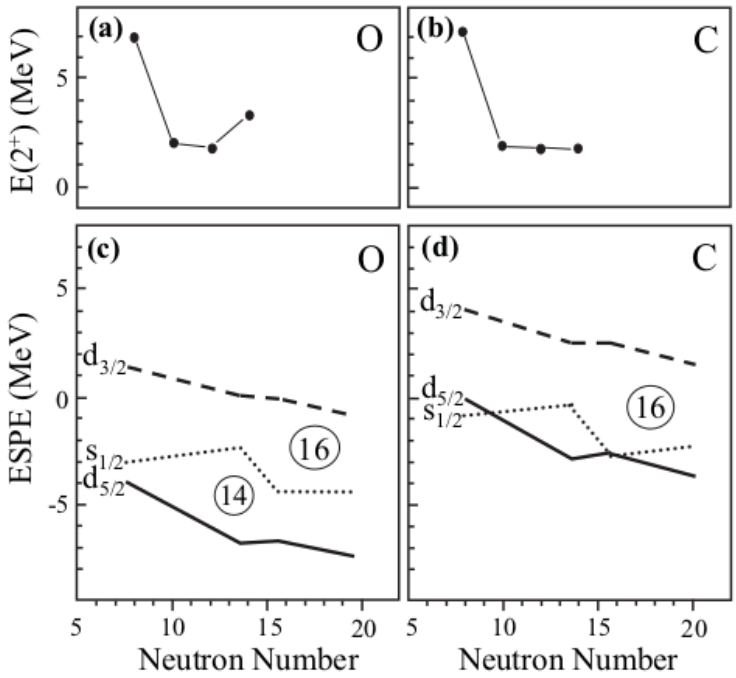

Figure 1.11: The systematics of the 2^+ energies as a function of the neutron number in (a) oxygen and (b) carbon nuclei The effective single-particle energies (ESPE) as a function of the neturon number is shown for (c) oxygen and (d) carbon isotopes [32].

gies is striking. But, the 2^+ energy of ^{20}C is significantly smaller than ^{22}O. This might indicate the absence of subshell closure at $N = 14$ in the C isotopic chain.

The halo nucleus, ^{22}C is closely associated with the inversion of two neutron orbitals $\nu 2s_{1/2}$, $\nu 1d_{5/2}$, deformation and the shell evolution [7]. The inversion of $\nu 2s_{1/2}$, $\nu 1d_{5/2}$ in ^{22}C is also found in deformed relativistic Hartree-Bogoliubov theory in continuum (DRHBc) which predicts a shell closure at $N = 16$ in the spherical limit [33]. In the spherical limits $2s_{1/2}$ state is lower than $\nu 1d_{5/2}$ as shown in Figure 1.12 (a) and (b). The inversion of $2s_{1/2}, 1d_{5/2}$ was predicted for $A/Z \sim 3$ nuclei [14], which is

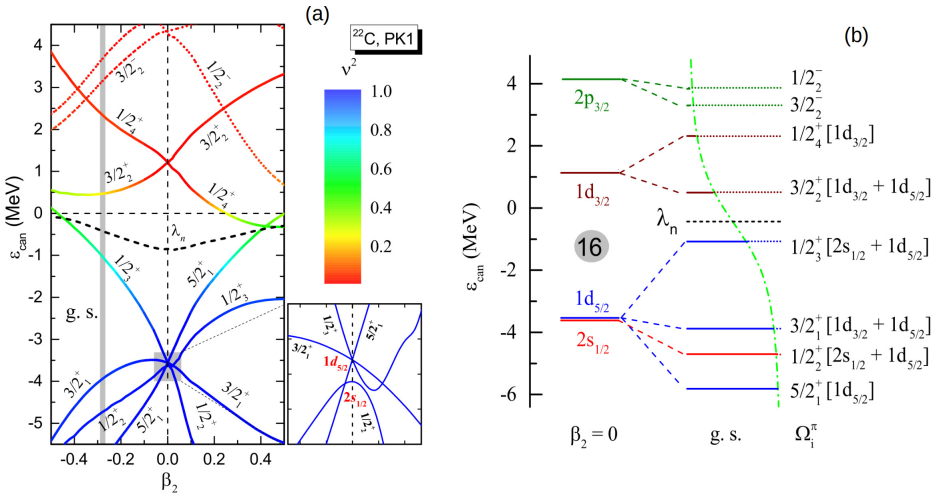

Figure 1.12: Single neutron orbits of ^{22}C around the Fermi-level in the canonical basis obtained from constraint calculations are shown in (a) The Fermi-level (λ_n) is displayed by the black dashed lines and the ground state of ^{22}C is shown by grey vertical line. and (b) The occupation probability (ν^2) is given by the length of the solid line caluclated from the DRHBc model fro the ground state. The dash dotted-line represents the ν^2 for the average pairing gap calculated from the BCS model [33].

closely associated to the competition of $2s_{1/2}, 1d_{5/2}$ orbitals [7, 17, 23]. The valence neutrons occupy a d-wave orbital if the spherical limit is considered for ^{22}C. However, predicted quadrapole deformation parameter $\beta_2 = -0.27$ of the ground state drives ^{22}C to be well deformed shown by the grey vertical line in Figure 1.12 (a). The probability of occupying an orbital ν^2 is represented with different colors. The strong quadrapole correlations in this nuclei mix the sd orbitals as shown in Figure 1.12 and destroys the $N = 16$ closure. The total amplitude of $2s_{1/2}$ component is ~ 0.25 in the two $1/2^+$ orbitals because of the mixture of sd orbitals as shown in Figure 1.12 (b). The half of the valence neutrons in ^{22}C are of the $2s_{1/2}$ nature because of degeneracy

of two. The halo in ^{22}C is predicted to be shrunk compared to with what it would be if the $(2s_{1/2})^2$ was the dominant configuration.

The scientific progress in understanding the nuclear structure is facilitated by collecting more experimental data and comparing them to the results derived from different theoretical models. The scientific motivation of this dissertation is to measure the charge-changing cross-section (σ_{cc}) of ^{20}C and ^{22}C, to determine their proton (distribution) radii. Systematic study of the measured proton radii with the matter radii will allow characterizing the geometric correlation in 2n-halos and also provide information on neutron skin thickness. The root mean square (rms) point proton radii R_p is the radius of proton distribution of a nucleus with protons as point particles inside the nucleus. The point proton radii of neutron-rich carbon isotopes ^{20,22}C will be extracted for the first time from the measured σ_{cc} using the RIBF accelerator complex located at RIKEN, Japan.

The upcoming chapters of this thesis are classified in the following manner:

- Chapter 2 presents a brief description of halo formation and the scientific motivation of this work. An overview of theoretical models which lead to the advancement of the $ab\ initio$ theory of nuclear forces. The second section discusses the traditional methods used to measure the point proton radius of a nucleus. The end section of this chapter focuses on the Glauber model framework, which is used to compute the proton radius from the measured σ_{cc}.

- Chapter 3 gives the description of BIGRIPS separator and Zero Degree spectrometer (ZDS) at the RIBF accelerator complex used to measure the σ_{cc}. The electronics and data acquisition system are explained in the second part of this chapter.

- Chapter 4 illustrates the techniques used to analyze the data obtained from different sets of detectors.

- Chapter 5 discusses the results obtained from the experiment and their compar-

ison with the predictions of theoretical models.

Chapter 2

Halo nuclei and the point proton distribution

Strong interaction (nuclear force) cannot bind two neutrons together or one neutron to a neutron-rich nucleus such as ^{9}Li. Yet, adding two neutrons to the stable ^{9}Li forms a three-body bound system, also known as a Borromean nucleus which has a remarkable property that none of its two-body subsystems are bound. The halo occurrence in light neutron-rich nuclei such as ^{11}Li has ushered a new era in nuclear science and is one of the most intriguing phenomena observed far from the stability that break many long-established rules of nuclear structure. Before taking a closer look at special cases of nuclear halos, it is necessary to point out what actually is a halo state and under what conditions will it be manifested.

2.1 Exotic phenomena of Halo formation

The nucleons of a nucleus are bound together by the strong interaction force (nuclear force), which is a short-range force. Therefore, all the nucleons should be confined in a compact space or be unbound like ^{10}Li. Equation 1.2 shows a well-known relation for the nucleon distribution $R = r_0 A^{\frac{1}{3}}$, which gives a good approximation of the matter

radius of a nucleus, since the nucleons are distributed equally inside the nuclear core. However, all the nuclei do not abide by the same approximation. Threshold effects can occur for the nuclei close to the drip-lines, if the nucleons fill the nuclear potential well up to the limit. For instance, in a finite 1-D square well potential, the deeply-bound states are mostly confined within the potential. But bound states with eigen-energies just below the surface of the potential well have long tails which allow the nucleon to tunnel beyond the range of the potential. Quantum mechanically, there is a significant probability of finding a nucleon outside the nuclear core. The term "halo" refers to one or two weakly bound nucleons (neutrons) forming a low density cloud around the core with normal density distributions of protons and neutrons. This term was first coined by P. G. Hansen and B. Jonson in 1987 [34], which became a label for the weakly bound nucleons having a long tail in the density distribution of a nucleus. A spherical or a stable nucleus has similar density distribution of protons and neutrons with the same *R* and *a*, given by Woods-Saxon distribution analogous to Equation 1.2:

$$\rho_{ws}(r) = \frac{\rho_0}{1 + exp\left(\frac{r-R}{a}\right)} \tag{2.1}$$

The density distribution $\rho_{ws}(r)$ has an exponential tail for large r but the slope factor *a* is independent of the mass number of the stable nuclei, which is associated with the outermost neutron(s) wavefunction. The density at the center is represented by $\rho_0 \sim 0.17$ fm^{-1} and the radius parameter R is parameterized by mass number A, $R \sim 1.10A^{1/3}$ (fm). The wave function of the neutron outside the potential is written as:

$$\psi(r) = \left(\frac{2\pi}{k}\right)\left(\frac{e^{-kr}}{r}\right)\left[\frac{e^{kR}}{(1+kR)^{\frac{1}{2}}}\right] \tag{2.2}$$

where R is the width of the potential and the parameter k represents the density tail [2]. The neutron density distribution can be determined using the wave function

described in 2.2:

$$\rho(r) = |\psi(r)|^2 \propto \left[\frac{e^{-2kr}}{r^2}\right] \tag{2.3}$$

where k is associated to the separation energy of the neutron (E_s) given by:

$$(\hbar k)^2 = 2\mu E_s \tag{2.4}$$

where μ is the reduced mass of the system consisting of the core nucleus and the outermost neutron(s). The slope factor is consistent as the $E_s \sim 6 - 8$ MeV for most of the stable nuclei. Since the density tail (k) is proportional to the separation energy, k

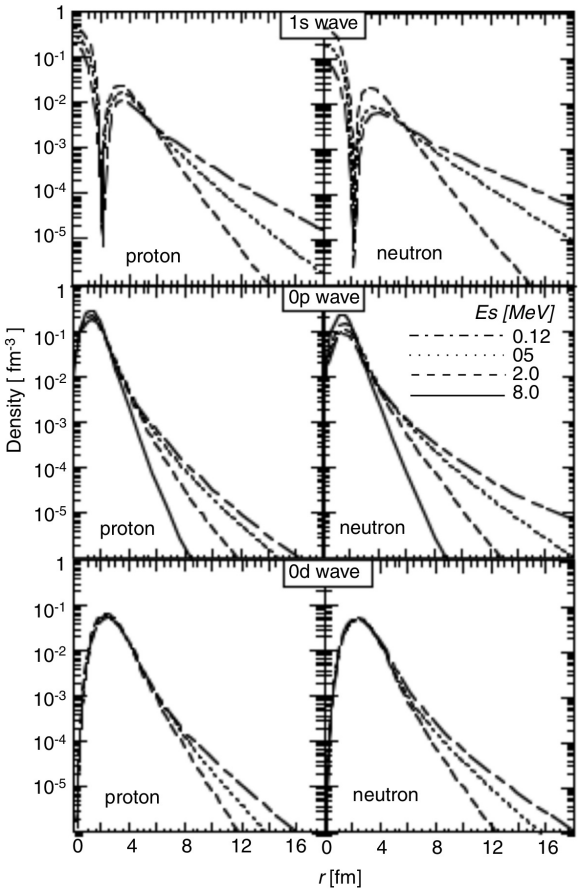

Figure 2.1: Density distribution of a nucleon in single-particle orbitals [2].

decreases as E_s decreases for the nuclei out of the stability line which in turn changes the diffuseness parameter in an unstable nucleus.

Smaller separation energies have longer tail distributions as shown in Figure 2.1 for different single-particle orbitals in Woods-Saxon potential given in Equation 1.2. Therefore, a small nuclear binding energy is one of the preconditions for the formation of a halo nucleus but not the only one. In addition to the decoupling of the core nucleus and halo neutrons, a low angular momentum orbital for the valence particle is also necessary. An additional centrifugal barrier is introduced because of higher l-values which lowers the probability of valence nucelon(s) tunneling to a larger radius. Therefore, the halo phenomenon is associated with $s-$ and $p-$ states. The confining Coulomb barrier in the proton-rich nuclei hinders the formation of a proton halo state making them less articulate than neutron halos.

2.2 Scientific Motivation to study the proton radii of ^{20,22}C

One of the main topics in modern nuclear physics is the study of exotic nuclear structures. With the advancement of heavy-ion accelerators and radioactive ion beam facilities, one of the goals is to understand the most striking exotic nuclear phenomenon "nuclear halo" which was first observed by I. Tanihata *et al.* [8] in ^{11}Li. Recently, the most neutron-rich carbon isotope ^{22}C is of particular interest owing to the large matter radius deduced from interaction cross-sections measured in two different experiments, $R_M = 5.4\pm$ 0.9 fm in 2010 [35] and $R_M = 3.44\pm$ 0.08 fm in 2016 [26] and a small two-neutron separation energy $S_{2n} = -0.14\pm$ 0.46 MeV [36]. ^{22}C is the most neutron-rich bound nucleus among C isotopes having a Borromean three-body system consisting of ^{20}C (core) + n + n in the $p-sd$ shell. With evidence of magic number $Z = 6$ in the neutron-rich carbon isotopes [37] and a new shell closure observed at $N = 16$, established for ^{24}O [14, 38–40], ^{22}C is also significant to provide some clues about the evolution of shell structure which results in (dis)appearance of magic numbers.

The deformed shapes of the core and the halo of ^{22}C were predicted using a de-

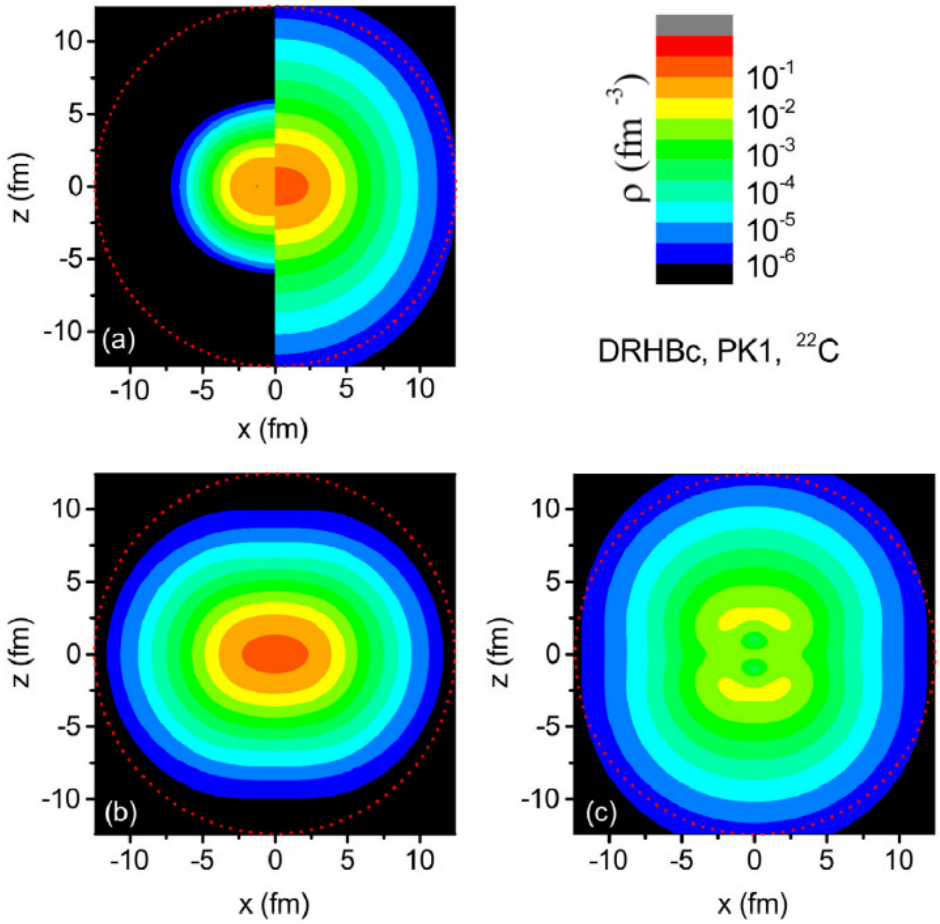

Figure 2.2: The density distribution of the neutrons and protons are shown in the left and right parts, respectively. z-axis as the symmetry axis. (a) Proton ($x < 0$) and neutron ($x > 0$) density profiles (b) Density profile of neutron core (oblate) (c) Density profile of 2 neutron halo (prolate) of ^{22}C [33].

formed relativistic Hartree-Bogoliubov model in continuum (DRHBc model) to be prolate and oblate respectively as shown in Figure 2.2 [33]. The results from this theoretical model also predicts a shrunk halo and a quenched shell gap at $N = 16$. The matter radius predicted from this method, R_m = 3.25 fm is close to the value 3.44 $\pm$ 0.08 fm obtained in 2016 [26] and 3.38 $\pm$ 0.10 extracted recently [22]. The difference between a deformation and a halo state can be resolved using the charge-changing and neutron removal cross-sections [41]. The observed Borromean nuclei ^{6}He [42], ^{11}Li [28] and ^{17}B [43] as well as one-neutron halo ^{11}Be [44] show an increase in the proton radius along an isotopic chain due to the halo effect. The increase in proton

radius for the Borromean nucleus ^{14}Be is relatively smaller [45], which raises further questions about the evolution of proton radii when we approach the drip-line at ^{22}C. A systematic study of proton radius in conjunction with the matter radius will allow us to characterize the halo configuration and the shell evolution in these drip-line carbon isotopes.

2.3 Proton and matter radii in halo nuclei

The proton radius is an important property to understand the influence of significantly large spatial extension of the neutron wavefunction on the protons of the core nucleus of these exotic nuclear structures. The geometric correlation in two-neutron halos can be studied using the matter and proton radii of a halo nucleus.

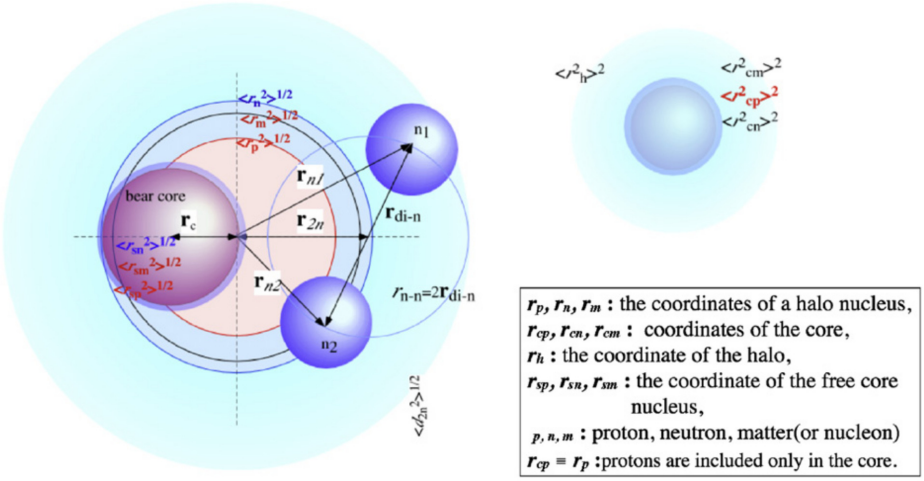

Figure 2.3: The left figure shows the geometry of a Borromean nucleus with the core nucleus and halo neutrons. The figure at the top right shows the density distribution of the halo nucleus just separated to the core and neutron halo densities [2].

A Borromean nucleus consists of a three-body system, as an example, the proton and neutron distribution of the ^{20}C core in the ^{22}C halo nucleus is exactly the same as the free ^{20}C nucleus. The proton and neutron distributions in the most neutron-rich C isotope are defined by the two outermost (halo) neutrons and the moving ^{20}C core. The geometry of a Borromean nucleus is shown in Figure 2.3. In the core plus neutron

model following [2], the relation between mean-square radii of nucleon, proton and neutron $\langle r_{im}^2 \rangle$, $\langle r_{ip}^2 \rangle$, $\langle r_{in}^2 \rangle$ for a nucleus i is,

$$A_i \langle r_{im}^2 \rangle = Z_i \langle r_{ip}^2 \rangle + N_i \langle r_{in}^2 \rangle \tag{2.5}$$

where A_i, Z_i, N_i are the number of nucleons, proton and neutrons in the nucleus i, respectively.

The matter radius for ^{22}C is known from refs. [25, 26] and the proton radius is determined from charge-changing cross-section measurements which would enable us to determine the corresponding neutron radius using Equation 2.5. All the radii of halo nucleus $\langle r_m^2 \rangle$, $\langle r_p^2 \rangle$, $\langle r_n^2 \rangle$ and the core $\langle r_{sm}^2 \rangle$, $\langle r_{sp}^2 \rangle$, $\langle r_{sn}^2 \rangle$ can be determined from its matter and proton radii using the core plus neutron model. The matter radii of a halo nucleus in relation to the core nuclei $\langle r_{cm}^2 \rangle$ and the halo neutrons $\langle r_h^2 \rangle$ are given as:

$$A \langle r_m^2 \rangle = A_c \langle r_{cm}^2 \rangle + A_h \langle r_h^2 \rangle \tag{2.6}$$

where A, A_c and A_h are the mass numbers of the halo nucleus, core nucleus and the number of outermost neutrons, respectively. The motion of the central core of the halo nucleus is defined as the mean square (ms) radius $\langle r_c^2 \rangle$. The relation between the nucleon, proton, and neutron radii of a halo nucleus to that of the core and the halo nucleus is given by:

$$\begin{aligned} \langle r_p^2 \rangle &= \langle r_{sp}^2 \rangle + \langle r_c^2 \rangle \\ \langle r_{cm}^2 \rangle &= \langle r_{sm}^2 \rangle + \langle r_c^2 \rangle \\ \langle r_{cn}^2 \rangle &= \langle r_{sn}^2 \rangle + \langle r_c^2 \rangle \end{aligned} \tag{2.7}$$

The movement of the core $\langle r_c^2 \rangle$ and the radii of the core in the halo nuclei $\langle r_{cm}^2 \rangle$, $\langle r_{cn}^2 \rangle$, can be determined using the aforementioned equations. The ms radius of the halo distribution can be determined using Equation 2.6. The distance of the center of mass

of two halo neutrons from the core is represented by the correlation:

$$A_c r_c = -A_h r_{2n} = -A_h \frac{(r_{n1} + r_{n2})}{2} \quad \text{then} \quad A_c^2 \langle r_c^2 \rangle = A_h^2 \langle r_{2n}^2 \rangle \tag{2.8}$$

where r_{n1} and r_{n2} represent the radius of the halo neutrons as shown in Figure 2.3. The average geometric correlation in two-neutron halos can be understood around the center of mass of two halo neutrons as:

$$r_{n-n} = r_{n1} - r_{n2} = 2r_{di-n} \quad \text{then} \quad \langle r_{n-n}^2 \rangle = 4 \langle r_{di-n}^2 \rangle \tag{2.9}$$

The relation between the halo distribution and the dineutron radius is given by:

$$\langle r_h^2 \rangle = \langle r_{2n}^2 \rangle + \langle r_{di-n}^2 \rangle \tag{2.10}$$

Using Equations 2.6 – 2.10, the distance between the two neutrons and the distance of the center of mass of the two halo neutrons from the core can be deduced which will allow us to understand the average geometric correlation in two-neutron halos.

2.4 Formulation of meson exchange theory

The theory of nuclear force as an exchange force has a long history summarized in Table 2.1 based on the seminal idea by Yukawa [47], who introduced the concept of massive particle exchange, π meson to explain the nucleon-nucleon interaction. Although the one-pion exchange was useful in explaining the *NN* scattering data, the results were ambiguous when the contributions from the two-pion exchange were included.

The one-pion exchange model developed in the 1950s was not successful as the pions are dynamically constrained by chiral symmetry, an understanding gained only at the beginning of the 21^{st} century. In the early 1960s, the discovery of heavy mesons

Table 2.1: History of nuclear force theory [48].

Year	*Theory*
1935	Meson theory by Yukawa
1950s	The "Pion Theories" One-pion exchange: good, Multi-pion exchange: failure
1960s	Many pions $\equiv$ multi pion resonances: σ, ρ, ω Succesful description by One-Boson-Exchange model
1970s	Progress in meson theory: 2π exchange models Paris, Bonn, Stony Brook, Partovi-Lomon.
1980s	Discovery of **QCD**: Quark models.
1990s	Discovery and advances in **Effective Field Theory**: Weinberg, van Kolck.. .
21^{st} Century	**Development of Yukawa's meson theory!** with *constraints on chiral symmetry.*

led to the emergence of the one-boson-exchange (OBE) model which includes the exchange of multi-pion resonances. However, the weakest link in the OBE model is the scalar-isoscalar σ or ϵ boson, having contentious empirical evidence.

Vast theoretical efforts were made in search of realistic calculation of 2π exchange. During these efforts, various *NN* potentials were constructed based on meson-exchange theory, namely, Nijmegen-I, Nijmegen-II, Reid [49], CD-Bonn [50] and Argonne-V18 (AV18) potentials [51]. The *NN* potential successfully described the properties of two-nucleon systems. The experimental binding energies of three-nucleon systems (^{3}He, ^{3}H) and four-nucleon system ^{4}He were underestimated by the *NN* potential models [52]. The underestimation of binding energies of three or more nucleon systems in the *NN* potential model is attributed to the fact that the nucleons are treated as point particles, which disregards their internal quark structure. Nucleons are finite-mass composite particles, which can be excited to resonances when three or more nucleons interact with each other. Therefore, the residual three-nucleon force (3NF) is unavoidable for point masses. The first attempt to describe this effect was made by Fujita and Miyazawa, in which the 3NF can be visualized as an exchange of two pions, extending Yukawa's meson exchange formulation [53]. 3NF mechanism is an exchange of two

Table 2.2: Predicted binding energies in light nuclei using NN (AV18) potential and NN+3N potentials. Estimation improves with the inclusion of 3N potential [56].

Potential	^{3}H	^{3}He	^{4}He	^{7}Li	^{8}Be
AV18	7.61 (1)	24.07(4)	23.9(1)	31.6(1)	45.6(3)
AV18+UIX	8.46 (1)	28.33(2)	28.1(1)	37.8(1)	54.4(2)
AV18+IL2	8.43 (1)	28.37(3)	29.4(1)	37.8(1)	54.4(2)
Experiment	8.48	28.3	29.27	39.24	56.5

pions between three nucleons with the central nucleon exciting to an isobaric state, which is de-excited by the scattering of a third nucleon as shown in Figure 2.4a. In

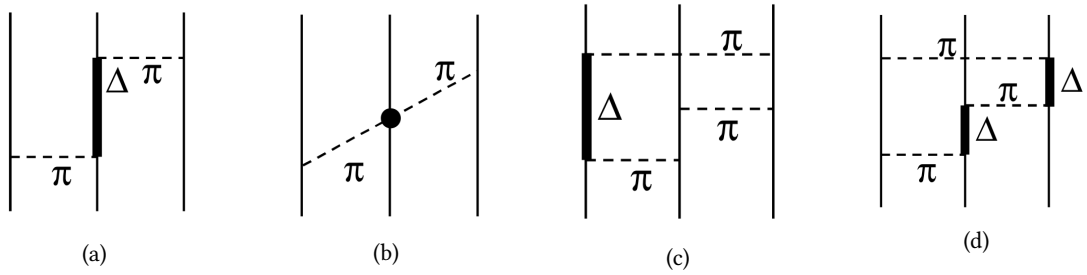

Figure 2.4: 3NF models (a) The Fujita-Miyazawa 3NF involves the excitation of the nucleon to a δ particle and Δ 1232 MeV (b) S-wave excitation in a two-pion exchange (c) and (d) Intermediate states with one or two Δ excitation states mediated via a three-pion exchange [54].

addition to this, several other processes contributed to the three-nucleon potential as shown in Figure 2.4(b-d). Several nuclear models based on three-nucleon potential have been developed including Urbuna IX (UIX) [55], Illinois [56], Tucson-Melbourne (TM) [57, 58] and the Brazil models [59]. The Urbana potential in combination with the two nucleon potential (AV18) improved the binding energy but as A increases it underestimates the binding energies for most of the nuclei. Table 2.2 shows the results of different models used to determine the binding energies.

The frequently used *NN* interaction with the inclusion of 3N potential has been successfully used to describe the properties of light nuclei. However, with the discovery of QCD, the meson exchange formulation resorted to the basic model of nuclear theory i.e., assuming nucleons as the point particles. A new theoretical effort was made to derive the nuclear force from the underlying fundamental theory QCD. The formulation of QCD provided the theoretical framework to describe the strong

interactions inside the nucleons which consist of quarks and gluons. Since QCD is non-perturbative at low energies relevant to nuclear physics, that poses a challenge in attaining a direct solution to the nuclear N-body problem.

2.4.1 Chiral effective field theory

The concept of chiral effective field theory (χEFT) [60] proved to be a major milestone in the field of nuclear physics, a low-energy effective representation of QCD. The most general Langrangian in terms of the chosen degrees of freedom (nucleons and pions) is the starting point for χEFT with terms in accordance with the broken chiral symmetry of QCD and allowed interaction mechanisms. The nuclear potential determined using

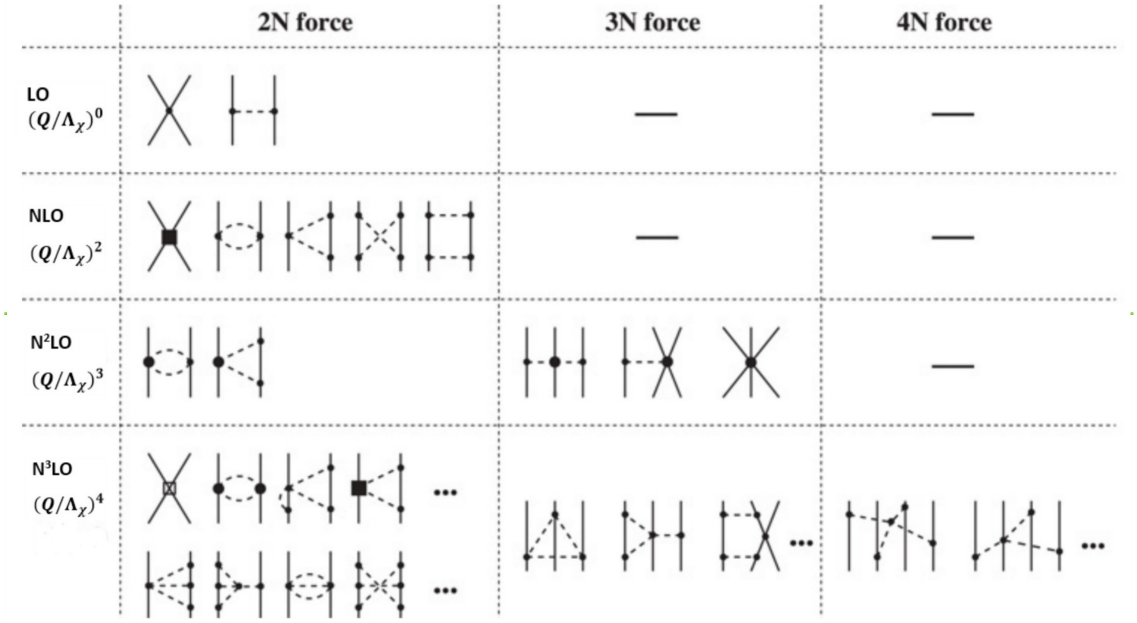

Figure 2.5: The nuclear potential derived from Chiral effective field theory for nuclear forces. The different contributions from terms at leading order, next-to-leading order, next-to-next-to-leading order, and next-to-next-to-next-to- leading order are shown diagrammatically. The pion exchange and the nucleons are represented by solid and dashed lines, respectively [62].

this Lagrangian generates an infinite number of terms and needs to be truncated using a power-counting scheme given by Weinberg [61]. Weinberg power counting is a systematic way of expanding the QCD Lagrangian in the powers of $(\frac{Q}{\Lambda_\chi})^\nu$, where Q

denotes the pion mass/momentum and $\Lambda_\chi \sim 1$ GeV is the chiral-symmetry breakdown scale. Power counting is an order by order scheme and for a given power ν of the expansion scale Q in each interaction, the number of contributing terms are finite and can be calculated for a given order ν.

The hierarchy of nuclear forces is evident from the first diagram in Figure 2.5, two-nucleon force (2NF) is much stronger than the 3NF as the contribution from the NN potential appears at the order ν = 0, whereas for 3NF it appears at the order ν = 3. Renormalization techniques are used to absorb high energy physics in coefficients called low-energy constants (LECs). The LECs are fitted to experimental data. The χ EFT theory has provided a more fundamental basis for the basic nuclear force model, by tying the concept of EFT to low-energy QCD [63].

The EFT for halo nuclei, $Halo\ EFT$ has been used to compute the exotic properties like binding energies, radii, Coulomb dissociation of halos of the s-wave and p-wave type [64]. The root mean square (rms) matter radii determined by Tanaka $et\ al.$ [25] could only be consistent if it is weakly bound (S_{2n} < 0.02 MeV) after constraining S_{1n} from Mosby $et\ al.$ [65]. The recently developed EFT of a two-neutron halo nucleus showed the universal properties of weakly bound halo nuclei [66]. Halo EFT was used to calculate the point-matter and point-charge radii, and the inter-neutron distances of the two-neutron halo nuclei ^{11}Li, ^{14}Be, and ^{22}C using the next-to-leading order (NLO) by treating them as an effective three- body system [67]. Halo EFT complements the state-of-the-art nuclear theory $ab\ initio$ by correlating the different halo observables. This unified framework of Halo EFT and the $ab\ initio$ theories can be used to test calculations and measurements of different observables to predict halo properties.

2.4.2 Reach of realistic *ab initio* calculations

The $ab\ initio$ models have made tremendous progress since the development of Similarity Renormalization Group (SRG) techniques [68] and nuclear many-body methods.

Ab initio coupled-cluster theory based on NN and 3NF from χEFT is used to compute the energies of the ground and low-lying states in neutron-rich carbon isotopes [69]. The no-core shell model first introduced the valence-cluster expansion [70], which is used to facilitate an effective shell-model Hamiltonian in a valence space from *ab initio* coupled-cluster theory. The Hamiltonian constructed via this approach is known as the coupled-cluster effective interactions (CCEI). The ground and excited state energies of carbon isotopes are obtained with good accuracy demonstrating the power of *ab initio* coupled-cluster theory.

In addition to the binding energies, the proton distribution radius is one of the fundamental observables that will test the realistic reach of various *ab initio* models. Various coupled-cluster methods were used to extract the point proton and radii for C isotopes; single and double excitations for the closed (sub-) shell nucleus ^{14}C [72], particle-removed or attached equation of motion used to assess the open-shell nuclei ^{13,15}C [73,74] and the CCEI method to obtain the ground state [69] and intrinsic radii of $^{16-19}$C. The interaction NNLO$_{sat}$ from χEFT at next-to-next-leading order (NNLO) is employed that simultaneously optimizes the LECs for the contributions up to NNLO for both two and three nucleon interactions by including data on charge radii and binding energies of selected nuclei up to ^{25}O. The recently developed NNLO$_{sat}$ also successfully predicted ^{48}Ca radii and these were in agreement with the experimental data [75]. The two-nucleon chiral interaction NNLO$_{opt}$ which does not include 3NFs was also used to compute the radii in this work.

The proton R_p distribution radii of ^{14}Be [45], $^{12-17}$B [43] and $^{12-19}$C [46, 71] were determined from the charge-changing cross-section measurement at GSI, Darmstadt. Recently, the smallest Spin Orbit (SO)-originated magic number was obtained at the proton number six in the carbon isotopes by Tran $et\ al.$ [37], by systematically analyzing the point proton distribution radii, electromagnetic transition rates and atomic masses of light nuclei. The proton distribution radii observed in these experiments

are explained by the state-of-the-art nuclear theory with chiral NN and 3N forces. The point proton radii of carbon isotopes computed with *ab initio* coupled-cluster

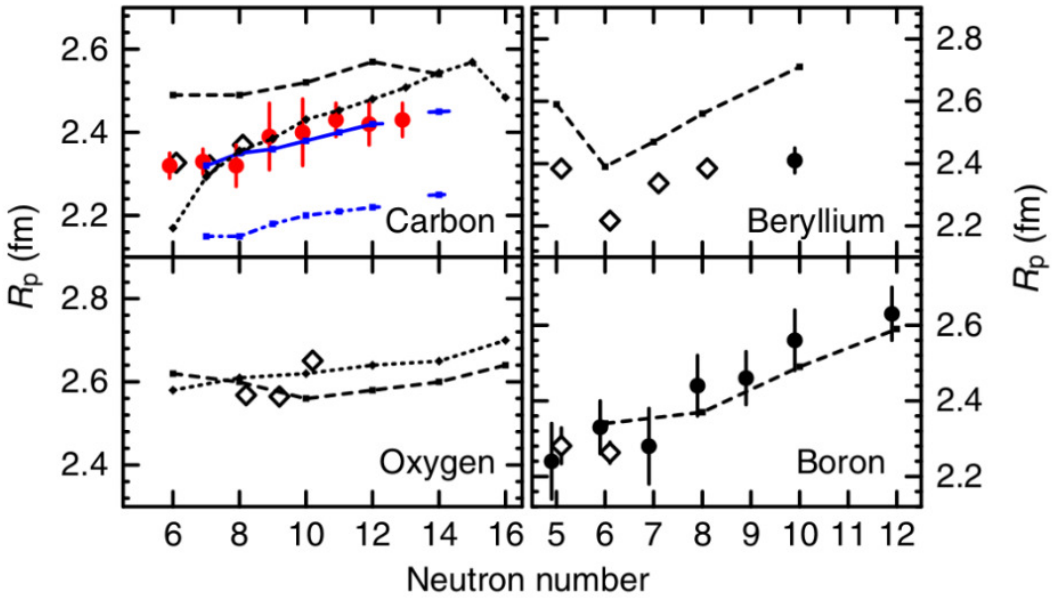

Figure 2.6: R_p from *ab initio* coupled-cluster computations using the chiral interaction NNLO$_{sat}$ and the two-nucleon interaction NNLO$_{opt}$ are shown by the small blue symbols with solid line and dash-dotted lines, respectively. The experimental R_p derived from charge-changing cross-section measurements from this work and the recent work is shown by red and black-filled circles [43, 45, 46, 71]. The error bars for the red-filled circles represent the statistical, systematic uncertainties and also the assumption of density distributions. The error bars for the othe experimental work is obtained from the literature. The predictions made from AMD [76] and RMF [77] models are shown by small symbols connected with dashed and dotted lines, respectively [37].

(CC) calculation with NNLO$_{sat}$ and the NN-only NNLO$_{opt}$ interaction are compared to the data as shown in Figure 2.6. The overall agreement between theoretical and experimental proton distribution radii in this analysis is good for the chiral interaction with 3N forces NNLO$_{sat}$. The chiral interaction with two nucleon force NNLO$_{opt}$ underestimates the radii by 10 %, which shows the significance of the simultaneous optimization technique used in NNLO$_{sat}$ and the 3N forces.

The carbon isotopes draw interest due to the presence of neutron halos in ^{15,19}C and ^{22}C. It will be interesting to see the evolution of the proton distribution of neutron-rich C isotopes (^{20,22}C). There are no data on proton radii of ^{20,22}C, which are required to constrain structure models and the nuclear interaction.

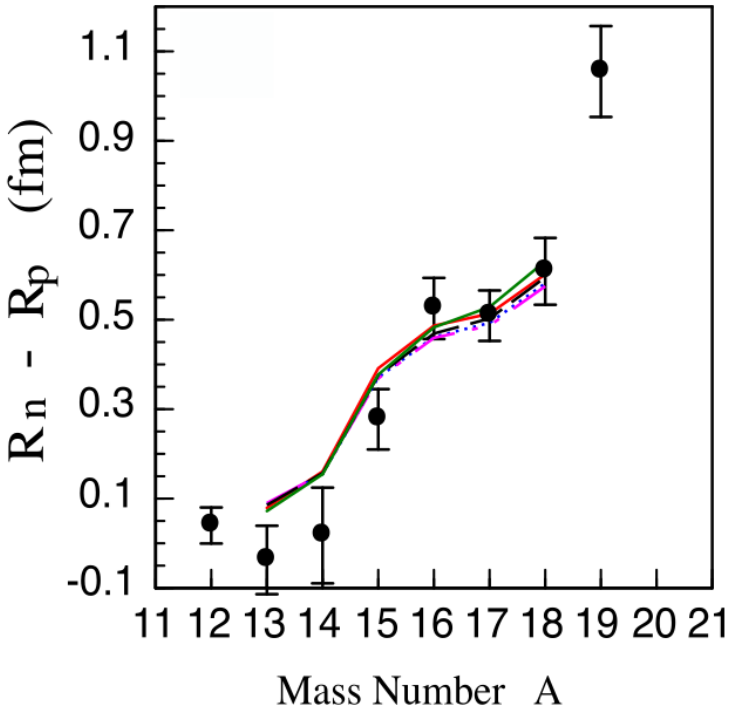

Figure 2.7: Measured neutron skin thickness for $^{12-19}$C are compared to the predictions using the different interactions (EM1 (blue curve), EM3 (pink curve), EM4 (black curve), EM5 (green curve) and $NNLO_{sat}$ (red curve) [46].

As discussed in Section 2.3, the proton radii together with the matter radii can be used to determine the neutron radii as shown in Equation 2.5. The neutron skin thickness, ΔR_{np}, defined as the difference of point neutron and proton radius. The neutron skin thickness measured for the carbon isotopes ($^{12-19}$C) [46] is shown in Figure 2.7. The measured neutron skin thickness is compared with the Entem and Machleidt (EM) and $NNLO_{sat}$ interactions. The predictions made by the different interactions are in good agreement with the experimental data. As seen in Figure 2.7, a very thick neutron skin is developing in the neutron-rich carbon isotopes. Therefore, the measurement of proton radius (R_p) of neutron-rich carbon isotopes (^{20,22}C) is needed to determine the neutron radii experimentally and observe the evolution of neutron skin thickness with increasing neutron-proton asymetry.

The Borromean halo ^{22}C was studied using a recently developed *ab initio* Gamow

in-medium similarity renormalization group (IMSRG) which includes the continuum via the complex-energy Berggren basis obtained by the Gamow-Hartree-Fock with chiral interactions [78]. The chiral interactions with two nuclei NNLO$_{opt}$ and three nuclei NNLO$_{sat}$ have been used in the calculations. The calculations were tested on the neutron-dripline nucleus ^{24}O in which the resonant states have been observed experimentally. The calculations obtained from this method are well in agreement with the experimental observations.

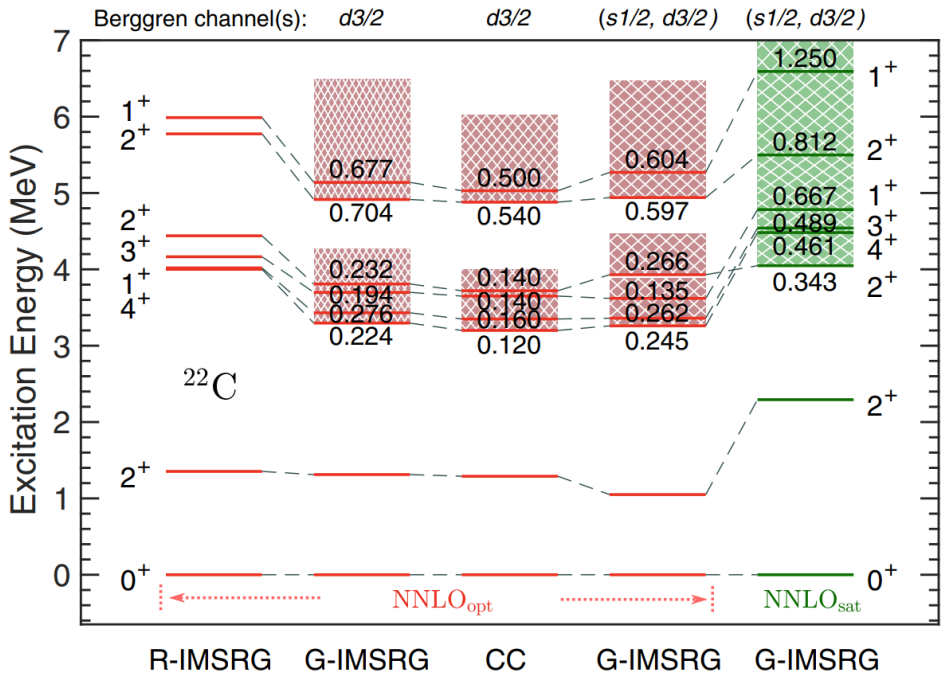

Figure 2.8: The excited states of ^{22}C calculated using the Gamow EOM-IMSRG with NNLO$_{sat}$ and NNLO$_{opt}$. CC calculation are used as benchmark for these calculations [78].

The Gamow IMSRG was employed to get the ground-state property by decoupling the continuum-coupled Hamiltonian of a closed shell nucleus with the ground state configuration. The decoupled IMSRG Hamiltonian was performed to obtain the excited states shown in Figure 2.8. Two types of calculations were performed to see the effect of continuum, by analyzing the role $s-$ channel: (a) discrete $s-$ states with real energy Hartree-Fock (HF) states (b) Bergren $s-$ states with the continuum Gamow-

Hartree-Fock (GHF) $s-$ wave. The matter radii obtained are 2.798 fm and 2.928 fm from the discrete real energy HF state and the continuum GHF $s-$ wave, respectively. The calculations with the nucleon forces NNLO$_{sat}$ (NN+NNN) interaction derived a radius of 2.983 fm and 3.139 fm for HF s states and GHF $s-$ wave, respectively. As explained above for Ref. [46], NNLO$_{sat}$ gives a good description of radii and the chiral interaction with two nucleon forces underestimates the radii. The matter radius predicted from the relativistic mean-field model with a continuum gives a radius of 3.25 fm [33]. The large spatial extension of the density can be seen from the calcu-

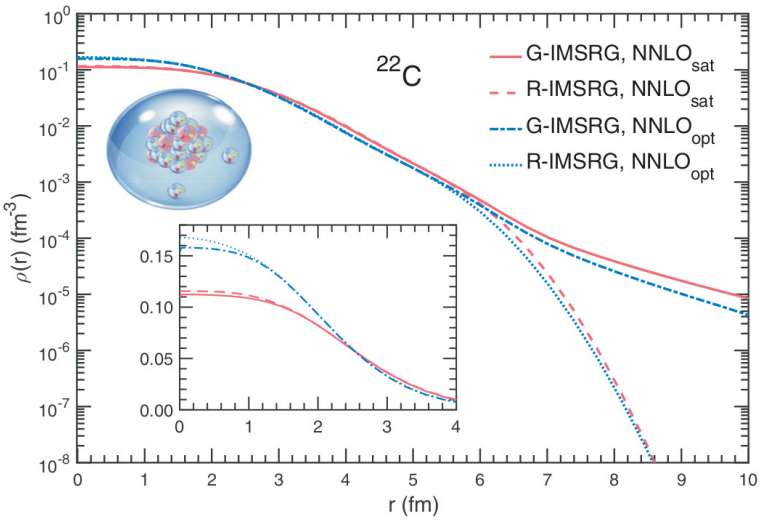

Figure 2.9: The ground-state densities calculated for ^{22}C are shown on a logarithmic scale. The real-energy HF calculation is indicated by R-IMSRG and G-ISMRG is the Gamow IMSRG calculation. The central region of the nucleus is shown in the inset [78].

lated $s-$ wave for the Borromean halo nucleus ^{22}C shown in Figure 2.9. The results obtained from different methods are benchmarked with the complex coupled cluster (CC) calculations. These results provide important information regarding the ground and excited states which can be the basis for future experiments.

2.5 Conventional methods for measuring the proton distribution radii

Measurement of interaction cross-section has been the most commonly used method to determine the matter radii of short-lived nuclei [25,26]. The model-independent interpretation of proton distribution inside a nucleus requires an electromagnetic probe. The methods for measuring the proton radii are summarized in this section.

2.5.1 Electron scattering

Rutherford concluded that the size of the nucleus is less than 10^{-14} m from α scattering experiments. Unlike α particles, the electron is a structureless point-like object which avoids the complexity of the strong interaction between the projectile and the target as they interact only electromagnetically. The scattering of electrons is one of the most powerful tools for revealing the internal structure of the nucleus. The elastic electron scattering provides precise information about the charge distribution in the nucleus. In Plane-Wave Impulse Approximation (PWIA), the differential cross-section for elastic scattering (with no spin or magnetic moment assumed for the target nucleus) can be divided into two factors, the Mott cross-section $d\sigma_{Mott}/d\Omega$ and the form factor squared [79]:

$$\frac{d\sigma}{d\Omega} = \frac{d\sigma_{Mott}}{d\Omega}|F_c(q)|^2 \tag{2.11}$$

In elastic electron scattering, the cross-section from a point-like particle of charge Z is given by the Mott cross-section:

$$\frac{d\sigma_{Mott}}{d\Omega} = \frac{(Z\alpha)^2\cos^2(\theta/2)}{4E^2\sin^4(\theta/2)} \tag{2.12}$$

where E is the energy of the electron, θ is the scattering angle and α is the fine-structure constant. The form factor is identified as the Fourier transformation of the

spatial charge distribution, $\rho_c(r)$, with q as the momentum transferred to the target from the projectile in the scattering process.

$$F_c(q) = \frac{1}{(2\pi)^{\frac{3}{2}}} \int \rho_c(r) e^{-i\vec{q}.\vec{r}} r d\vec{r} \tag{2.13}$$

The charge distribution $\rho_c(r)$ of a nucleus can be extracted by an inverse Fourier transformation of the measured charge form factor.

Charge radii or proton distribution radii of stable nuclei have been determined by measurements of electron scattering. The elastic scattering data for long-lived nuclei, ^{3}He and ^{14}C [80, 81] were analyzed. The study of nuclei far from the stability line by elastic electron scattering has not been reported yet as it requires long-half lives to prepare a sufficiently thick radioactive target. Self-Confining RI Ion Target (SCRIT) electron scattering facility at RIKEN RI beam factory, Japan has a novel internal target system with the aim of investigating the internal nuclear structure of nuclei far from the β stability line by electron scattering [82]. The nuclear charge density distribution of ^{132}Xe was determined via the electron scattering experiment [83]. Currently, this facility is preparing the first experiment to conduct electron scattering of rare isotopes.

2.5.2 Muonic atom x-ray spectroscopy

Muons are a fascinating probe to study the charge distribution of a nucleus. A negative muon beam is bombarded on a target material to form a muonic atom. When a negative muon is subsequently captured, it orbits the nucleus at a very small distance due it its higher mass compared to that of the electron. The atomic capture of muon is followed by a muon cascade from an initial excited state to the ground state with the emission of X-rays and Auger electrons. The charge radii of almost all stable elements have been determined using Muonic X-ray spectroscopy [84, 85] profiting from the high sensitivity of low-lying muonic transitions to the properties of the nuclear charge distribution. Muonic X-ray spectroscopy has not been used to investigate the

radioactive nuclei since this experimental method requires several tens of milligrams of the target. Although researchers have made strong efforts towards the possible formation and investigation of radioactive nuclei [86]. The idea is to extract the nuclear charge radii of radioactive isotopes that can only be facilitated with several micrograms of the target.

2.5.3 Isotope shift

The charge distribution inside a nucleus can be extracted from isotope shifts for very light elements. Among the three method — electron scattering, muonic atoms and isotope shift — isotope shift measurements are mostly used to determine the charge radii of nuclei far from stability. The two major components of isotope shift which enable to decode the charge radius information are the mass shift (MS) and the volume shift or field shift (FS). The change in nuclear mass between two isotopes is the mass shift and the difference in the charge distribution inside a nucleus is the volume shift. The measurement of charge radii using isotope shift measurements in lithium isotopes provided a nuclear-model-independent value of charge radius of the Borromean halo nucleus, ^{11}Li [28, 87]. However, in the case of light nuclei, the MS by far dominates and decreases rapidly with increasing mass number as A^{-2}. The FS is predominant in the heavy elements, which increases with the nuclear charge number Z as $Z^2 A^{\frac{-1}{3}}$. Extracting the charge radius of light nucleus from isotope shift measurements is a complicated task and can only be performed on very simple and stable atoms consisting of no more than two electrons. To determine charge radius from the isotope shift measurements, a very accurate theoretical atomic structure calculation of the parts contributing to the MS of at least one reference isotope is also required. The difference of charge radius is deduced from the experimentally observed isotope shift and the atomic theory calculations. This approach was used in the determination of the ^{6}He nuclear charge radius, using the charge radius of ^{4}He measured by electron

scattering and muonic atom spectroscopy, and the difference of the charge radii from ^{4}He-^{6}He isotope shift measurement [42, 88]. A similar technique was used to determine the charge radii of Be [44] isotopes as shown in Figure 2.10. An interesting trend

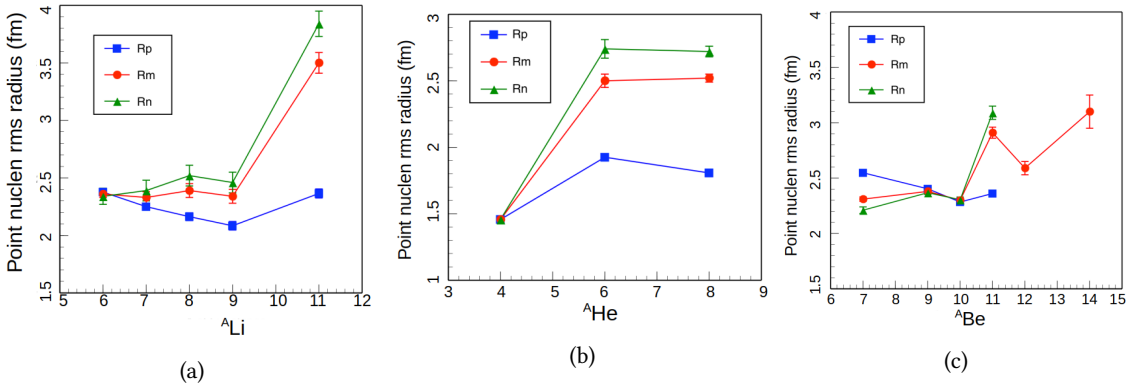

Figure 2.10: Rms radii of nucleon (R_m), proton (R_p) and neutron (R_n) (a) Li isotopes (b) He isotopes (c) Be isotopes. Figure adapted from [2].

is observed for an isotopic chain that the proton radius increases when a neutron halo is formed, namely ^{11}Li, ^{6}He, ^{11}Be. Such an increase suggests the movement of the core nucleus explained using "a core nucleus" + "halo neutron(s)" assumption in Section 2.3. Most strikingly, there is a decrease in charge radius from ^{6}He to ^{8}He even though the matter radius increases due to an increase in nucleon number. In Borromean halo ^{6}He, the correlated pair of neutrons moving against the recoil motion of the α like core smears the charge distribution, resulting in an increase in charge radius. On the other hand, in ^{8}He, the recoil effect is considered to be smaller due to possibly a spherical distribution of the four excess neutrons around the α like core. Therefore, the charge distribution is less smeared out in comparison to ^{6}He resulting in a smaller charge radius.

The charge radii of ^{41,51,52}Ca were determined using isotope shift measurements [89]. The charge radii of the radioactive calcium isotopes beyond $N = 28$ are unexpectedly larger than the theoretical predictions and thus challenges the doubly magic nature of ^{52}Ca. It has opened new intriguing questions on the evolution of nuclear

structure in unstable neutron-rich nuclei and how it influences the charge radius. The study of light neutron-rich nuclei with isotope shift requires low energy and high-intensity beams of short-lived isotopes which is quite challenging. Therefore, these nuclei have not been investigated by isotope shift. Many-body correlations between the electrons in the atoms make the atomic structure calculations difficult.

2.6 Charge-changing cross-section measurement

An important breakthrough was achieved in the 1980s due to the remarkable development towards the production technique of unstable nuclei, which led to the discovery of the neutron-halo structure [8]. The nuclear rms radii were determined by applying the Glauber model. Since then, interaction cross-section σ_I measurements have made significant contributions to unstable nuclear physics [90]. The charge-changing cross-section (σ_{cc}) is related to the point proton distribution in a nucleus. In 1990, the σ_{cc} was measured by Webber *et al.* [91] and Cummings *et al.* [92], which is the total cross-section of all processes that change the proton number of a nucleus. The σ_{cc} of stable isotopes were determined to interpret the interstellar production of secondary fragments during cosmic-ray propagation in the galaxy. The proton distributions of neutron-rich lithium isotopes were investigated by Blank *et al.* [93] but no attempt was made to determine the proton radii. The total charge-changing cross-sections of stable and radioactive nuclei (^{14}Be, $^{10-19}$Be, $^{12-20}$Be, $^{14-23}$Be, $^{16-24}$Be and $^{18-27}$Be) were measured by Chulkov *et al.* [94]. The σ_{cc} data obtained for stable isotopes in this experiment was not explained by the proton radii determination using electron scattering and also were greater than σ_{cc} values determined by Webber and Cummings. The proton radii were not extracted from the measured σ_{cc} yet. Tanihata *et al.* [2] bridged the gap by extending the Glauber model framework to the measured charge-changing cross-section. The feasibility of extracting the point proton distribution from σ_{cc} measurements was illustrated through comparisons with the results

from the isotope shift method.

2.6.1 Finite range Glauber model

One of the advantages of measurement of the σ_{cc} is that the cross-section can be measured for most of the nuclei using the same setup as the reaction or interaction cross-section that plays an integral role in deriving the matter distribution inside a nucleus. A theoretical tool based on the Glauber model framework [95] is well established for the reaction cross-section of projectile-target collisions integrated by the reaction probability with respect to the two-dimendional impact parameter vector $\boldsymbol{b}$,

$$\sigma_{\mathrm{R}} = \int [1 - T(\boldsymbol{b})] db \tag{2.14}$$

where T($\boldsymbol{b}$) is the transmission function, which is the probability that the projectile will pass through the target without any interaction after the projectile-target collision at $\boldsymbol{b}$. There is no role of neutrons in charge-changing cross-section, as the interaction is between projectile's protons with the nucleons of the target. The desired isotope of interest is selected as the incoming beam, the production of events after the target is from proton transfer reactions where one proton is added to the nucleus. These reactions do not involve the protons from the desired isotope and needs to be subtracted to measure the charge-changing cross section. The σ_{cc} is given by:

$$\sigma_{\mathrm{cc}} = \int db P_{\mathrm{cc}}(\boldsymbol{b}) \tag{2.15}$$

where $\mathrm{P}_{cc}(\boldsymbol{b})$ is the probability of charge changing reaction at the impact parameter $\boldsymbol{b}$. $\mathrm{P}_{cc}(\boldsymbol{b})$ is calculated using Optical Limit Approximation (OLA) [95–97]. The evaluation of the Glauber model within OLA describes the probability of charge-changing cross-

section [71],

$$P_{cc}(\boldsymbol{b}) = 1 - exp\left(-2\sum_{n=p,n}\int\int d\boldsymbol{s}d\boldsymbol{t}T_{\mathrm{P}}{}^{(\mathrm{p})}(\boldsymbol{s})T_{\mathrm{t}}{}^{(\mathrm{N})}(\boldsymbol{t}) \times Re\Gamma_{pN}(\boldsymbol{b}+\boldsymbol{s}-\boldsymbol{t})\right) \quad (2.16)$$

where, $\boldsymbol{s}$ is the two-dimensional vector of the projectile's single-particle coordinate, $\boldsymbol{r}$, measured from the projectile's c.m. coordinates and the target nucleus 2-d vector, $\boldsymbol{t}$ is also defined in the same manner. $\mathrm{T_P}{}^{(\mathrm{p})}(\boldsymbol{s})$ is the thickness function of the projectile's proton density $\rho_p^{(p)}(\boldsymbol{r})$ [40]:

$$T_P^{(p)}(\boldsymbol{s}) = \int dz\rho_p^{(p)}(\boldsymbol{r}); \quad \boldsymbol{r} = (\boldsymbol{s}, z) \quad (2.17)$$

The finite-range profile function, $\Gamma_{NN}(\mathbf{b})$ for the nucleon-nucleon (*NN*) scattering is parameterized as [30]:

$$\Gamma_{NN}(\boldsymbol{b}) = \frac{1 - i\alpha_{NN}}{4\pi\beta_{NN}}\sigma_{NN}^{tot}exp\left(-\frac{\boldsymbol{b}^2}{2\beta_{NN}}\right) \quad (2.18)$$

here, α_{NN} represents the *NN* scattering amplitude's ratio of the real to the imaginary part, β_{NN} is the finite range parameter i.e. the slope parameter of the *NN* elastic differential cross-section and σ_{NN}^{tot} is the total cross-sections for *NN* collisions. These parameters of NN profile functions are given in [30] for a wide range of energies. Applying this Glauber model framework using the measured parameters of nucleon-nucleon cross-sections and a target with a well-known density distribution, the point proton radii can be extracted.

As discussed in Section 2.6 the source and isotopic components of cosmic rays can be interpreted by the charge-changing cross-section [91]. The energy dependence of σ_{cc} was investigated by Suzuki *et al.* [71]. There is no role of neutrons in the direct process which is employed in our experiment (σ_{cc}^{dir}). The energy dependence of σ_{cc}^{dir} for a proton target in this kind of interaction is determined from the total cross-section of the proton-proton collision σ_{pp}^{tot}. The indirect process of determining

the σ_{cc}^{indir} depends on the neutron distribution as well. Therefore, the σ_{cc}^{indir} is also influenced by σ_{pn}^{tot} and its energy dependence becomes vital. The σ_{pn}^{tot} is slightly smaller than σ_{pp}^{tot} at energies E > 600 MeV and becomes larger at lower energies. Hence, the elemental cross-sections of the secondary fragments during cosmic ray propagation can be understood from basic systematics like the energy dependence, charge, and target. This can be an important input for understanding the nuclear physics involved in these peripheral collisions.

2.6.2 Point proton mean square radii determined from σ_{cc}

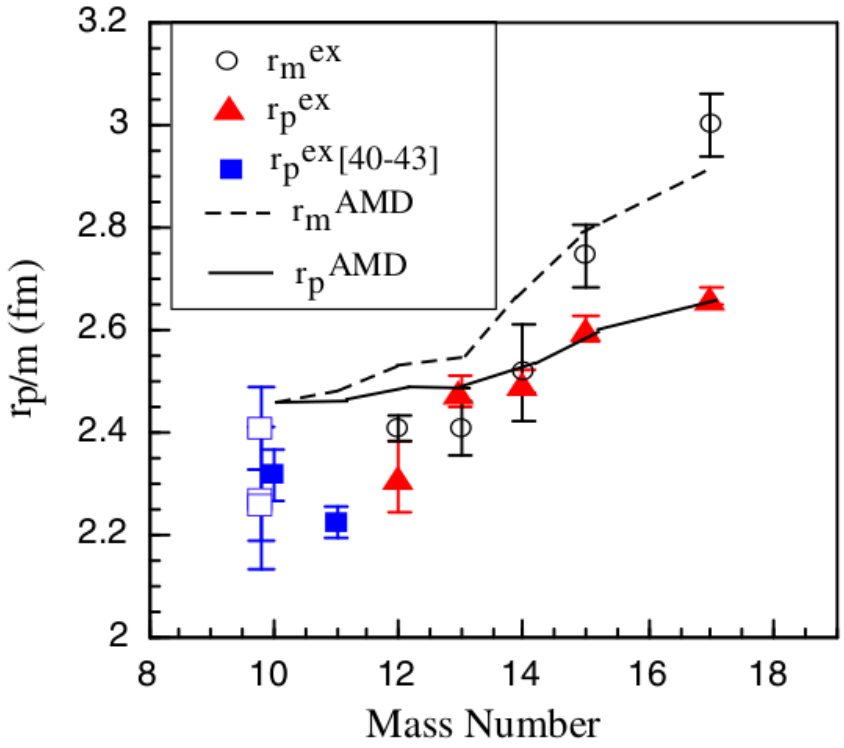

Figure 2.11: The filled triangles represent the measured R_p from σ_{cc} measurement of $^{13-17}$B and the open circles are R_m [43].

The Glauber model was successfully applied to determine the R_p from σ_{cc} measurements of neutron-rich isotopes which marked an important milestone in the study of nuclear radii. The R_p of $^{10-17}$B isotopes were determined for the first time using the σ_{cc} measurements by Estradé *et al.* [43]. Combining σ_R and σ_{cc}, a thick neutron surface

of 0.51 $\pm$ 0.11 fm was observed in ^{17}B. The measured R_p and R_m are shown in Figure 2.11. The proton and matter distribution radii calculated from the densities predicted by the antisymmetrized molecular dynamics (AMD) framework [98] are compared to the experimental measurements. Yamaguchi *et al.* [99] performed σ_{cc} measurements

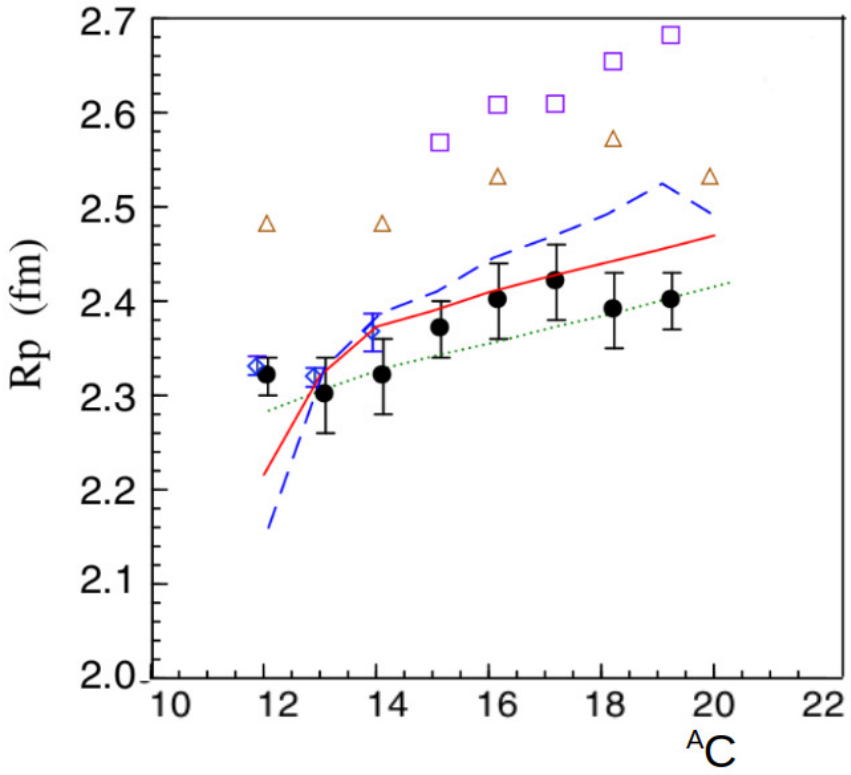

Figure 2.12: R_p (black filled circles) extracted from σ_{cc} measurement of $^{12-19}$C and R_p from e$^-$ scattering (blue open diamonds) [46]. The red solid line (blue dashed line) represent the relativistic mean field calculations with spherical (deformed) potentials. The green dotted line represents the Hartree-Fock calculations. The open triangles and open squares shows the results from AMD.

of ^{9,10}Be, $^{14-16}$C and $^{16-18}$O nuclides on carbon at 300A MeV. The zero range Glauber model was applied to determine the proton radii of these nuclides, but with a universal scaling of σ_{cc} over a wide range of A/Z. The matter radii of ^{15,16}C determined from the interaction cross-sections [27] and the deduced proton radii of ^{15,16}C were used to derive the neutron matter radii of these nuclei. It revealed a systematic evolution of proton radii and the neutron skin effect for these carbon isotopes. The finite range Glauber model was successfully applied to neutron-rich C isotopes to extract the point

proton radii at 900 MeV by Kanungo *et al.* [46]. A good agreement is seen for $^{12-14}$C R_p determined using e^- scattering and the σ_{cc} measurements as shown in Figure 2.12. The neutron skin among the C isotopes evolves with neutron-proton radii difference of 0.5 fm in ^{15}C to 1 fm in ^{19}C. The halo radius of a heavy one neutron-halo ^{19}C was derived to be 6.4 ± 0.7 fm, which shows the existence of a more prominent halo compared to ^{15}C, 4.2 ± 0.5 fm. The R_p and R_m determined for $^{13-19}$C (Figure 2.6) are consistent with *ab initio* calculations, which are discussed extensively in Section 2.4.2.

Chapter 3

Experimental setup and techniques

The experiment was performed using the BigRIPS fragment separator and the Zero Degree spectrometer at the RI Beam Factory (RIBF) [100] to measure the charge-changing cross-sections of the neutron-rich carbon isotopes. RIBF is a radioactive ion beam facility operated by RIKEN Nishina Center, Japan. It boasts a new high-power heavy-ion accelerator consisting of three ring cyclotrons, fixed frequency (fRC), intermediate stage (IRC) and superconducting cyclotron (SRC) which can boost energies of the beams up to 440A MeV for light ions and 350A MeV for heavy ions.

3.1 Radioactive Ion beam production at RIBF

Since the emergence of RI beams, scientists have been able to shed more light on the ultimate picture of nuclei and enhance their knowledge of nuclear phenomena. RIBF is an in-flight facility and the secondary beams are produced by the projectile fragmentation. Secondary beams produced are not sensitive to the chemical properties and half-life of the isotopes of interest. The projectile fragmentation technique requires a combination of a primary beam, a target, a mass separator, spectrometer and a beam transport system. The RI beams of ^{20,22}C are produced via projectile fragmentation reaction after the high energetic primary beam of ^{48}Ca (345A MeV) interacts with a

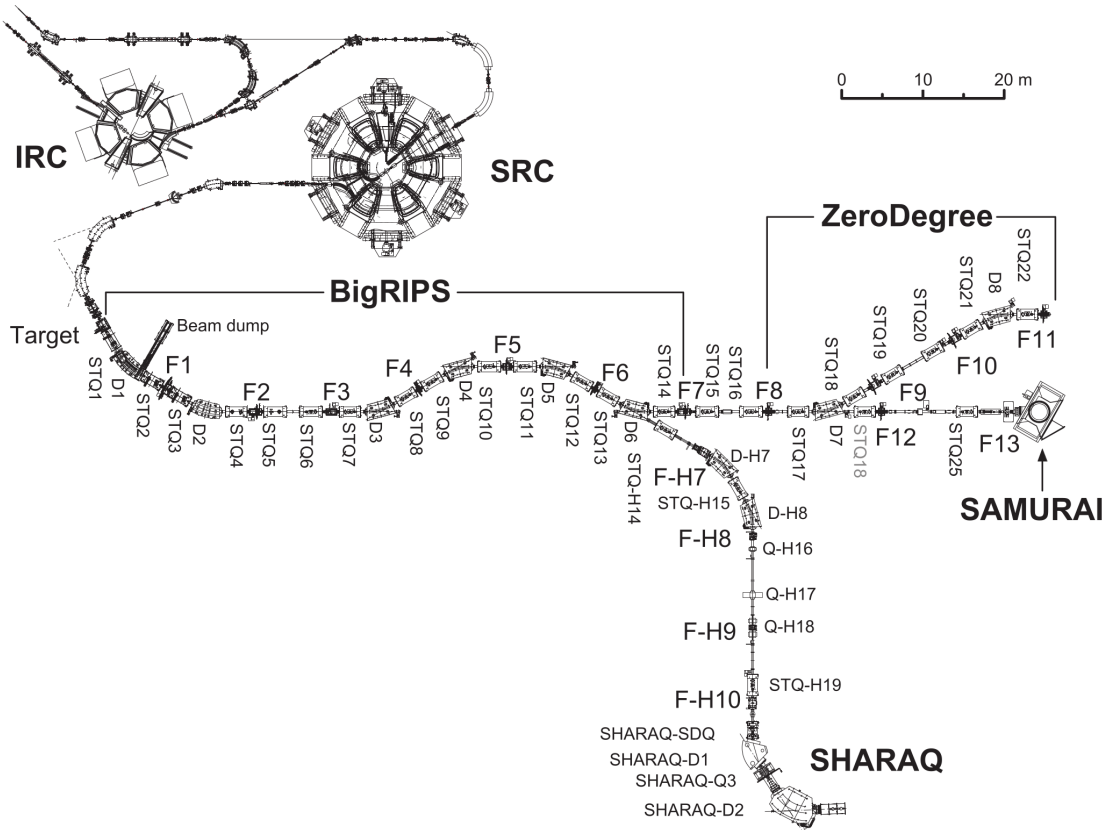

Figure 3.1: The schematic view of RIBF at RIKEN Nishina Center [103].

10 mm thick rotating ^{9}Be target. A schematic view of the RI Beam Factory at Riken Nishina Center is shown in Figure 3.1.

3.2 BigRIPS separator

BigRIPS separator is a high-resolution magnetic spectrometer designed to deliver isotopically selected fragments using a two-stage structure characterized by large-ion optical acceptances and particle identification with a total length of 78.2 m [103]. The first stage of the BigRIPS is operated in separator mode as shown in Figure 3.2 used to produce the projectile fragments and separate the nuclei of interest with an energy degrader.

The second stage of BigRIPS is a spectrometer designed to identify the fragments

for secondary reaction studies. The angular and momentum specifications of the BigRIPS separator are listed in Table 3.1. It has an acceptance range of ±40 mr horizontally and ±50 mr vertically and the momentum acceptance is ±3%.

Table 3.1: Specifications of the BigRIPS [103].

Separator stage	1st stage	2nd stage
Configuration	F0–F3	F3–F7
Horizontal angular acceptance $\Delta\theta$(mr)	±40	±40
Vertical Angular acceptance $\Delta\phi$(mr)	±50	±50
Momentum acceptance δ(%)	±3	±3
Momentum Dispersion P/ΔP(cm/%)	-2.14	+3.17
Max. Rigidity Bρ (Tm)	9.6	8.8
Momentum Dispersive Foci	F1	F4–F6
Doubly achromatic Foci	F2,F3	F7
Path Length (m)	31.6	46.6

The first stage consists of two 30° room-temperature dipole magnets (RTDs) and a set of large-aperture superconducting quadrupoles (STQs) for large acceptances encapsulating the dipoles. The BigRIPS separator is designed specifically to enhance the accessible region of secondary reactions which allows one to collect the fragments with higher efficiencies. BigRIPS separator is a two bend achromat system with momentum-dispersive focus at F1 and achromatic focus at F2 transporting the separated fragments to the second stage as shown in Figure 3.2.

The spectrometer (second) stage forms a four-bend achromat system consisting of four dipoles and eight STQs encapsulating the dipoles from the experimental focus F3 to F7. The intermediate focal planes F4, F5, F6 are momentum-dispersive, while F3 and F7 are achromatic. Several isotopes are produced in the secondary reactions due to the mixture of different charge states. The spectrometer stage is employed to identify the isotopes of interest using the technique of time of flight (TOF), energy loss (ΔE) and magnetic rigidity based on an event-by-event information. The beam transport system following the BigRIPS separator works as a forward spectrometer, named Zero Degree spectrometer [101, 105].

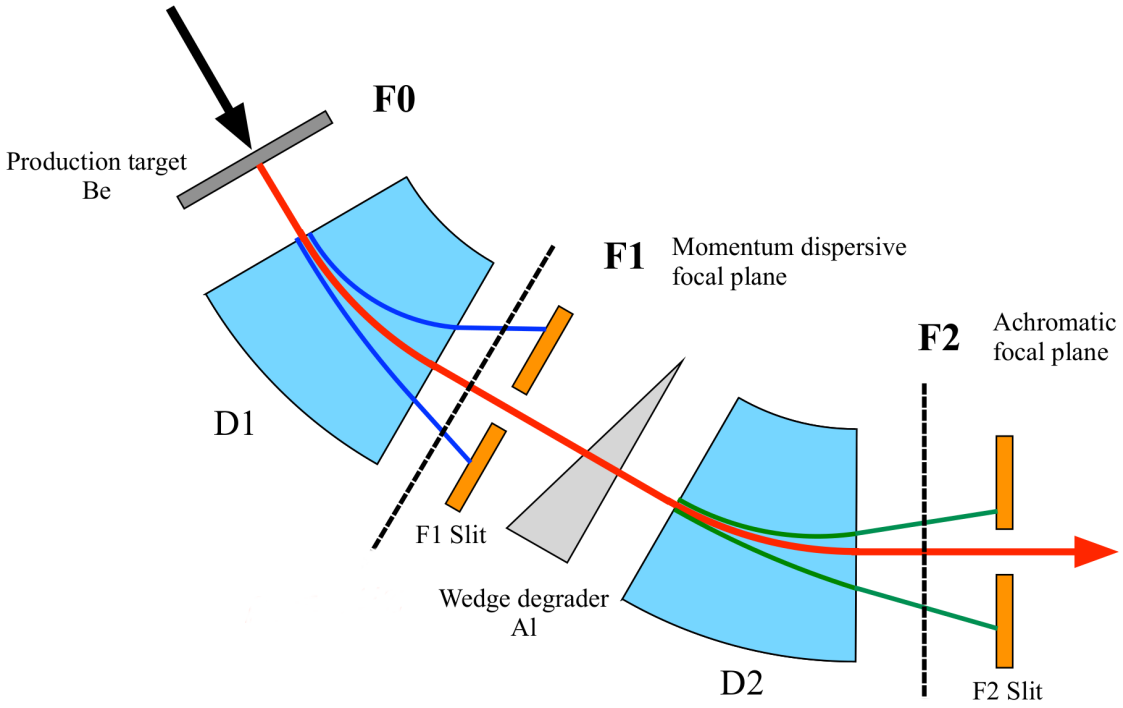

Figure 3.2: Schematic drawing of the separation of RI beams in the 1st stage of BIGRIPS [104].

3.3 Zero Degree Spectrometer

Figure 3.1 shows the schematic representation of the Zero Degree spectrometer (ZDS) consisting of two dipoles and 6 STQs from experimental focus F8–F11. ZDS has an identical layout of the magnets as the BigRIPS, having the momentum-dispersive focal planes at F9 and F10, with the final focus F11 being fully achromatic. The quadrupole magnets (STQ15 and STQ16) in the section F7–F8 connecting the BigRIPS and ZDS are used to determine the focusing ion-optical conditions at F8, where a secondary target is placed. Similarly, for quadrupole magnets STQ20, 21 and the dipole D8 in section F9-F11 are tuned for the delivery of the secondary reaction products to the achromatic focus at F11, where the reaction target C (2.5 g/cm^2) was placed.

The ZDS is fixed at zero degree for the secondary reaction studies with RI beams, to identify and analyze the projectile fragments after the secondary target at F8. Particle identification scheme similar to the BigRIPS separator based on the TOF-Bρ-ΔE is

employed in the ZDS with the trajectory reconstruction.

3.4 Measurement of mass-to-charge ratio

The BigRIPS separator is employed to separate out the secondary beams as shown in Figure 3.2. The mass-to-charge ratio is determined using the Lorentz equation, which describes the motion of charged particles in magnetic dipole fields:

$$F = qvB = \frac{mv^2}{\rho} = \frac{\gamma m_0 v^2}{\rho} \tag{3.1}$$

where ρ is the radius of the circular path taken by the particle of velocity v in a magnetic field B, q is ionic charge state of the secondary beam, m_0 is the rest mass and γ is a Lorentz factor. The equilibrium between the Lorentz and centrifugal force can be expressed by:

$$\frac{m_0}{q} \approx \frac{A}{Z} = \frac{B\rho}{u\beta\gamma c} \tag{3.2}$$

where u is the atomic mass unit equal to 931.494 MeV/c^2 and the charge equal to Z as the nuclide of interest is fully stripped. The magnetic rigidity $B\rho$ is defined as

$$\chi = B\rho = \frac{p}{q} \tag{3.3}$$

where p and q are the momentum and charge of the particle, respectively. In a given magnetic field, the particle with higher momentum will be bent less as it travels through that field. The variable χ is inversely proportional to the charge of the particle, therefore, higher Z particle will be bent more as it travels through the magnetic field.

The BigRIPS and ZDS are operated in the dispersion matched mode where the dispersion of the first stage is compensated by the dispersion of the second stage. For a particular A/Z fragment, corresponding to the χ value of F0–F1 (dispersive

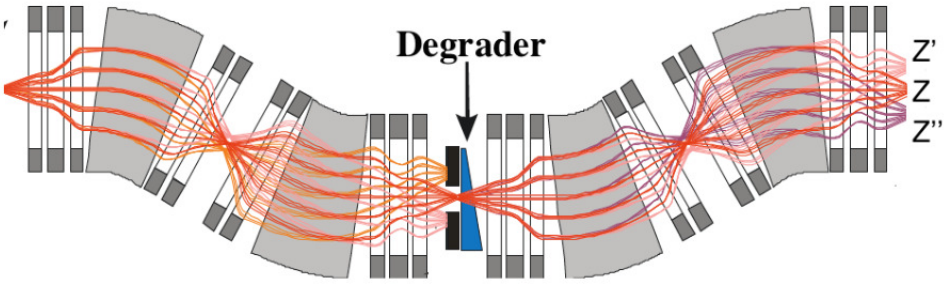

Figure 3.3: Schematic view of ion-optics on passing through a degrader [40].

focal plane), F2–F3 (achromatic focal plane) is configured to have a value (χ) which converges it back to the same horizontal position as shown in Figure 3.3.

A technique called momentum-loss achromat is employed to isotopically separate the fragments in flight by inserting achromatic wedge shaped energy degraders at the experimental foci F1 and F5 [106, 107]. The isotopes will have different velocities as it passes through the degrader as the energy loss of the particles is proportional to Z^2/v^2. The fragments with the same A/Z will be separated in position as shown in Figure 3.3.

The achromaticity of the setup is preserved because of the wedge-shaped design of the degrader, as the fragments with higher velocity pass through more degrading material and the lower velocity passes through less. The slits are used to further reduce the contaminants coming from the reaction at F0 as shown in Figure 3.2.

3.5 Experimental Methodology

As discussed in the previous chapter, σ_{cc} cross-sections on a carbon target were determined using the transmission method. σ_{cc} is the cross-sections for the reactions after the target that changes the the proton number of the projectile nucleus. The number of incident nuclei is identified and counted by the total mass and the proton number (^{A}Z) on an event-by-event basis, before the reaction target. The nuclei transmitted through the breakup target at F11 without any charge-changing interaction $i.e.$ the

nuclei with the same proton number as the incident nuclei are identified and counted.

The intensity of the beam particles diminishes as they interact with matter. The reaction cross-section σ_R is the nuclide-changing reactions, where the number of interactions per unit time per unit area is proportional to the number of incident beam particles N_{in} and the number of target particles. The reaction cross-section, by the constant of proportionality is defined as [108]

$$N = N_{\text{in}} e^{-\sigma_R t} \tag{3.4}$$

where N is the number of particles unreacted after passing through the target, t is the number of target nuclei per cm^2. Analogous to the reaction cross-section, σ_{cc} is defined as:

$$N_{in} - N_z = N_{in} e^{-\sigma_{cc} t} \tag{3.5}$$

In Equation 3.5, N_z represent the particles that undergo a charge-changing reaction. Therefore, $N_{in} - N_z$ is the number of particles after the reaction target that do not undergo any change of charge. This is denoted by:

$$N_{sameZ} = N_{in} e^{-\sigma_{cc} t} \tag{3.6}$$

Counting the number of incident beam particles N_{in} and the particles with an unchanged charge (Z) N_{sameZ} gives the total charge-changing cross-section. The nuclei after the target with the same proton number (Z) or that greater than the incident beam can be represented by $N_{out \geq Z}$. Therefore, the equation of σ_{cc} is given by:

$$\sigma_{cc} = -\frac{1}{t} ln \frac{N_{out \geq Z}}{N_{in}} \tag{3.7}$$

In order to take into account the nuclear reactions in the non-target materials, a mea-

surement is needed without the target in the setup, which changes Equation 3.6:

$$\sigma_{cc} = \frac{1}{t} ln \frac{R_{Tout}}{R_{Tin}} \tag{3.8}$$

where R_{Tin} and R_{Tout} are the transmission ratios with and without the reaction target, $R_{Tin(Tout)} = N_{out \geq Z}/N_{in}$. Event-by-event counting of the selected incident beam is the main asset of this method. Therefore, there is no uncertainty involved while selecting the incident particles (N_{in}) of the isotope of interest.

3.6 Detector setup along the beamline

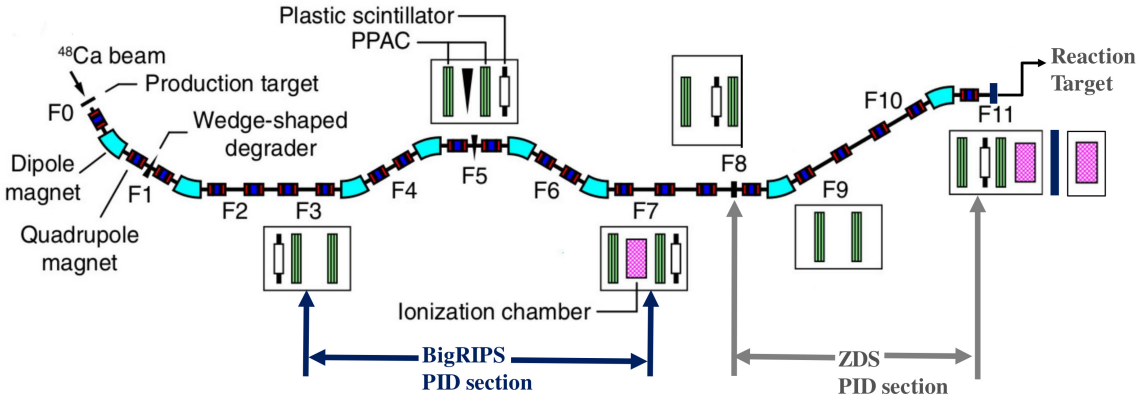

Figure 3.4: Schematic view of experimental setup [110].

The particle identification method based on TOF-$B\rho$-ΔE is employed to identify and count the incident nuclei before the reaction target. Various detectors are accommodated at different focal plane chambers along the beamline for particle identification. The magnetic rigidity determination requires the x position of RI beams, therefore each focal plane is equipped with two sets of position-sensitive parallel plate avalanche counters (PPAC) [109].

The trajectory reconstruction based on PPAC measurements enables one to fine-tune the ion optics, focusing and achromatic settings. Focal planes F7 and F11 are equipped with a multi-sampling ionization chamber (MUSIC) for providing ΔE infor-

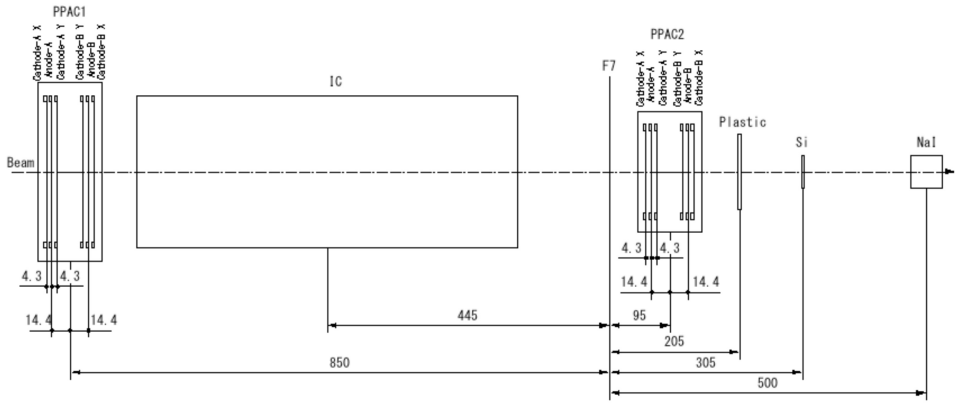

Figure 3.5: The geometrical information of detectors at *F7* given in mm [111].

mation. The time of flight was measured using the plastic scintillator detectors of 3 mm thickness located at F3, F7 and F11. A schematic view of the experimental setup with these detectors is shown in Figure 3.4.

MUSIC detectors are placed before and after a 2.5 g/cm^2 thick carbon reaction target. The geometrical information of the detectors at the achromatic focal plane F7 is shown in Figure 3.5.

3.7 Parallel Plate Avalanche Counter

The position of the particle in the horizontal (x) and vertical (y) directions were determined using the Parallel Plate Avalanche Counters (PPAC) [112]. PPACs are installed for trajectory reconstruction at each focal plane. The PPAC detectors have an effective thickness $\sim$ 30 mg/cm^2 which is quite small as compared to the other position sensitive detectors, such as multi-wire proportional counters [113] and a multi-wire drift chambers. PPAC is less than 1/10 of the amount of the other gaseous detectors, thereby having little or no influence on the delivery of RI beams. PPAC is a gas detector having no wires, thereby further reducing the hindrance in the transportation of the RI beams. Another key asset of PPAC detector is its durability and the ease of maintenance due to its simple structure. PPAC detector uses a delay-line readout

technique for position determination which helps to attain a high $B\rho$ resolution for particle identification, which not only enables the production and transport of the RI beams but also plays a key role in beam diagnostics of the BigRIPS and ZDS. A photograph after removing the window plate of PPAC detector is shown in Figure 3.6.

Figure 3.6: Photograph of the Double PPAC detector after removing its window plate [112].

The delay line PPAC consists of electrode strips connected to multi-tapped delay line and the position information is obtained from the time difference between signals from either end. An anode electrode is sandwiched between two x–axis and y–axis cathode electrodes having strips of width 2.4 mm with an inter-spacing of 0.15 mm between each strip. When a bias voltage ~1500 V is applied between the electrodes, induced electrons from incident ions are accelerated resulting in a Townsend Avalanche. The counter gas such as isobutane (C_4H_{10}) or perfluoropropane (C_3F_8) is used with a pressure of 3–50 Torr. As heavy ions pass through the detector, they create electron-ion pairs immediately causing an electron avalanche as shown in Figure 3.7. In comparison to the proportional counters there is no time delay before the electron

shower occurs. Therefore, the end result is a signal with excellent timing properties having rise and fall times of a few ns. Two double PPAC detectors are installed at

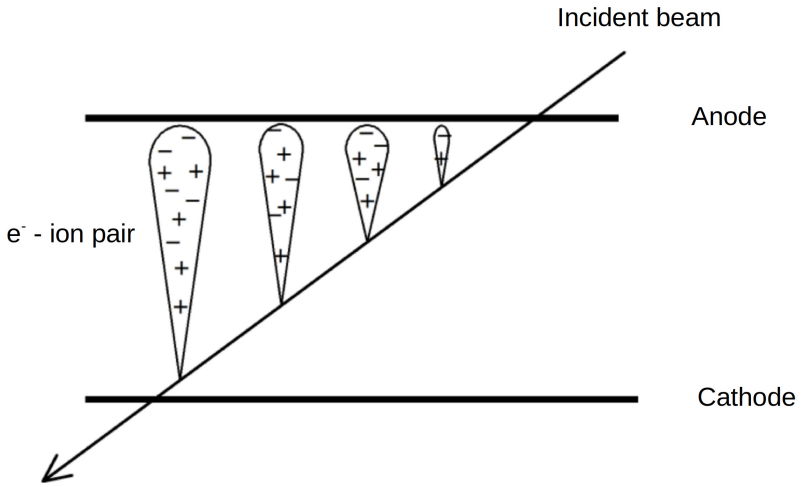

Figure 3.7: Operating principle of PPAC.

each focal plane in the BigRIPS separator and ZDS spectrometer. Each PPAC has two planes that are position sensitive in the x direction and two planes that are segmented in the y direction. An enlarged view of the delay-line PPAC is shown in Figure 3.8. A time-to-digital converter (TDC) is employed to measure the delay time, which starts with the anode signal (electron drift time) and stops with cathode signals. The fast induced signals in the cathode enter the delay line and travel to the left and right $i.e.$ the *X1* and *X2* cathode terminals, respectively. The delay time in the cathode terminals is represented as T_{x1} and T_{x2}, the position X_{Pos} of the ionizing particle is given by

$$X_{Pos} = K_x \times (\frac{T_{x1} - T_{x2}}{2} + X_{off}) \tag{3.9}$$

where K_{x} (mm/ns) and X_{off} (mm) are the position coefficient and the offset correction, respectively. The control sum is the sum of the total delay time which corresponds to the total delay line length.

$$T_{sumX} = T_{X1} + T_{X2} - 2T_a \tag{3.10}$$

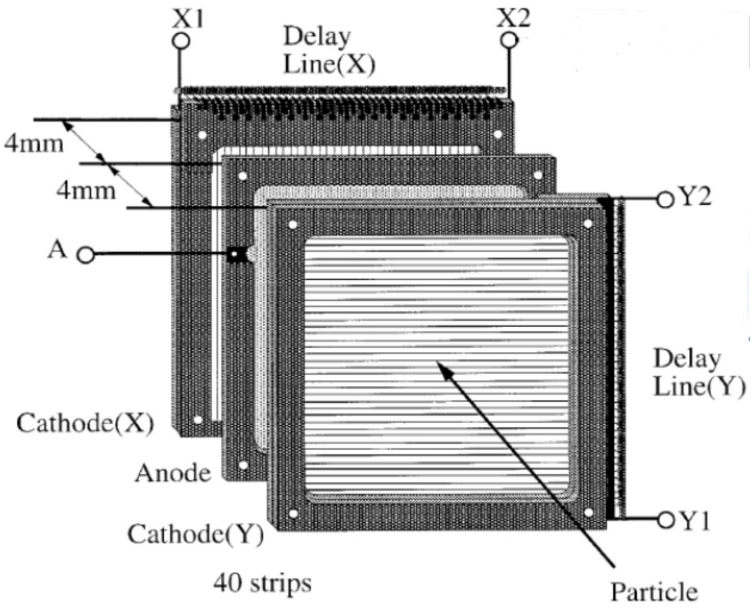

Figure 3.8: Schematic of a PPAC in BIGRIPS.

Similarly, T_{sumY} and Y_{Pos} are computed for the y position. The control sum is independent of the ionizing particle position, thereby having a constant value if the events are normal. However, if the avalanche region gets wider due to the creation of δ rays or multiple hits, it decreases the control sum as T_{X1} and T_{X2} gets smaller than the normal value [112].

3.8 Multiple-Sampling Ionization Chamber (MUSIC)

As discussed in the previous sections, two multiple-sampling ionization chambers (MUSIC) based on the design described in [114] are used to measure ΔE for determining the Z, counting both the incident particles and reaction products at F11. The MUSIC detectors are from the Fragment Separator (FRS) at GSI, Germany. The ionization chamber is segmented into eight anodes made of a thin mylar foil aluminized on each side, with an active length of 400 mm along the beam axis. The neighboring anodes are electrically connected in pairs. CF_4 is used as the ionization gas in both the MUSIC detectors operated at room temperature and atmospheric pressure.

A schematic view of the internal geometry is shown in Figure 3.9. Electron-ion pairs are created as the ionizing particle penetrates the ionization gas and loses energy. The number of e^-–ion pairs generated is proportional to the square of charge of the penetrating particle. The energy lost by a charged particle when interacting with a material is described by the Bethe-Bloch formula:

$$-\frac{dE}{ds} = \frac{4\pi Z_p^2}{m_e c^2 \beta^2}\left(\frac{e^2}{4\pi\varepsilon_0}\right)^2 Z_t N_t \left(\ln\frac{m_e v^2}{I} - \ln(1-\beta^2) - \beta^2\right) \tag{3.11}$$

where Z_p and β represent the charge and the velocity of the impinging particle, respectively and s represents the path length of the particle in the absorber material. I, N_t and Z_t are the mean excitation potential, particle density and the proton number of the absorber material, respectively. The charge and mass of the electron are e and

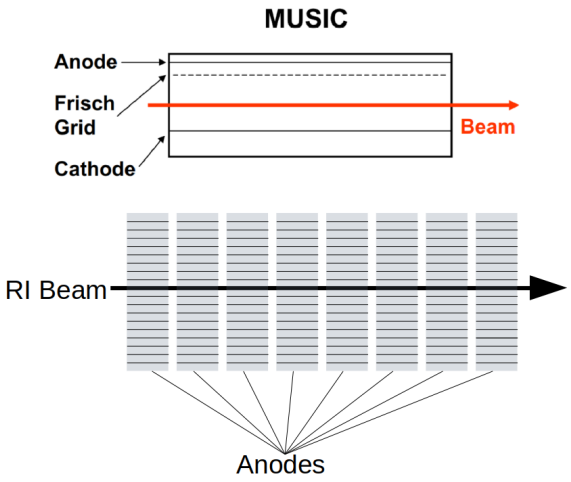

Figure 3.9: Schematic view of ions passing through the MUSIC detector.

m_e [115]. The electrical signal produced from the anodes is read-out using the charge-sensitive preamplifiers which convert the charge into a proportional signal amplitude. In order to obtain the charge information, the anodes were coupled to be equivalent to a single anode read out. The peak sensing ADC used in this experiment is made by Mesytec (MADC-32). It has a fast conversion time of 800 ns for 32 channels at 2k (2048) resolution as it is a 12-bit ADC [116].

3.9 Plastic Scintillators

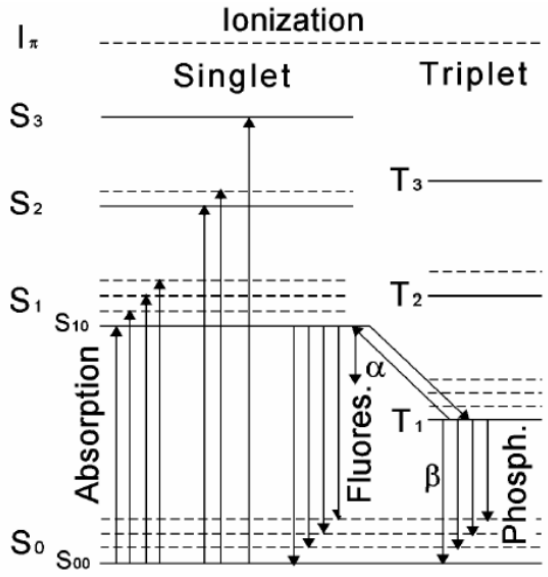

Figure 3.10: Energy levels of organic molecules.

The plastic scintillation counters were used to measure the time-of-flight (TOF) [117]. Organic scintillators (plastic) are characterized by a short decay time of around 2 ns and are suitable for fast timing purposes. The scintillation mechanism is quite different in organic materials as the scintillation arises because of the structure of the crystal lattice.

The fluorescence mechanism in organic materials arises from transitions in the energy level structure of a single molecule and can be observed independently of the physical state [118]. The scintillation light in organic scintillators is emitted in transitions between S_{10} and the ground state as the fluorescence emissions except ($S_{10} \rightarrow S_{00}$) have lower energy than the minimum required for absorption. The energy levels of organic molecules are shown in Figure 3.10. The plastic scintillator detectors, EJ-212 and EJ-230 from Eljen technology were used in the BigRIPS and ZDS setup. The properties of these plastic scintillators are shown in Table 3.2.

The secondary photons emitted via scintillation propagate to a Photo-Multiplier

Table 3.2: Time-of-flight measurements for determining the offset.

Scintillator	EJ-212	EJ-230
Light Output (% Anthracene)	65	64
Efficiency (photons//1 MeV e^-)	10000	9700
Rise Time (ns)	0.9	0.5
Decay Time (ns)	2.4	1.5
Pulse Width (ns)	2.7	1.3
Max. Wavelength (nm)	423	391
Density (g/cm^3)	1.023	1.023
Refractive Index	1.58	1.58

Tube (PMT). The PMTs are manufactured by Hamamatsu Company which include types H6533 and H2431. When a photon enters the PMT, it interacts with the photocathode and produces a photoelectron. The next stage consists of a series of dynodes each at a higher potential than the previous one, which the electron has to pass through. The electron releases additional electrons upon impacting a dynode and accelerates towards the next dynode. This avalanche of electrons eventually reaches the anode creating a signal which is fed to the processing unit. PMTs were connected to both ends of the plastic scintillator in the horizontal direction. The time difference between signals from the two PMTs contains the position information of the incident particle. The digital outputs of these units served to start and stop the time-to-digital converters (TDC). The average of the two timing signals from each side of the PMT is used as the final TOF to eliminate the time difference introduced due to different hitting positions of the incoming particles on the plastic scintillator.

Signals generated by the plastic scintillation detectors are split into two to provide both energy and time information. The energy loss measurement is fed to a Charge-to-Digital Converter (QDC). The other is delivered to a Leading Edge Discriminator (LED) with thresholds set above the noise level of PMTs. There is a time delay of 150 ns because of the long transmission distance between the experimental setup and the Data Acquisition (DAQ) system [119]. Therefore, a second LED is used after the long transmission for reshaping the timing signals. The LEDs, TDC and QDC used here

are LeCroy 623B, CAEN-V1290 and Philips 7166, respectively.

3.10 Veto Scintillators

The veto scintillator detector is used as a passive veto detector to remove the unwanted events while doing the data analysis. A Veto scintillator was placed in front of the carbon reaction target at F11. The central aperture of the veto scintillator is smaller than the reaction target area.

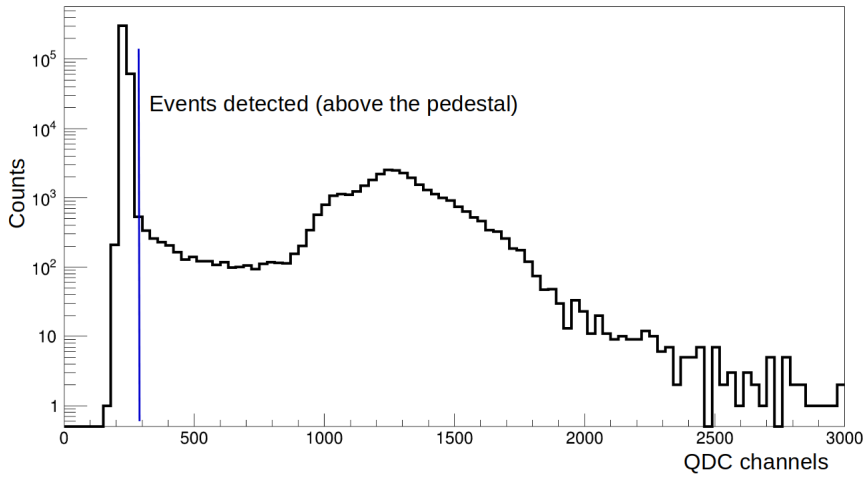

Figure 3.11: Energy deposited in the PMT (right) in scintillator.

Similar to the plastic scintillator, PMTs are attached to the left and right sides. The readout is obtained from the PMTs attached to these both sides. The RI beam near the edge of the reaction target should be rejected. PMT detects the signals corresponding to the events at the edge of the reaction target and the spurious events caused by nuclear reactions along the beamline upstream.

In the off-line data analysis, the signals detected in either PMTs were rejected from the incident beam selection for the isotope of interest. The QDC channels of the PMT (right) are shown in Figure 3.11 where the events above the pedestal correspond to the events detected by the PMTs. The correlation of left and right energy loss signals in the PMTs will be explained in Chapter 4.

3.11 Signal processing and data acquisition trigger system

As explained in the previous sections, electric charge carriers are produced when an incident charged particle interacts with the detector. To construct an electrical signal for further analysis the front end boards include pre-amplification, shaping, discrimination, and digitization.

The pre-amplification is the first stage of signal amplification from the detector. The preamplifiers are located close to the detector, which allows a reasonably long cable between the detector and the readout. The preamplifier circuit is designed to improve the signal strength for further amplification. A charge-sensitive preamplifier was used in this experiment. The amplified signal from the preamplifier circuit is sent into a shaping amplifier unit in order to optimize the signal-to-noise ratio (SNR) and for further amplification. The shaping amplifier unit applies a capacitor-resistor followed by resistor-capacitor CR-$(RC)^2$ networks to improve the SNR. The CR network eliminates the low-frequency signals and the RC network attenuates the high-frequency components, which contain a lot of noise.

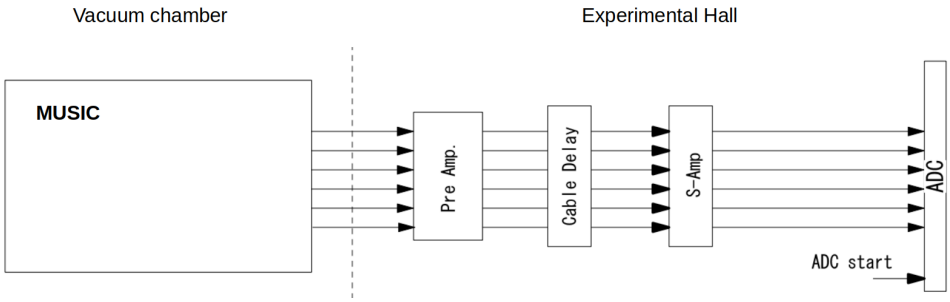

Figure 3.12: Pulse processing from the shaping amplifier for MUSIC [120].

The shaper output contains the information of the energy deposited in that detector. This analog signal from the shaper needs to be converted into something more useful: an equivalent digital signal. For example, the MUSIC detector's shaper output is read out using the Analog-to-Digital Converter (ADC). Peak-sensing ADC by

Mesytec (MADC32) was used in this experiment for the digitization of the signal from the MUSIC detector. The ADCs have a resolution of 13 bits, which has a range of 0 to 8191 channels. The MUSIC detector's circuit diagram is shown in Figure 3.12.

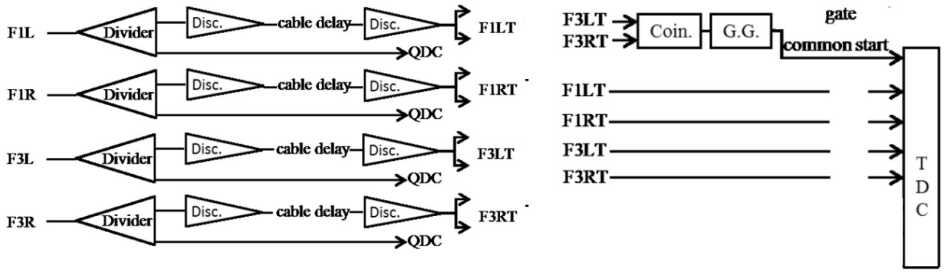

Figure 3.13: Pulse processing from the shaping amplifier for Plastic Scintillators [120].

A Leading Edge Discriminator (LED) was used in this experiment for eliminating the electronic noise generated by the PMTs as discussed in Section 3.9. The threshold is set to the desired voltage using a simple voltage comparator in the LED. The LED generates an output logic pulse when the amplitude pulse crosses the threshold voltage level. The pulse generated from the LED is digitized using a Time-to-Digitial Converter (TDC). The TDCs (model number CAEN V1190/V1290) employed in this experiment were 21-bit multi-hit TDC. The second signal from the plastic scintillator is fed to the Charge-to-Digital Converter (QDC-Philips 7166/H) as shown in Figure 3.13.

The signals from the detectors need to be transmitted to the Data Acquisition (DAQ) system, which is nearly 100 m from the experiment hall. The signal is transmitted using optical fiber cables. The optical fiber cables have a high-frequency range of 2.5 GHz because of the low attenuation of a few hundreds of meters long cables. The signal from the amplifier of a PPAC is fed to the Constant Fraction discriminator (CFD) as shown in Figure 3.14. The CFDs are used to yield trigger times independent from the peak heights, which eliminates the time walk effect. CFDs output is read out using the (CAEN-V1190/1290) TDCs, which assign the timestamps.

A particle traversing through different detectors (PPAC and Plastic) from F1 to

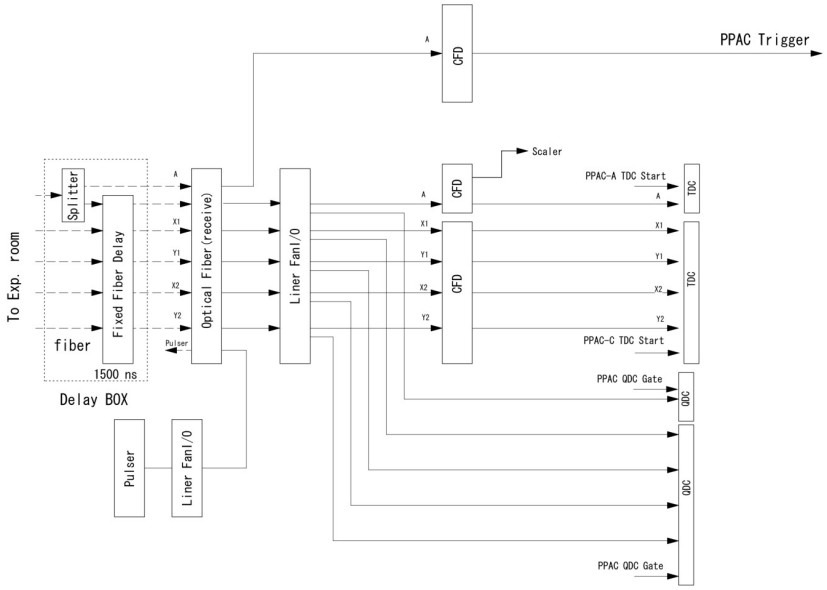

Figure 3.14: Pulse processing from the shaping amplifier for PPAC [120].

F7 (BigRIPS) and F8 to F11 (ZDS) should produce a signal at each of the focal plane detectors for it to be considered as an event. The trigger signals from the different detectors at different focal planes in the BigRIPS are fed to the "Trigger Box" as shown in Figure 3.15. The BigRIPS "Trigger Box" output in coincidence with the ZDS Trigger

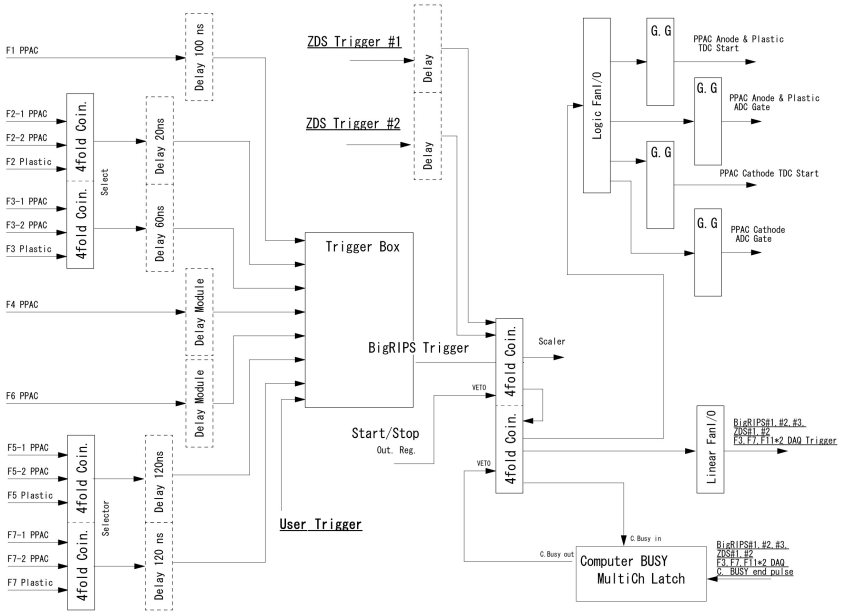

Figure 3.15: Trigger logic from the detectors in the BigRIPS and ZDS [120].

gives a valid master trigger for the event of interest. Therefore, this experiment is based on an event-by-event analysis. All the events are not registered by the DAQ because of the dead time involved to process an event. The master trigger is then fed to the Quad Gate Generator (G. G) unit via logic fan I/O to acquire the data in coincidence. The quad gate generates a gated pulse within the user-defined time window. The output signals from all the detectors used in this experiment were processed by NIM modules. The signals processed were digitized by CAMAC and VME modules.

Chapter 4

Data Analysis

This chapter provides an overview of the techniques employed to extract the physical observables of interest from the detectors. The raw data collected from the detectors are in a digitized form, for example in ADC, TDC and TAC. Performing detector calibration of these TDCs and ADCs, we can convert the digital signal into a physical quantity like time, charge and energy. In the first few sections, calibration procedures of all the detectors are discussed. Once the detectors are calibrated, the data analysis is divided into two parts, particle identification (PID) before the reaction target for the incident beam selection and the identification of the charge-changing events after the reaction target; which is required for the determination of σ_{cc}. The phase space restriction on the incident beam particles is discussed in detail in this chapter. Finally, the measurement of charge-changing cross-section is discussed.

4.1 Proton number identification

The proton number of the particles was determined using the MUSIC detectors. The calibration of MUSIC detectors was done to associate the energy loss in channels with Z of the particles. As discussed in Section 3.8, the energy loss in a detector is proportional to the square of charge of the incident particle which can be understood from

the equation of the stopping power (dE/dx), which is defined as energy loss per unit length given as:

$$-\frac{dE}{dx} \propto \frac{Z^2}{\beta^2} \tag{4.1}$$

where Z and β are the atomic number and the velocity of the incident particle, respectively.

MUSIC detectors placed upstream (MUSIC1) and downstream (MUSIC2) of the target were used for identifying the atomic number of the beam particles. The charged particle deposits energy as it passes through the detector material; which generates a voltage pulse. This voltage pulse is digitized in the form of a channel number using a peak sensing ADC. Calibration is the conversion of channel number into a more useful form of physical quantity i.e. energy for this case.

The MUSIC detector consists of 8 anodes, which are gain matched by aligning the channel number of all the anodes. All the anodes are aligned by multiplying a factor g that equates with the peak position (channel) of the central anode given by Equation 4.2. The peak position of the channel number of the incident particle is found using a Gaussian fit for the central anode which corresponds to the energy lost by the nuclide of interest ($^{20,\,22}$C). The following linear equation is employed for the gain matching of all the anodes of the MUSIC detector:

$$E_c = (C - P) \times g \tag{4.2}$$

where *C* represents the channel numbers from the ADC, pedestal *P* is the zero-energy point in the ADC spectrum, and *g* is the factor used for gain matching of the anodes.

The geometric mean of all the gain matched anodes (*dE*) is determined for the conversion of the ADC channel number to a physical quantity $i.e.$ *Z*. The stopping power is related to Z^2, given by Equation 4.1. Calibration of the MUSIC detectors is

done using:

$$Z^2 = f \times C \tag{4.3}$$

where f is the calibration factor for converting the channel number into the energy deposited in the detector. The MUSIC1's uncalibrated (ADC channels) and calibrated

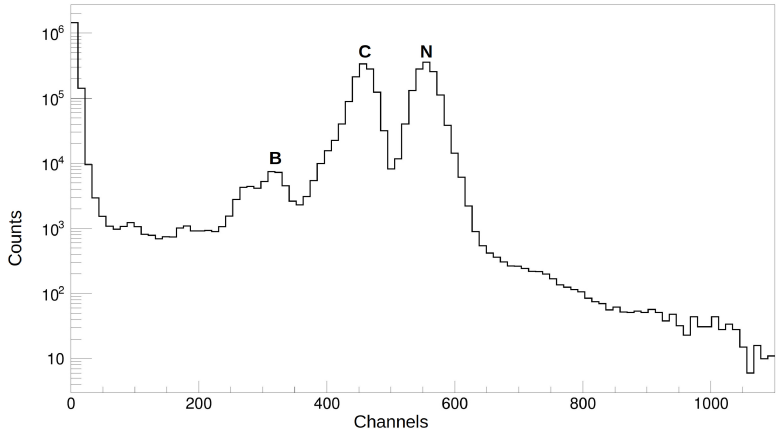

(a)

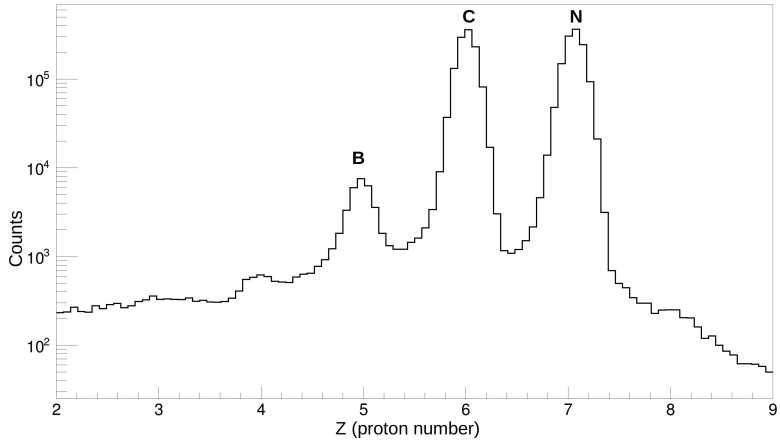

(b)

Figure 4.1: (a) The uncalibrated MUSIC (channels) spectrum. (b) The calibrated MUSIC (Z) spectrum.

spectra (Z) for ^{22}C secondary beam are shown in Figure 4.1 (a) and (b), respectively. The Z resolution of MUSIC1 and MUSIC2 in terms of σ was ΔZ = 0.09 for carbon isotopes.

4.2 Position determination

As discussed in Chapter 3 the vertical and horizontal positions of the ionizing particle are computed by using the time difference between the induced signals on the left and right side of delay lines. When a side of the PPAC registers an event ("hit"), this hit information is used to determine the incident beams x- and y- positions at different focal planes of the experimental setup, which will allow the reconstruction of ion trajectories as described in Section 3.7. Track reconstruction is traditionally divided into two parts, the former being the track finding and the latter being the track fitting. Track finding enables the formation of subsets of hit information originating from the same particle. Using the information from the subsets, a set of track parameters is optimally estimated from the hit information. The track fitting is performed using the

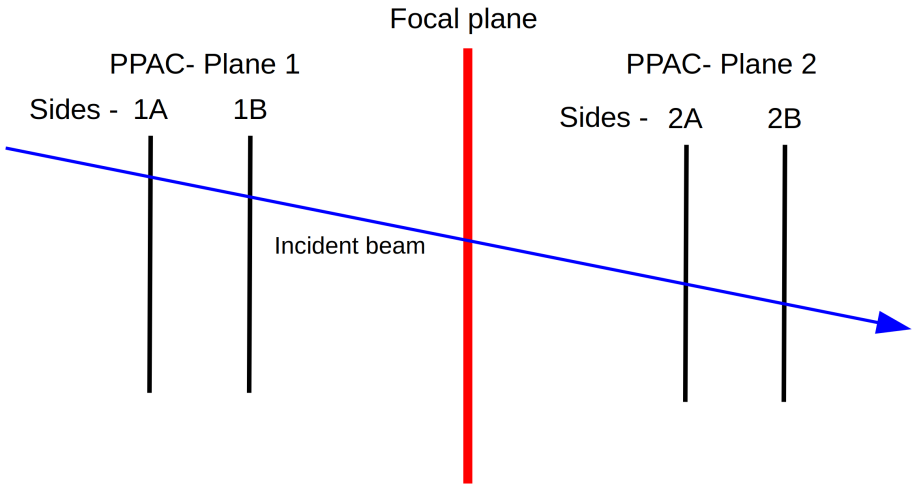

Figure 4.2: Schematic of two PPACs and their planes at the experimental focal plane.

least square minimization technique. The deviations (D^2) found from the least square minimization technique are added up on an event-by-event basis ($\sum$) as described in the equation:

$$D^2 = \sum [y_i - mx_i + c]^2. \tag{4.4}$$

where subscript i represents the side of the PPAC plane shown in Figure 4.2. These deviations (D^2) are minimized between the model ($c + m \times x_i$) and the data (y_i) using the least square principles to determine the trajectories at the focal planes. The trajectory reconstruction was made using the position and angles of the fragments measured using PPACs. First-order ion-optical transfer matrices attained from RI beams experimentally were used to reconstruct the trajectory. The central trajectory's $B\rho$ value was determined by the magnetic fields of the dipole measured by Nuclear Magnetic Resonance (NMR) probes. Determination of $B\rho$ with high resolution plays a pivotal role to attain a higher resolving power in particle identification of projectile fragments [121, 122] which will be explained in detail in Section 4.4. The x and y co-

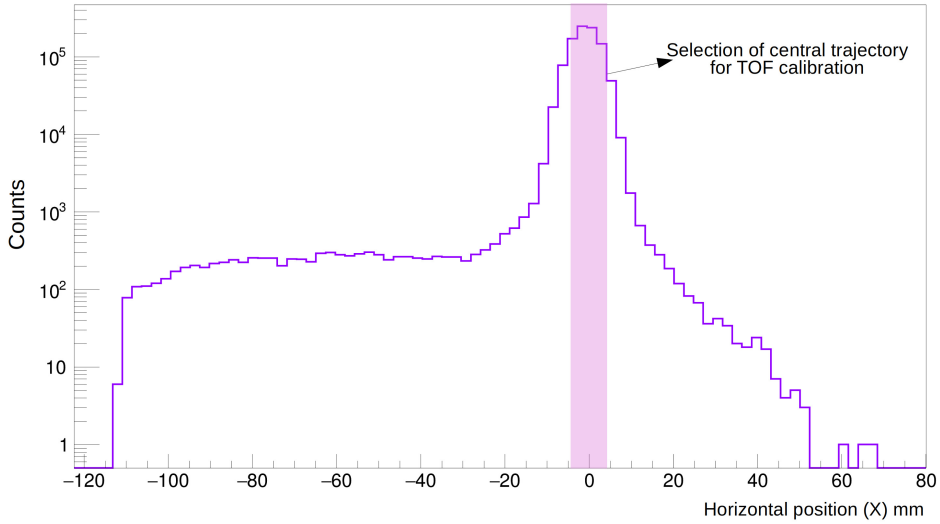

Figure 4.3: The horizontal position of the incident particle at the dispersive focal plane (F5). The central trajectory selected for Time-of-flight (TOF) calibration is shown by the transparent region.

ordinates in mm were determined using Equation 4.4. Figure 4.3 shows the x position at the dispersive focal plane (F5). The central trajectory from the momentum phase space is selected for measuring the time-of-flight which is explained in the following section.

4.3 Time of flight measurement

As mentioned previously in Section 3.9, the time-of-flight of the RI beams are measured using the plastic scintillators kept at different focal planes (F3, F5, F7, F8, F11). The measured TOF is the difference in timing information between plastic scintillators at respective focal planes as follows,

$$TOF = T_j^{PL} - T_i^{PL} \tag{4.5}$$

The subscripts i and j represent upstream and downstream information, respectively. On the other hand, TOF is represented as:

$$TOF = \frac{L}{\beta c} \tag{4.6}$$

where L is the flight path between the plastic scintillators (PS), β is the relativistic velocity and c is the speed of light. The flight path between plastic scintillators at focal plane F7 and F3 ($PS_7 - PS_3$) is 46.978 m. The flight path for the plastic scintillators in ZDS is ($PS_{11} - PS_8$) 36.983 m. Therefore, β is given as:

$$\beta = \frac{L}{TOF \times c} \tag{4.7}$$

The plastic scintillator has left and right PMTs at both ends as previously mentioned in Chapter 3. The average of the two timing signals from each side of the PMT is used as the final TOF given by Equation 4.8 to eliminate the time difference introduced due to different hitting positions of the incoming particles on the plastic scintillator

$$PL = \frac{PL_{TL} + PL_{TR}}{2} \tag{4.8}$$

where PL is the average of the left (PL_{TL}) and right (PL_{TR}) timing signals of the PMTs shown in Figure 4.4. The theoretical TOF for the isotopes of interest (^{20,22}C) is calculated using the magnetic field.

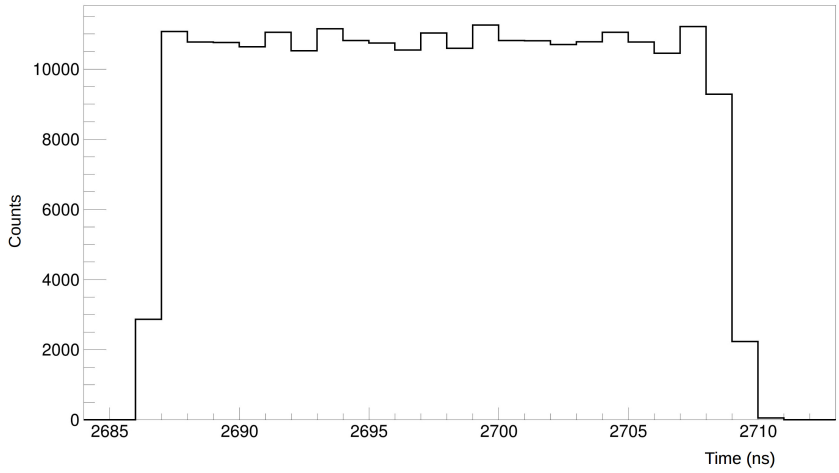

Figure 4.4: Timing signal (average) PL from plastic at F7.

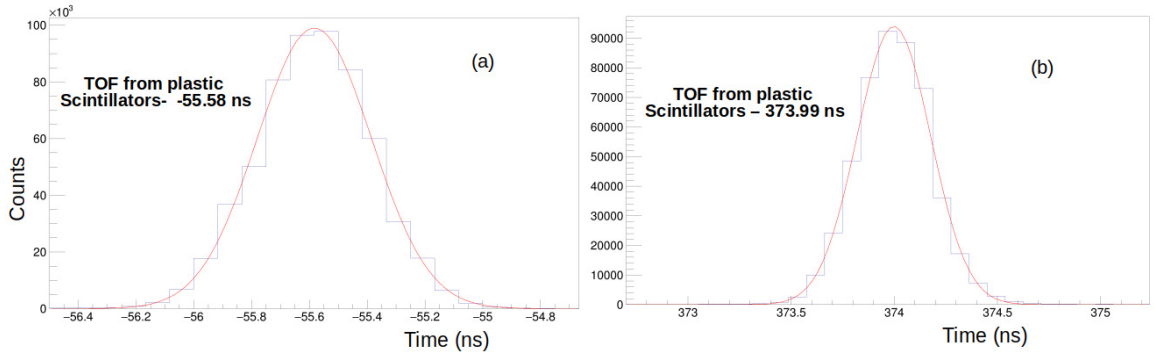

Figure 4.5: Measured TOFs (ns) for the flight path between downstream and upstream plastic detectors (a) $PS_7 - PS_3$ (b) $PS_{11} - PS_8$. TOF is determined by selecting the central trajectory of the isotope of interest ^{20}C.

The difference between the theoretical and the measured TOF gives the offset to be added to the measured TOF. The measured TOF is determined after selecting a central region of the incident beam's x position at F5 (dispersive focal plane) shown in Figure 4.5. The absolute TOF with the added offset to the measured TOF is shown in Figure 4.6.

The TOF offsets for PS_{11} and PS_8 scintillator detectors were also determined using

the procedure mentioned above. Table 4.1 shows the absolute TOFs, measured TOFs from the plastic detectors and the offsets. The plastic detector at F8 was removed for the ^{48}Ca data and the TOF offset was determined using PS_7 instead of PS_8.

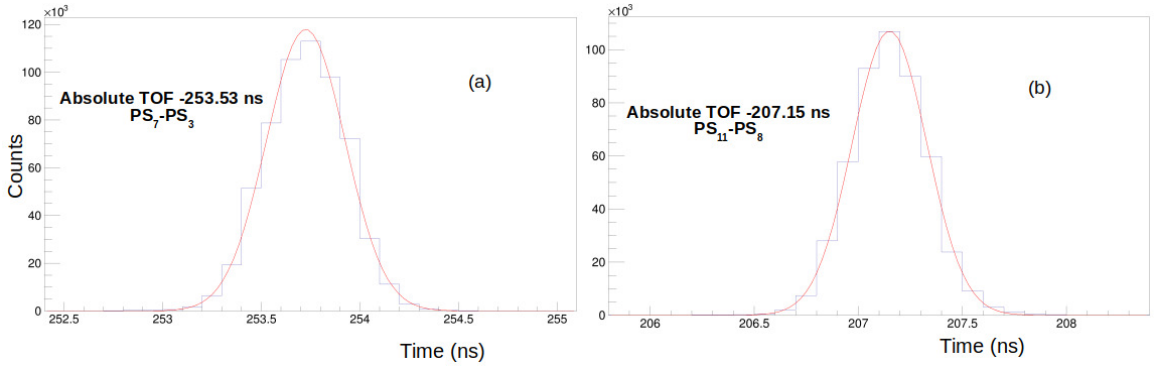

Figure 4.6: Absolute TOF (ns) for the flight path (a) TOF_{37} (b) TOF_{811}, of ^{20}C.

Table 4.1: Time-of-flight measurements for the offset determination

Isotope	Flight Path	Length (m)	Abs. TOF (ns)	Measured TOF (ns)	offset (ns)
^{48}Ca	$PS_7 - PS_3$	46.978	231.575	-77.750	309.325
^{22}C	$PS_7 - PS_3$	46.978	261.300	-47.820	309.120
^{20}C	$PS_7 - PS_3$	46.978	253.531	-55.58	309.111
^{48}Ca	$PS_{11} - PS_7$	47.146	248.9	334.2	-85.3
^{22}C	$PS_{11} - PS_8$	36.983	214.050	381.120	-167.070
^{20}C	$PS_{11} - PS_8$	36.983	207.150	373.99	-166.840

4.4 Particle Identification

Various secondary beam fragments arrive at the reaction target at F11. Therefore, the identification of a particular nucleus by its mass and charge number is crucial for the determination of σ_{cc}. The measurement of the energy deposited in the MUSIC provides the Z of the nuclei, as they are fully ionized heavy ions. The mass number is determined from the mass-to-charge ratio described by the motion of RI beams in the magnetic field.

Double PPAC detectors are installed along the beamline to determine the position of the incident particles, which is required for the trajectory reconstruction. The ab-

solute $B\rho$ values for the central trajectory from NMR probes were used as explained in the previous Section 4.2. The fractional momentum deviation (δ) relative to the central trajectory (p_0) is given by:

$$\delta = \frac{p - p_0}{p_0} = \frac{B\rho - B\rho_0}{B\rho_0} \quad (q = q_0) \tag{4.9}$$

Now, the dispersion matching of two stages requires that the deviation in the horizontal (x) position, because of the first stage (F3–F5), is compensated by the (F5–F7) dispersion ($x|\delta$) of the second stage as explained in Section 3.4. Fractional momentum deviation δ can be derived with the first-order ion optical transfer matrix M by the following equation:

$$\begin{bmatrix} X_j \\ A_j \\ \delta_{ij} \end{bmatrix} = \begin{bmatrix} (x|x) & (x|a) & (x|\delta) \\ (a|x) & (a|a) & (a|\delta) \\ (\delta|x) & (\delta|a) & (s|\delta) \end{bmatrix} \begin{bmatrix} X_i \\ A_i \\ \delta_{ij} \end{bmatrix} \tag{4.10}$$

where *x* and *a* are the position and angle in the horizontal (x) direction and s is the distance along the central trajectory. The subscripts *i* and *j* denote the upstream and downstream focal plane information, respectively. The complete derivation of optical transfer Matrix M can be found in Ref. [123]. From Equation 4.10, δ_{ij} is derived for all the particles

$$\delta_{57} = \frac{1}{(x|\delta)_{57}}[X_7 - (x|x)X_5] \tag{4.11}$$

The horizontal position (x) of the particle is independent of the initial angle in a system with point-to-point imaging, hence the matrix element ($x|a$) is zero. Equation 4.9 can be re-arranged to obtain the magnetic rigidity:

$$B\rho = (1 + \delta_{57})B\rho_0 \tag{4.12}$$

The energy loss in the PPAC, plastic detectors and the energy degrader at F5 is taken

into account by a twofold $B\rho$ measurement in combination with the TOF measurement between the plastics (F7–F3) to determine the A/Q value of the fragments which is given by

$$TOF = \frac{L_{35}}{\beta_{35}c} + \frac{L_{57}}{\beta_{57}c}$$

$$\left(\frac{A}{Q}\right)_{35} = \frac{B\rho_{35}c}{\beta_{35}\gamma_{35}m_u} \tag{4.13}$$

$$\left(\frac{A}{Q}\right)_{57} = \frac{B\rho_{57}c}{\beta_{57}\gamma_{57}m_u}$$

where 35 and 57 subscripts denote the entities related to the F3–F5 and F5–F7 sections, respectively. If there is no change in A/Q ($Q \sim Z$, as the ions are fully stripped) in Equation 4.13, then:

$$\frac{\beta_{35}\gamma_{35}}{\beta_{57}\gamma_{57}} = \frac{B\rho_{35}}{B\rho_{57}} \ . \tag{4.14}$$

Using the measured TOF and magnetic rigidities ($B\rho_{35}$, $B\rho_{57}$), the fragment velocities before (β_{35}) and after (β_{57}) the wedge degrader at the dispersive focal plane (F5) can be deduced using Equation 4.14. The absolute A/Z value is determined using the combination of Equations 4.11 - 4.14:

$$\frac{m_0}{q} \approx \frac{A}{Z} = \frac{B\rho_0}{u\beta\gamma c}(1 + \delta_{57}) \tag{4.15}$$

The absolute Z value derived from the energy loss in the MUSIC detector is essential for the identification of the particles. Therefore, with the absolute values of *Z* and *A/Z*, PID can be achieved as shown in Figure 4.7. A similar technique is used to achieve PID (Figure 4.8) at the final focal plane position using the track information from double PPAC detectors installed at F9 and F11. The $B\rho$ value of the fragments on the central trajectory was determined using the same method applied for BigRIPS by measuring the magnetic fields of the dipoles by NMR probes. The dispersion matching sections are F7–F9 and F9–F11 in the Zero Degree Spectrometer (ZDS). The A/Z at F11 was

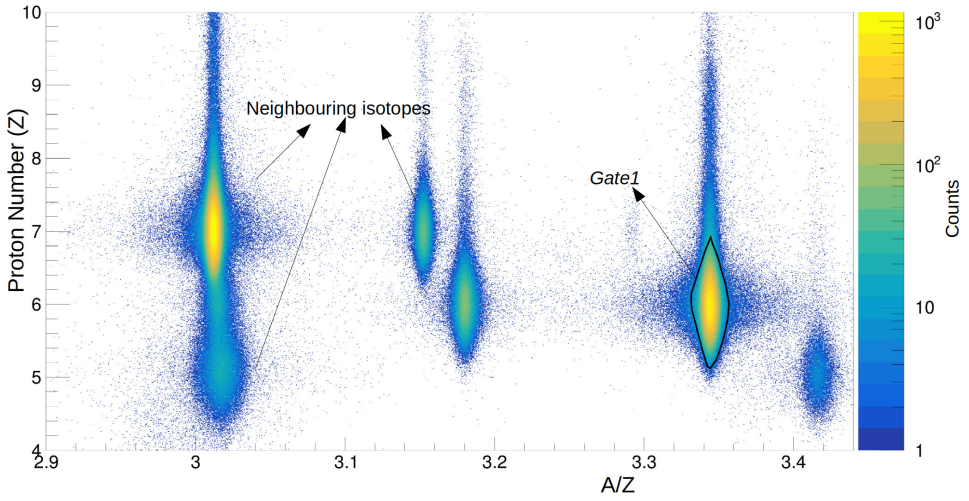

Figure 4.7: Particle identification plot for ^{20}C fragments from a ^{48}Ca primary beam in BigRIPS at F7.

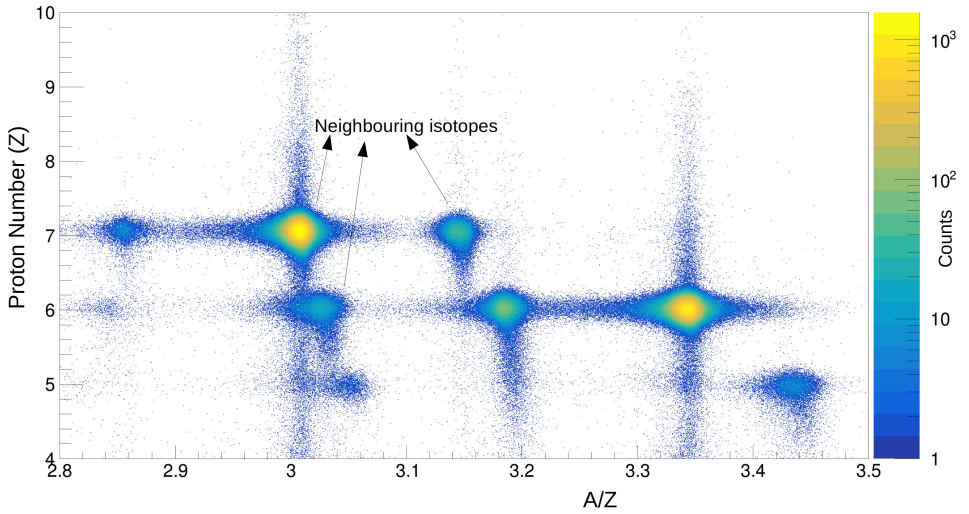

Figure 4.8: A two-dimensional plot for ^{20}C fragments from a ^{48}Ca primary beam in ZDS at F11.

determined using the same technique explained for A/Z at F7:

$$\frac{A}{Z} = \frac{B\rho_0}{u\beta\gamma c}(1 + \delta_{911}) \tag{4.16}$$

The neighboring isotopes are clearly visible for the ^{20}C secondary beam as shown in Figure 4.8. The incident beam is selected after inspecting the position and angular correlations of the secondary beam upstream which will be discussed in detail in Section 4.7. The correlation plot in Figure 4.9 shows the energy loss signal of the left

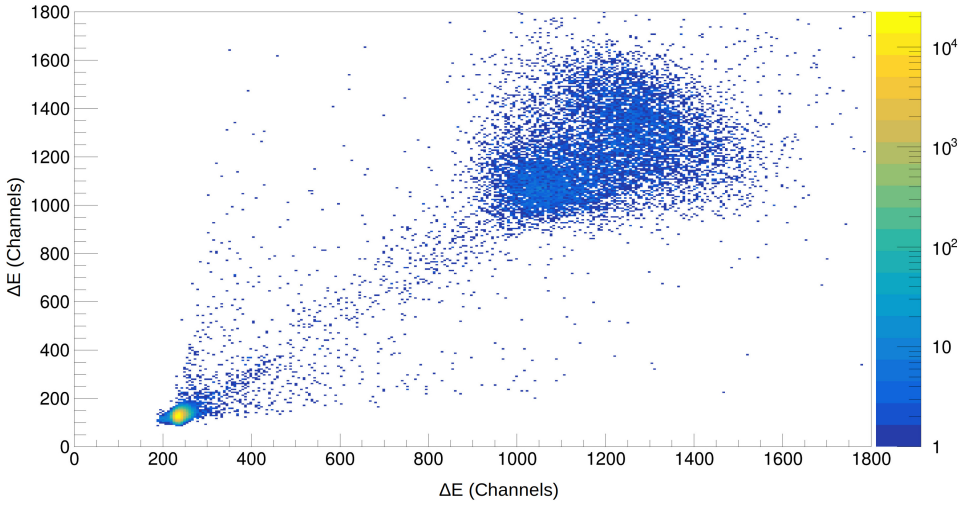

Figure 4.9: Correlation plot of the amplitudes of Veto_L and Veto_R for the ^{20}C secondary beam.

PMT (Veto_L) compared to the energy loss signal of the right PMT (Veto_R) for ^{20}C. As explained in Section 3.10, the signals detected above the pedestal in the energy loss signal of either ends of the veto scintillator detector. The contamination level is 0.03% in the PID at F11 target for the carbon isotopes. Therefore, these signals are rejected in the analysis.

4.5 Incident beam selection

As discussed in the previous chapter, σ_{cc} is determined using the transmission ratios with and without the target, R_{Tin} and R_{Tout}, respectively:

$$\sigma_{cc} = \frac{1}{t} \ln \frac{R_{Tout}}{R_{Tin}} \tag{4.17}$$

To determine the transmission ratios (R_{Tin} and R_{Tout}), ^{20}C is selected from the PID plot at BigRIPS (F7) which shows the graphical selection of events $(gate1)$ as shown in Figure 4.7. The selection of event $gates$ shown in this section are the final gates used for selecting the incident beam before the target. The $gate$ selection is made after iteratively going through different parts of the correlations to understand the

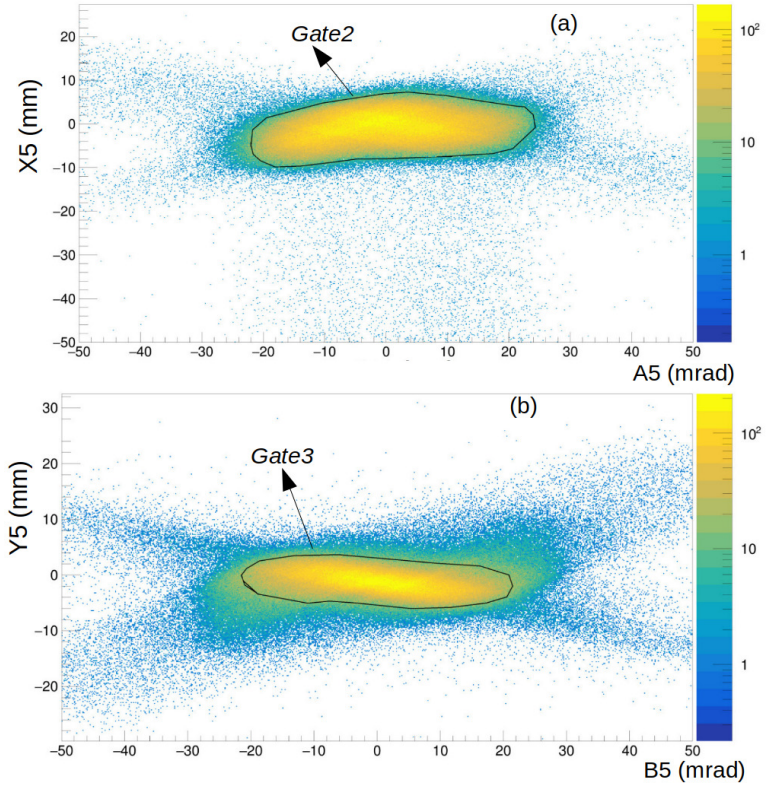

Figure 4.10: (a) Position and angle correlation (x, a) at F5 with *gate1*. Graphical selection of events is shown by *gate2*. (b) Angle and position correlation (y, b) at F5 with *gate1* and *gate2*. Graphical selection of events is shown by *gate3*.

spurious and background events The position and angle correlation are used to make a selection on the momentum phase space at the dispersive focal plane F5 as shown in Figure 4.10, where (a) shows the graphical selection of events (*gate2*) made for the horizontal position (x) and angle (a) correlation with *gate1* and (b) shows the graphical selection of events (*gate3*) made for the correlation between the vertical position (y) and angle (b) with *gate1* and *gate2*. The phase space restrictions defined with *gate1* - *gate3* are used to select events for inspecting the position and angular correlation further downstream. A similar procedure is followed for the focal plane (F7) and new gates (*gate4*, *gate5*) are implemented as shown in Figure 4.11. The particle identification plot is shown in Figure 4.12 with the PID selection in BigRIPS (*gate1*) and with the event selection made at focal planes *F5 (gate2, gate3)* and *F7 (gate4, gate5)*. The

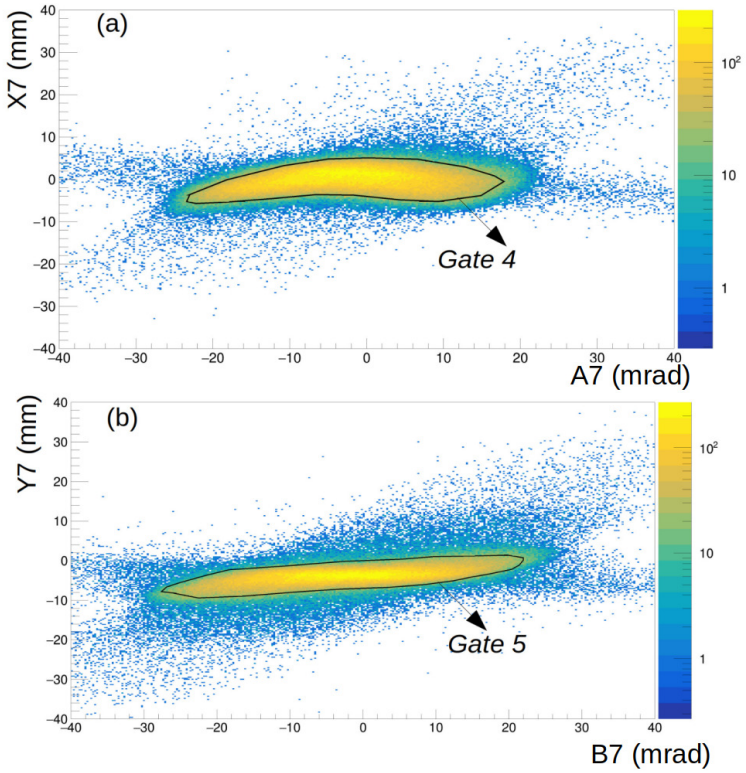

Figure 4.11: (a) Angle and position correlation (x, a) at F7 (*gate4*) with *gate1* - *gate3* (b) Angle and position correlation (y, b) at F7 (*gate5*) with *gate1* - *gate4*

.

background events are clearly visible in the PID spectrum in Figure 4.12.

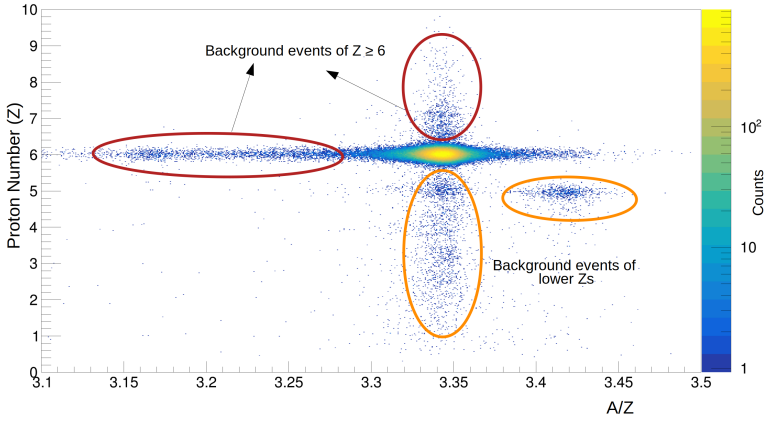

Figure 4.12: Particle identification in ZDS at F11 with *gate1* - *gate5*. Proton number is derived from the MUSIC1 at F11. The background events in the PID spectrum are shown by arrows.

The background events of lower Zs shown in Figure 4.12 can be further inspected by the correlation between the vertical position (y) of ^{20}C at the reaction target (F11)

and the proton number derived from the MUSIC detector. The condition in this correlation plot (*gate6*) is set such that the events below the channel number 390 in ADC are rejected during the analysis as shown in Figure 4.13. After the rejection of reac-

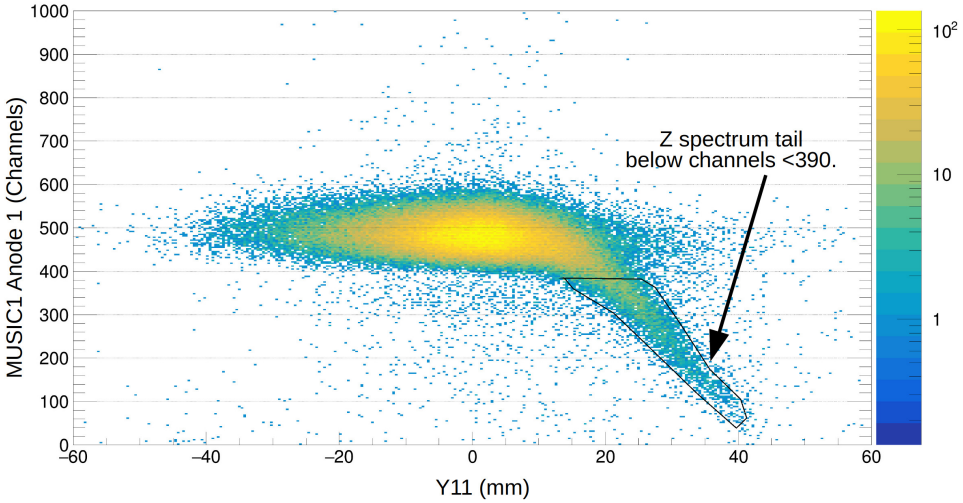

Figure 4.13: Correlation plot between vertical position (y) at F11 target and the energy loss in the first anode (ΔE).

tion events arising from the MUSIC detector, the purified PID spectrum with all the previous selection conditions applied (*gate1* - *gate6*) is shown in Figure 4.14. The puri-

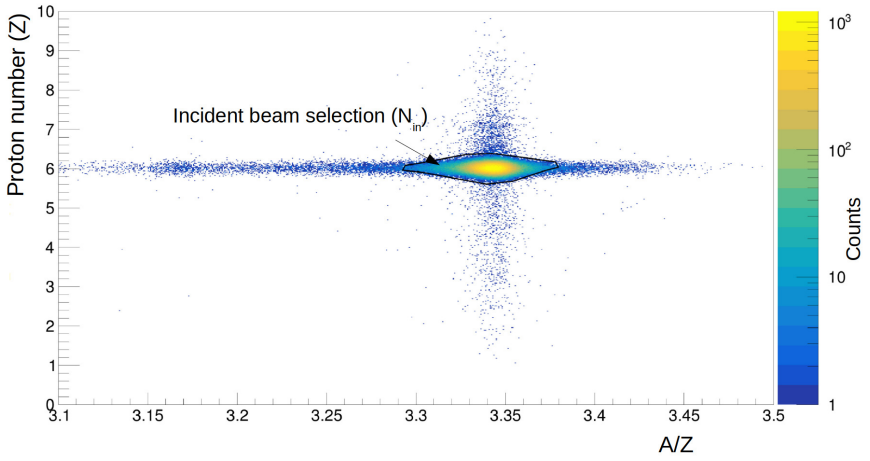

Figure 4.14: The incident beam selection of ^{20}C from the particle-identification plot.

fied PID spectrum after rejecting the secondary reactions from the MUSIC detector is shown in Figure 4.14 with all the previous selection conditions ($gate1 - gate6$) applied.

Now, the incident beam events (N_{in}) of ^{20}C are selected before the reaction target as shown in Figure 4.14. The process of contamination removal and the selection of incident beam events were followed for each of the BigRIPS and ZDS settings (^{22}C and ^{48}Ca).

4.5.1 Primary Beam analysis (^{48}Ca)

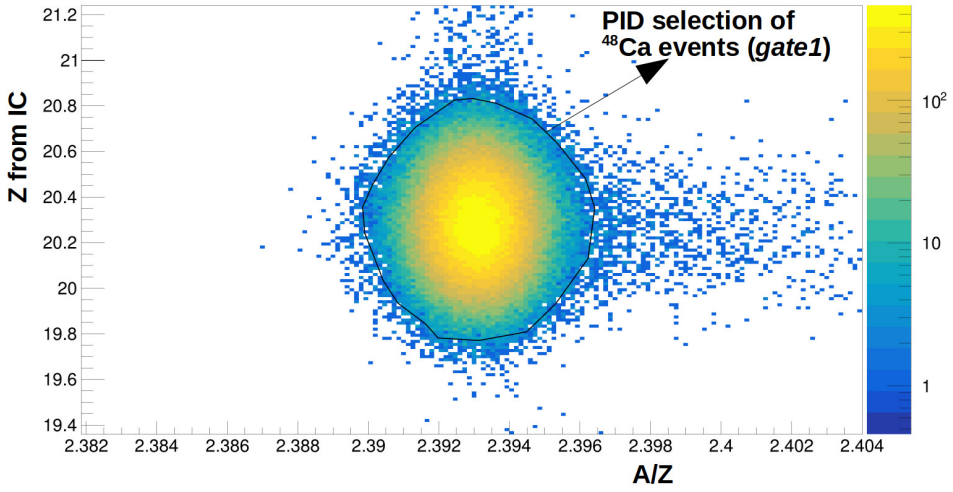

Figure 4.15: Particle identification plot for ^{48}Ca primary beam in BigRIPS at F7.

A similar analysis was done for the primary beam (^{48}Ca). The particle identification plot for the primary beam at F7 (BigRIPS) is shown in Figure 4.15 with the selected events of ^{48}Ca. The selected events of ^{48}Ca using the PID at F7 (*gate1*) are used to make a graphical selection of events on the phase spaces at different focal planes. The selection for the primary beam's phase space is more stringent compared to the RIBs because of electronic artifacts arising from the PPACs as shown in Figure 4.16 for one of the position and angular correlations at F3 (X_{F3} : A_{F3}). The phase space of the incident beam was investigated by making a selection of events using the position and angle correlation (X_{F3} : A_{F3}, Y_{F3} : B_{F3}, X_{F5} : A_{F5}, Y_{F5} : B_{F5}). The cluster of low events separated from the main events of interest in these correlations was inspected further downstream. Figure 4.16 shows one of the event selection made

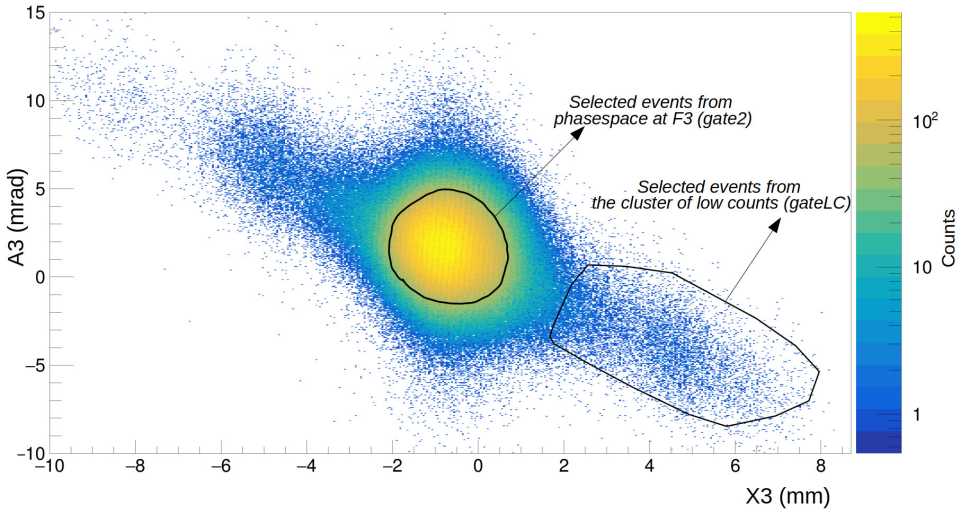

Figure 4.16: Position and angular correlation at F3 with the restricted phase space defined using the PID selection of ^{48}Ca. Selection made from the cluster of low counts is shown.

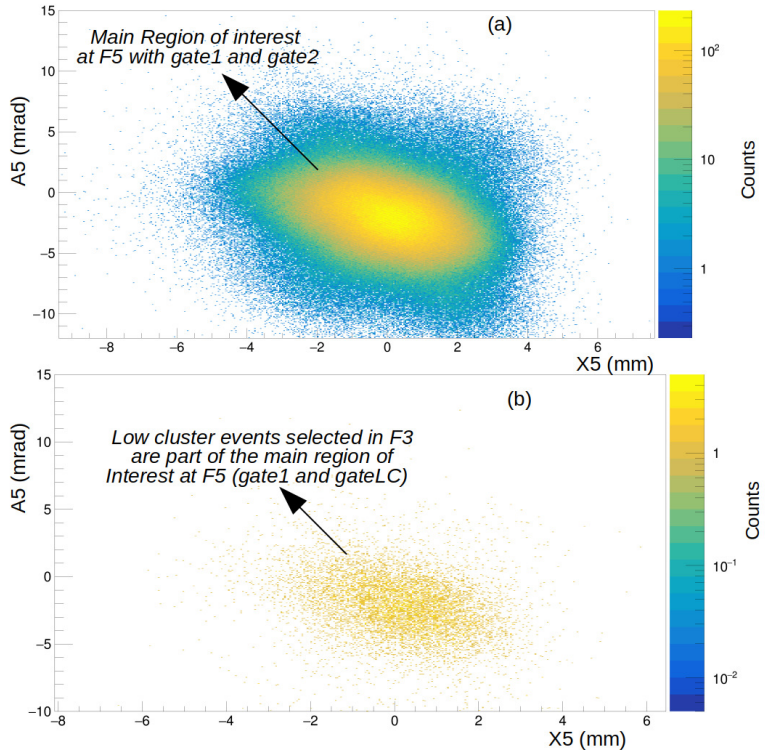

Figure 4.17: (a) Position and angular correlation (X, A) at F5 with the events selected ($gate1$ and $gate2$). (b) Same correlation with the events selected ($gate1$ and $gateLC$).

for this inspection using the correlation at F3 ($X_{F3} : B_{F3}$). The selected events from the cluster of low count events are part of the central trajectory of ^{48}Ca as it reaches

further downstream at F5, F7 as shown in Figures (4.17 (b) and 4.18 (b)).

This demonstrates that these events with larger positions and angles in F3 originate due to some electronic signal reflections in the F3 PPAC. For ensuring a safe selection of proper events, these events are eliminated in the selection of the incident beam before the target.

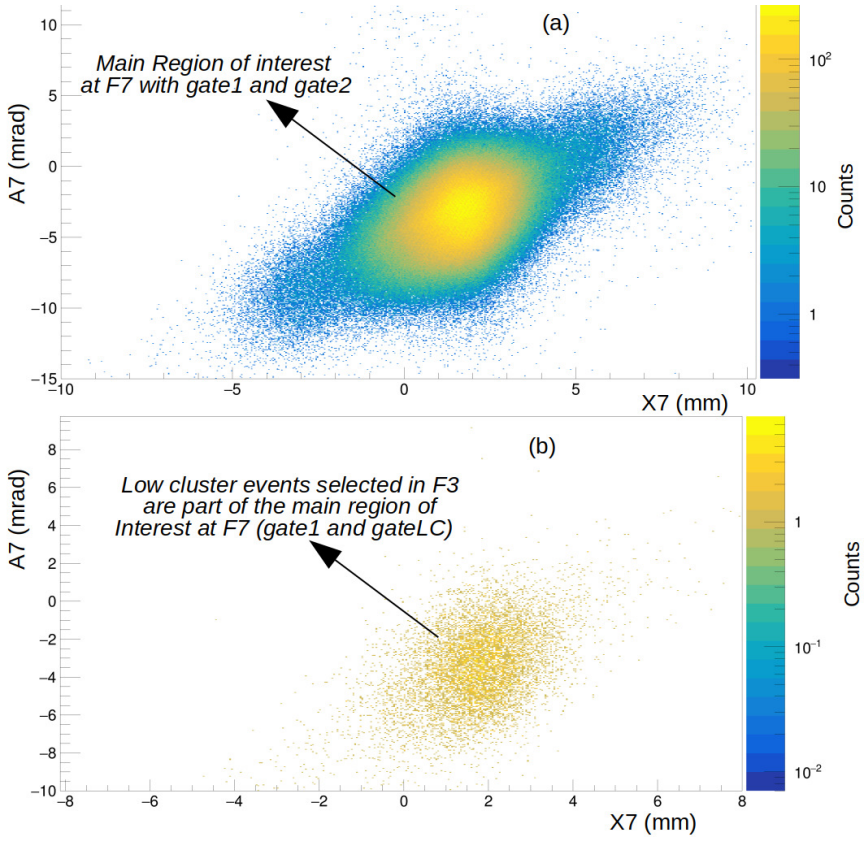

Figure 4.18: (a) Position and angular correlation (X, A) at F7 with the events selected ($gate1$ and $gate2$). (b) Same correlation with the events selected ($gate1$ and $gateLC$) demostrating the electronic artifact arising from the PPACs.

Figure 4.17 (a) and 4.18 (a) show the angular and position correlation (X, A) at F5 and F7 with the selection of events ($gate1$, $gate2$) made using the PID information at F7 (4.15) and the correlation at F3 (4.16). Part (b) of these Figures (4.17, 4.18) show the same correlations with the selection of events ($gate1$, $gateLC$). The same procedure was followed for eliminating these artifacts from (X, A) and (Y, B) correlations at different focal planes.

A similar procedure was followed for the contamination removal of the ^{48}Ca at different phase spaces as explained in the previous section for ^{20}C. The incident beam events (N_{in}) of ^{48}Ca are selected with all of the phase space conditions applied at different focal planes as shown in Figure 4.19. Due to the lower efficiency of PPACs for the ^{48}Ca data, the TOF_{811} was used for the PID of the primary beam instead of *A/Z*.

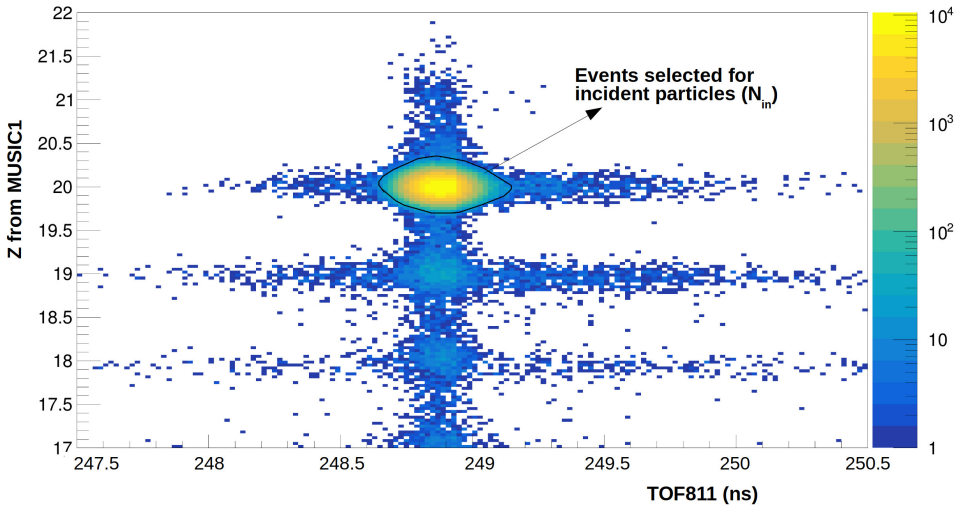

Figure 4.19: The incident beam selection of ^{48}Ca from the particle identification at F11.

4.6 Z identification after the reaction target

To determine the σ_{cc}, the particles with unchanged charge (Z) after the reaction target need to be identified and counted (N_{sameZ}). The offline analysis of target-out measurements was performed with the same condition as the target-in data.

4.6.1 Z identification for ^{20}C data

Figure 4.20 shows the MUSIC2 energy loss spectrum with the incident beam selection, phase space conditions (*gate1-gate6*) described in Section 4.5 and phase space restrictions which will be explained in the next Section 4.7. The red histogram represents the proton number spectrum for the target-in measurements and the blue histogram

Figure 4.20: Z obtained from MUSIC2 spectrum with the target (red) and without the target (blue) for ^{20}C.

represents the target-out measurements, where the target-out spectrum is normalized to the target-in spectrum using the histogram counts. The charge-changing cross section is based on the transmission technique. The transmission ratio (R_T) is given by:

$$R_T = \frac{N_{out \geq Z}}{N_{in}} \tag{4.18}$$

where R_T represents the transmission ratio which is determined from the ratio of proton uninteracted nuclei $N_{out \geq Z}$ and the incident particles N_{in}. The $N_{out \geq Z}$ are the particles with the proton number greater than or equal to the selected events of the incident beam N_{in} which is $Z = 6$ in this case as shown in Figure 4.14.

The spectrum shows three different particles, boron ($Z = 5$), carbon ($Z = 6$) and nitrogen ($Z = 7$). $Z = 5$ is a result of incident carbon beam losing a proton, whereas the $Z = 7$ is produced by picking up a proton from the reaction target. The production of the nitrogen isotope with $Z = 7$ originates from the charge exchange where one proton is added to the incident nucleus ^{22}C. These reactions do not involve the interactions with the protons of the incident carbon isotope. Therefore, the total number of counts under $Z = 6$ and $Z = 7$ peaks are subtracted in order to measure the

charge-changing cross-section as explained in Section 3.5. The vertical line in Figure 4.20 shows the 3.5σ region around the mean position of $Z = 6$ peak determined from the fits are explained in Section 4.6.4. The 3.5σ region around the mean in the Gaussian function covers 99.95% of the area under the peak.

4.6.2 Z identification for ^{22}C data

The steps explained in Section 4.5 are followed to obtain the phase space and the PID conditions for the 2-n halo nucleus ^{22}C. The proton number obtained from the MUSIC2 for ^{22}C is shown in Figure 4.21 with the 3.5σ region selection. The total number of counts under $Z = 6$ and $Z = 7$ peaks are counted to get the $N_{out \geq Z}$, which will be used to determine the σ_{cc}.

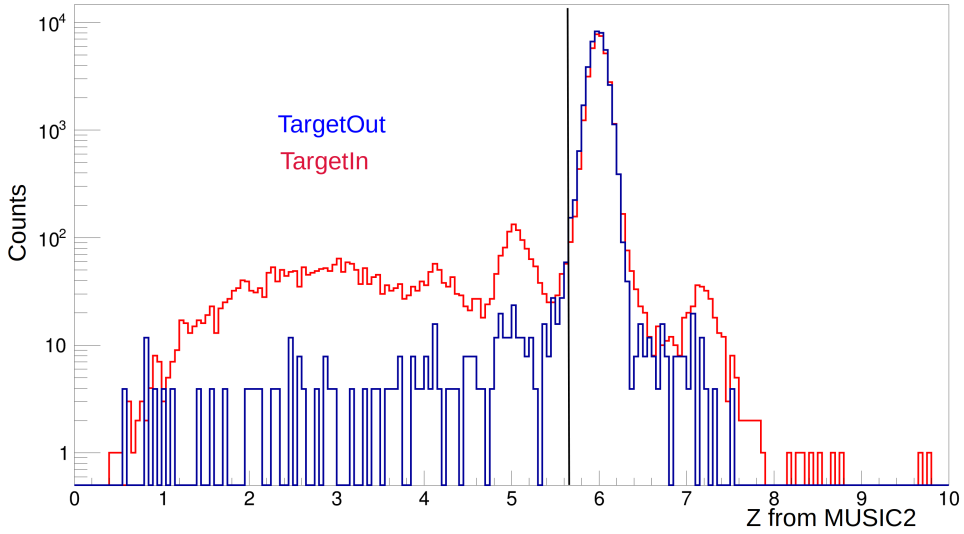

Figure 4.21: Z obtained from MUSIC2 spectrum with the target (red) and without the target (blue) for ^{22}C.

4.6.3 Primary beam ^{48}Ca

The procedure of the selection of $N_{out \geq Z}$ particles described above was followed for the primary beam analysis (^{48}Ca). Figure 4.22 shows the energy loss spectrum with the incident beam selection of ^{48}Ca shown in Figure (4.19). The Z identification spectrum represents the target–out (black) and target–in measurements, where the target–out

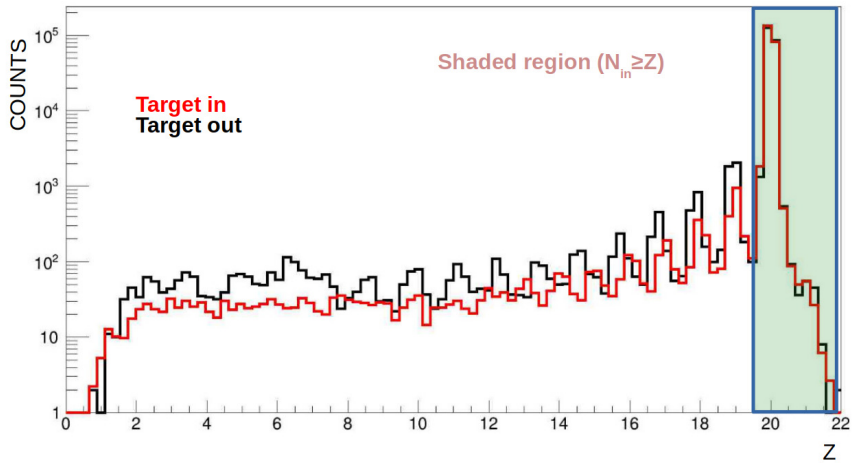

Figure 4.22: MUSIC2 (Z) spectrum for the target–out and target–in measurements.

spectrum is normalized to target–in spectrum (red). The ($N_{out\geq Z}$) selection area is shown by the shaded region for $Z = 20$ peak.

4.6.4 Functions used for counting the $N_{out\geq Z}$

Two different functions (Gaussian and GausExp) were used to determine the lower limits (3.5σ) on the Z (peak) of the desired isotope for $N_{out\geq Z}$ particles for all the isotopes (^{20,22}C, ^{48}Ca). One of the isotopes (^{20}C) Z-identification spectra is shown in Figures (4.23, 4.24). Figure 4.23 shows the fitting of $Z = 5, 6$ using a new function

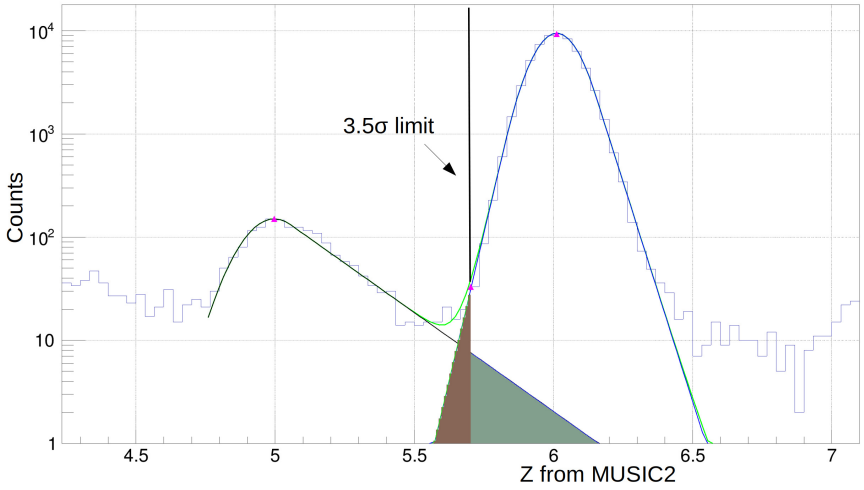

Figure 4.23: MUSIC2 (Z) spectrum for the target-in measurements of ^{20}C fitted using the "GausExp" function.

termed as "GausExp" [124] which consists of four parameters, three from the Gaussian fit and the fourth parameter, k, represents the exponential tail on the lower side of the Gaussian. The x, $\bar{x}$,σ represent the counts, the mean and the standard deviation obtained from the Gaussian fit and k represents the number of standard deviations on the side of the tail where the Gaussian switches to an exponential given by the equation:

$$\begin{aligned} f(x;\bar{x},\sigma,k) &= e^{-\frac{1}{2}\left(\frac{x-\bar{x}}{\sigma}\right)^2}, \qquad for\ \frac{x-\bar{x}}{\sigma} \geq -k \\ &= e^{\frac{k^2}{2}+k\left(\frac{x-\bar{x}}{\sigma}\right)^2}, \qquad for\ \frac{x-\bar{x}}{\sigma} < -k \end{aligned} \tag{4.19}$$

The $Z = 6$ peak's 3.5σ region is needed to set a lower limit for counting the $N_{out \geq Z}$ particles, which is 6 in this case. Boron isotope ($Z = 5$) is fitted to estimate the contamination level in the limits set for counting the $Z = 6$ particles. The green-filled region shows the contamination from $Z = 5$ isotope and the brown-filled region shows $Z = 6$ outside the counting region of 3.5σ. The counts from the brown region ($Z = 6$) are added and the counts from the green region ($Z = 5$) are subtracted from the $N_{out \geq Z}$ particle counts before the final cross-section is determined. The Gaus-

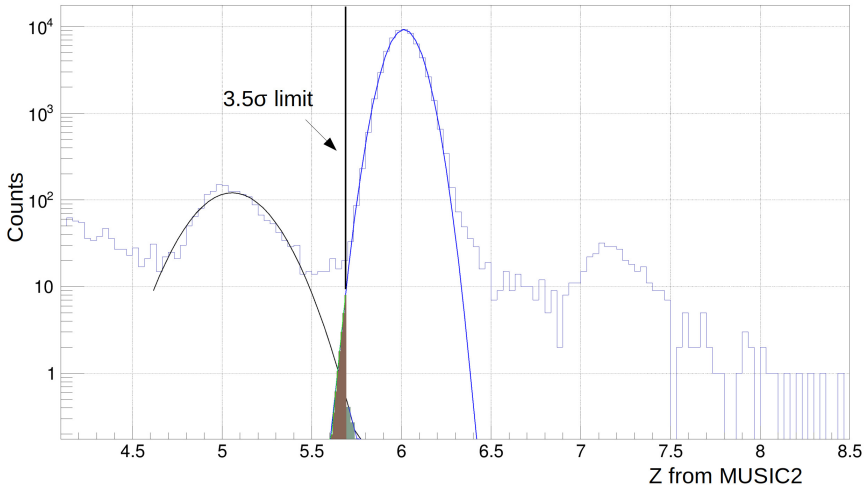

Figure 4.24: MUSIC2 (Z) spectrum for the target-in measurements of ^{20}C fitted using the Gaussian function.

sian function was also used to fit the Z identification spectrum. The 3.5σ lower limit

found using these two functions were the same. But, the "GausExp" provides a better description of $Z = 5, 6$ in the Z spectrum generated by the MUSIC2 detector. Therefore, the "GausExp" function is used for counting the $N_{out \geq Z}$ particles. These functions were also used to estimate the contamination level from the lower Zs in the counting region. The estimated contamination from $Z = 5$ is of the order of 8×10^{-4} obtained from the "GausExp" function for ^{20}C. The $Z = 6$ counts missing from the lower limit of 3.5σ region are of the order of 6×10^{-4} for ^{20}C. On the other hand, the estimation of the contamination level using the standard Gaussian function is of the order of 3×10^{-5}. The effect of the contamination from $Z = 5$ and the missing $Z = 6$ counts from the $N_{out \geq Z}$ particles on the final CCCS will be discussed in Chapter 5.

4.7 Phase space selection on the incident particles

All unreacted particles are not transmitted efficiently to F11 due to BigRIPS and ZDS angular and momentum acceptances. Therefore, to select fully transported particles, the phase spaces of incident beam particles are confined by investigating the region of constant transmission ratio for different positions and angles at the various focal planes before the reaction target. The double PPAC detectors in the ZDS spectrometer were used for beam tracking to determine the horizontal (x) and vertical positions (y) of the incident beam with the X angle (A) and Y angle (B) at F9 and F11.

The particles that do not undergo a charge-changing reaction can be represented by the transmission ratio:

$$R_{Tin} = \frac{N_{out \geq Z}}{N_{in}}, \tag{4.20}$$

where N_{in} represents the number of incident particles and $N_{out \geq Z}$ is the number of particles with Z equal to and greater than that of the incident particles after the reaction target. The same equation is used for the target out measurements ($R_{Tout} = \frac{N_{out \geq Z}}{N_{in}}$) to determine the transmission ratio of the incident and the outgoing particles

for the non-target reactions. The position and angle at F9 and F11 are confined by the dependence of R_T. The final selection of the constant region in R_T at each phasespace is made after looking at all the phasespaces and then iteratively going through all the phasespaces upstream after the intial selections.

4.7.1 ^{20}C phase space selection

The transmission ratio R_T, variation is inspected for different phase spaces from the experimental focal plane F9 to the target at F11. The R_T for the Y_{F9} and X_{F9} focal

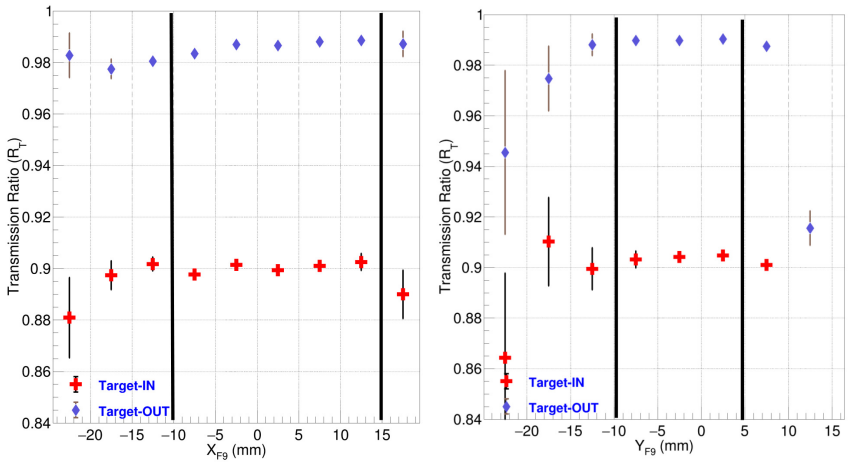

Figure 4.25: Transmission ratio variation for different Y_{F9} and X_{F9} positions.

plane positions determined for different selected regions of the beam position with 5 mm intervals are shown in Figure 4.25. The size of the bin is depicted by the horizontal bars and the statistical uncertainty in R_T is represented by the vertical bars. The determination of statistical uncertainty in R_T will be discussed in the next chapter. The transmission ratios R_{Tout} (blue points) and R_{Tin} (red points) have a constant trend from $X_{F9} = -10$ mm to 15 mm. The constant region of the transmission ratio is shown by the black vertical lines, which is the selected region in both R_{Tout} and R_{Tin} to determine the σ_{cc}. The Y_{F9} position is inspected with the phase space restriction on X_{F9}. Similarly, the angles A_{F9} and B_{F9} at F9 are examined with the phase space restriction selected on X_{F9} and Y_{F9}. The selection regions for F9 phase spaces are

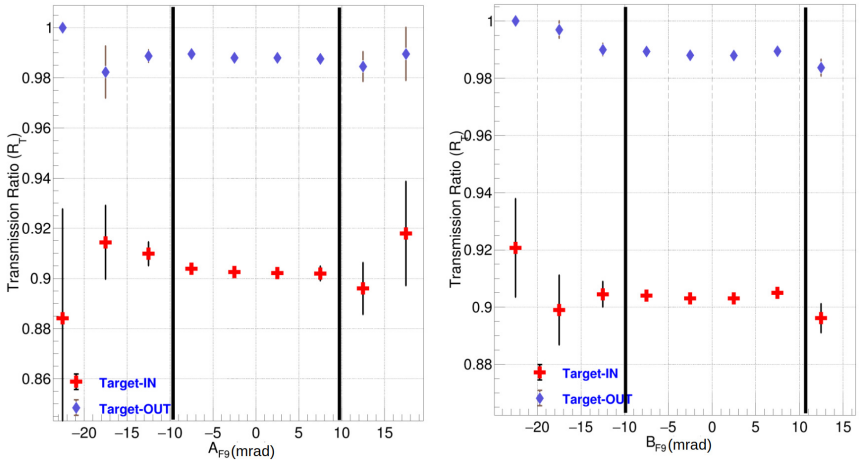

Figure 4.26: Transmission ratio variation for different A_{F9} and B_{F9} angles.

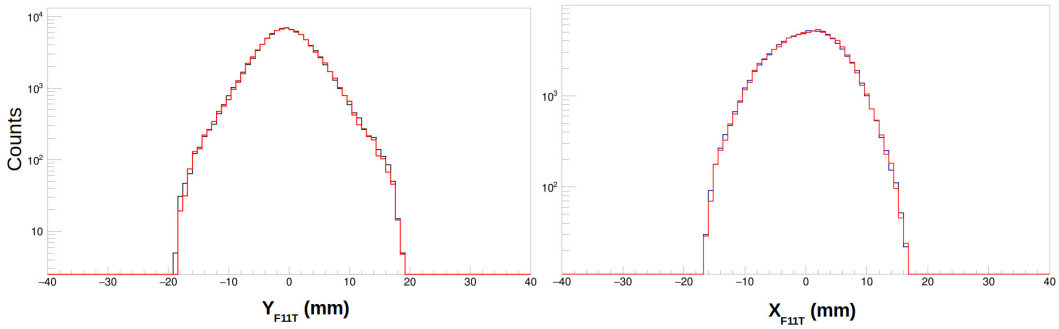

Figure 4.27: (a) $Y11_T$ position of the beam at the target in mm (b) $X11_T$ position of the beam at the target in mm.

shown by black vertical lines in Figures 4.25 and 4.26. The x and y positions of the

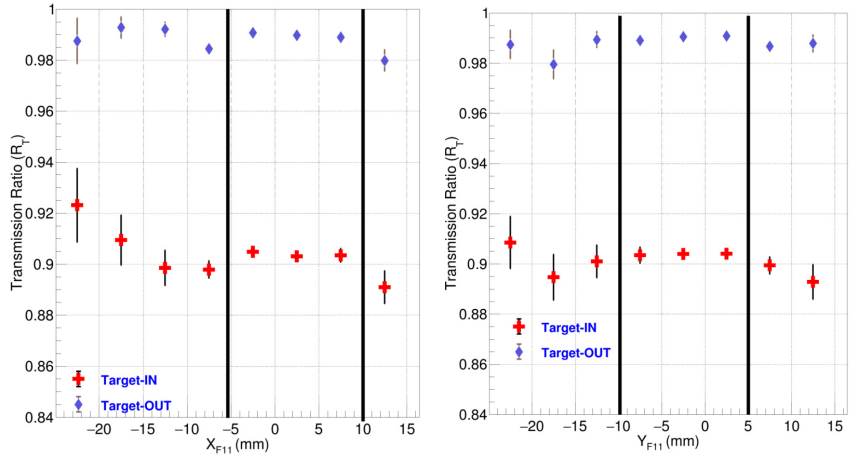

Figure 4.28: Transmission ratio variation for different X_{F11T} and Y_{F11T} positions.

incident beam at the F11 target for the ^{20}C beam are shown in Figure 4.27 where the red histogram represents the target-out measurements and the black histogram represents the target-in measurements.

The transmission ratio variations for the positions and angles at the final focal plane in ZDS are shown in Figures 4.28 and 4.29, respectively.

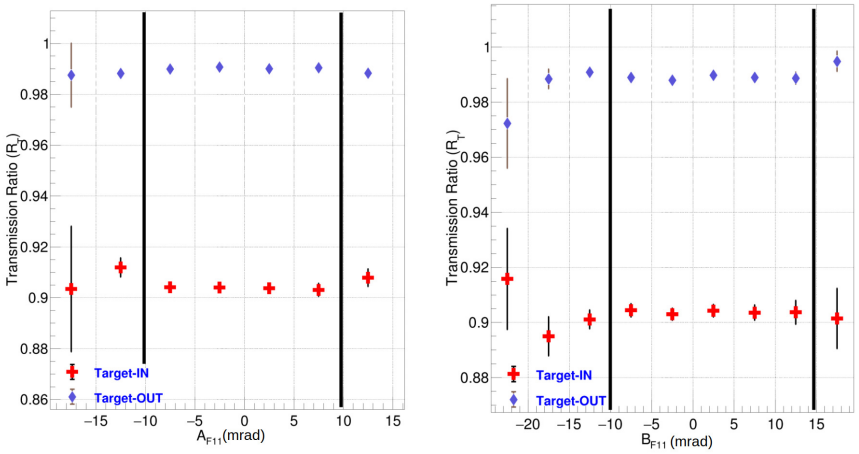

Figure 4.29: Transmission ratio variation for different A_{F11} and B_{F11} angles.

4.7.2 ^{22}C phase space selection

The phase space was restricted for ^{22}C following a similar analysis of transmission variation explained for ^{20}C. The transmission ratios R_T for the position of the incident

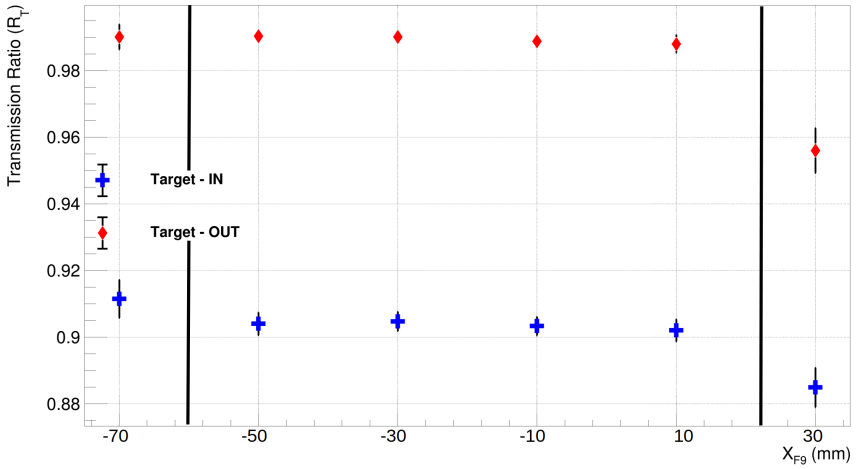

Figure 4.30: Transmission ratio variation for different horizontal positions X_{F9}.

beam at focal plane 9 (Y_{F9}, X_{F9}) with 10 mm intervals are shown in Figures 4.30, 4.31. The bin size is shown by the horizontal bars and the statistical uncertainty in R_T is

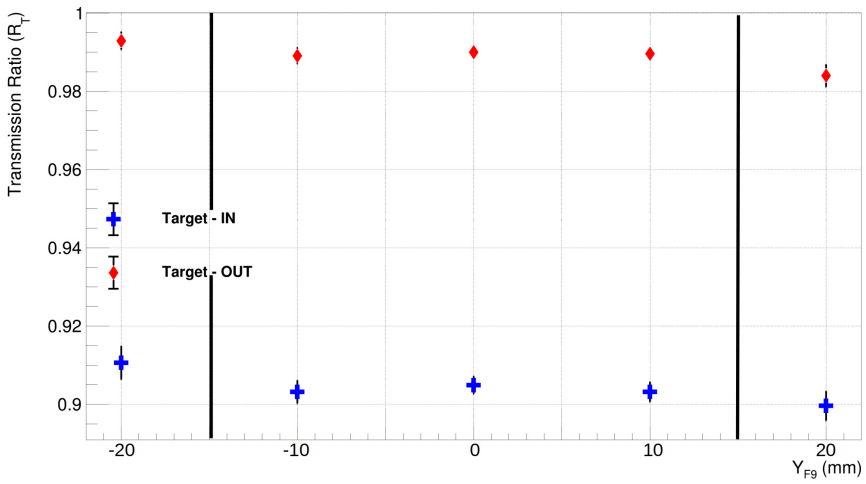

Figure 4.31: Transmission ratio variation for different vertical positions Y_{F9}.

given by the vertical error bar. The transmission ratios R_{Tout} (blue points) and R_{Tin} (red points) have a constant trend from $X_{F9} = -60$ mm to 20 mm. The Y_{F9} position is inspected with the phase space restriction on X_{F9}. The constant region for the vertical position at F9 is from $Y_{F9} = -15$ mm to 15 mm.

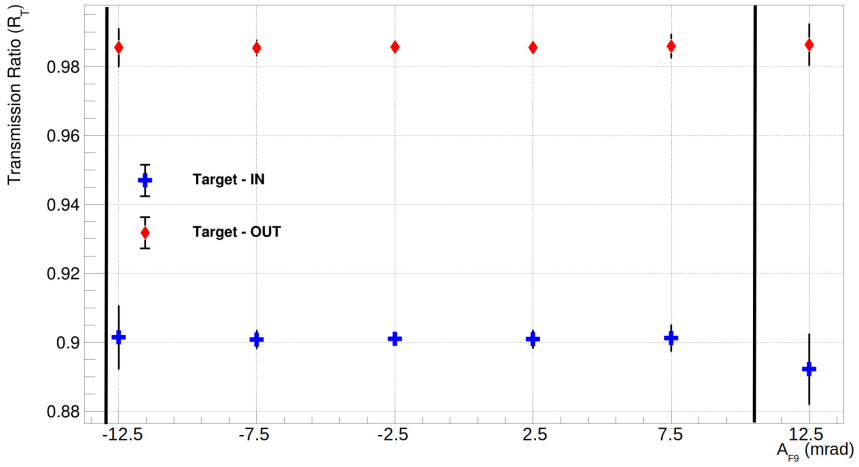

Figure 4.32: Transmission ratio variation for different horizontal angles A_{F9}.

Similarly, the angles A_{F9} and B_{F9} at F9 are examined with the phase space restriction selected on X_{F9} and Y_{F9} shown in Figures 4.32 and 4.33. The constant region for

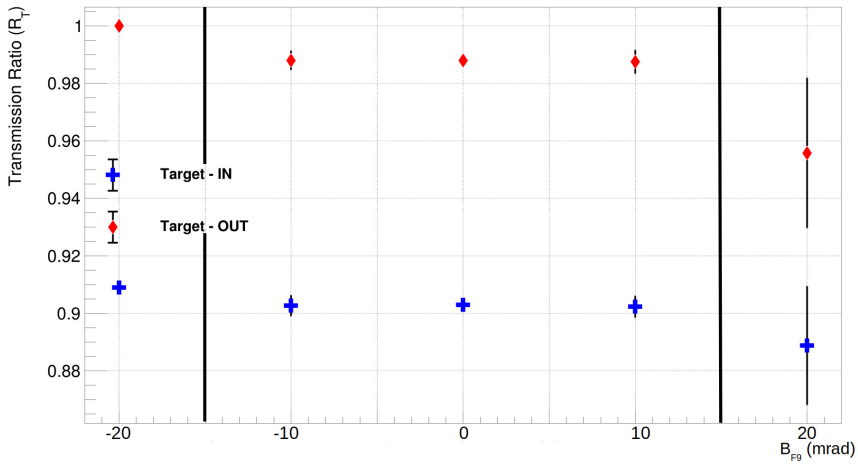

Figure 4.33: Transmission ratio variation for different vertical angles B_{F9}.

the angles at F9 is shown with the black vertical lines.

The transmission ratio variation for X angle at F11 target as shown in Figure 4.32 has 5 mm bin intervals between the selected regions of phase space. The position and angles at the F11 target (X_{F11}, Y_{F11}, A_{F11}, B_{F11}) are examined with the phase space restrictions selected for F9 position and angles. The transmission ratios for F11

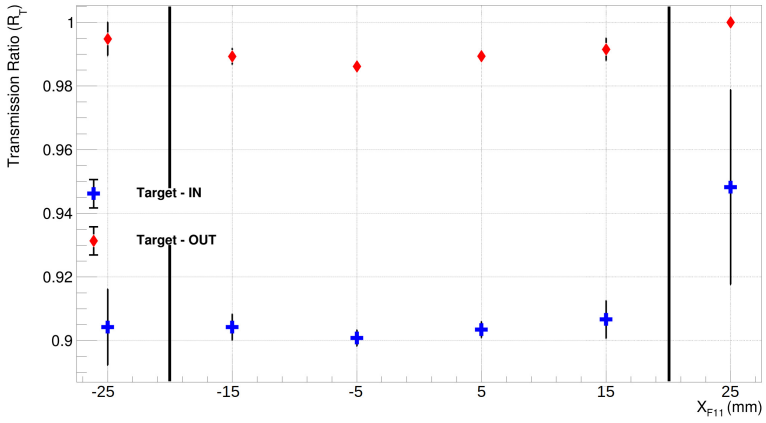

Figure 4.34: Transmission ratio variation for different horizontal positions X_{F11}.

position and angle are shown in Figures 4.34, 4.35, 4.36 and 4.37.

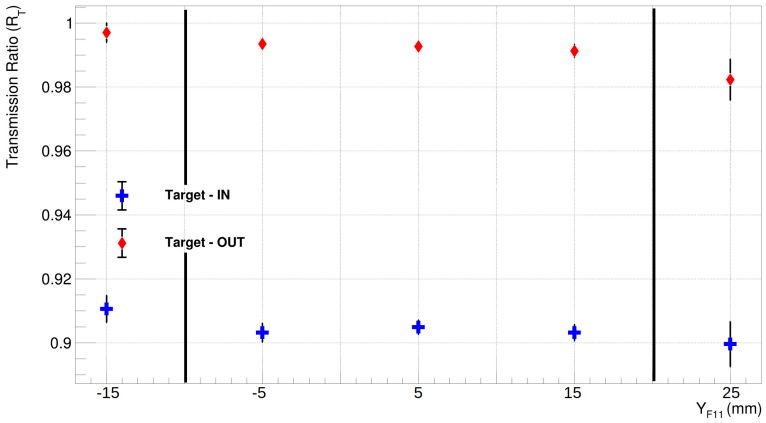

Figure 4.35: Transmission ratio variation for different vertical positions Y_{F11}.

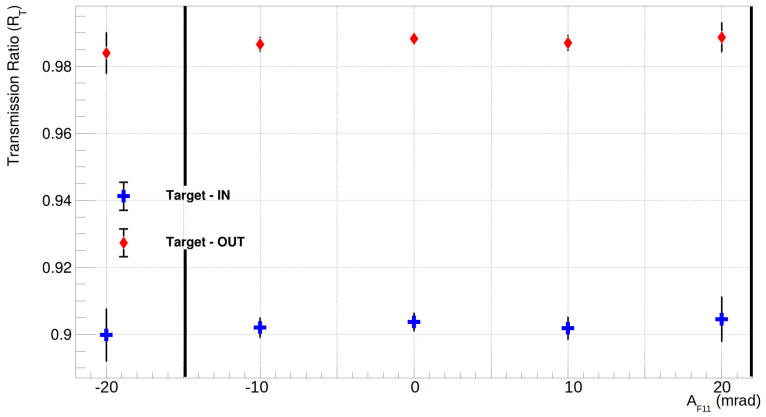

Figure 4.36: Transmission ratio variation for different horizontal angles A_{F11}.

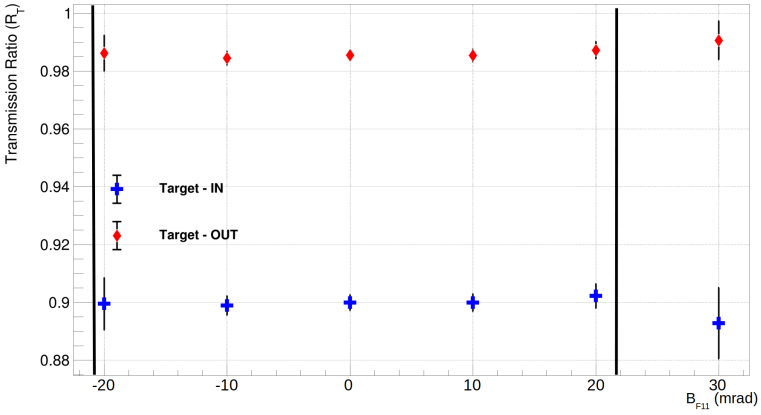

Figure 4.37: Transmission ratio variation for different vertical angles B_{F11}.

4.7.3 Primary beam ^{48}Ca phase space selection

The constant region of the phase space is selected by investigating the transmission ratio variation for the primary beam ^{48}Ca using the same technique. ^{48}Ca phase space

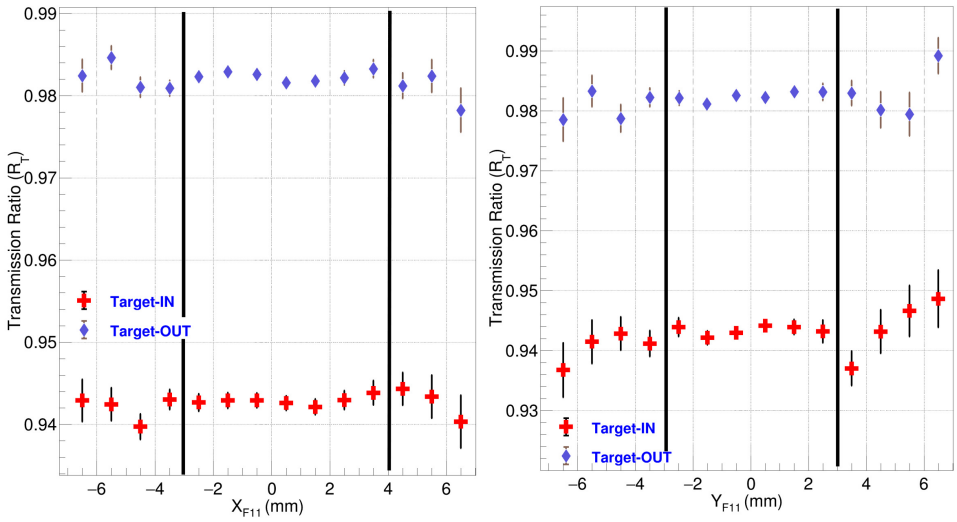

Figure 4.38: Transmission ratio variation for different positions of the incident beam at F11.

was restricted only at focal plane F11 due to the electronic artifacts arising at F9 from PPACs as explained in Section 4.5.1. The R_T variation for the positions of the incident beam at F11 target (X_{F11}, Y_{F11}) with 1 mm intervals is shown in Figure 4.38. The

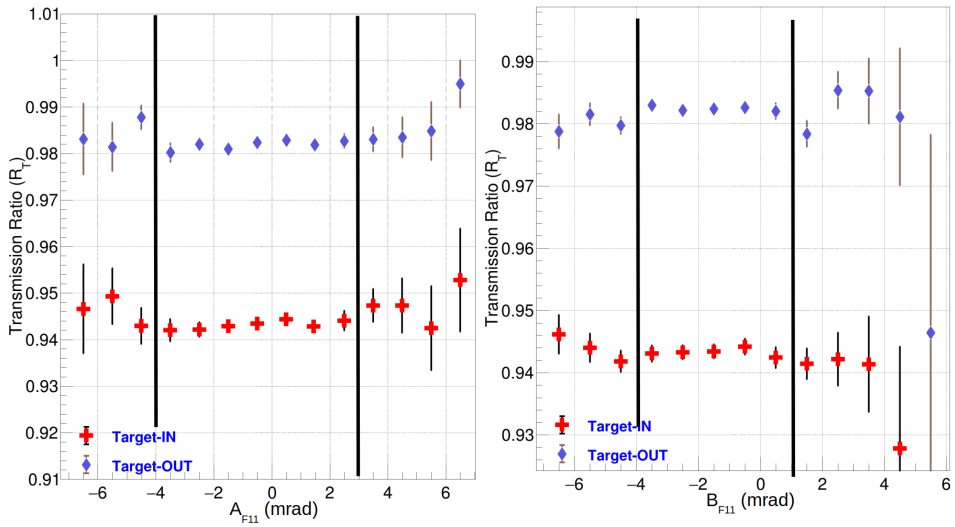

Figure 4.39: Transmission ratio variation for angles of the incident beam at F11.

transmission ratios R_{Tout} (blue points) and R_{Tin} (red points) have a constant trend from $X_{F11} = -3$ mm to 4 mm shown by the black vertical lines. The constant region for the vertical position at F11 is from $Y_{F11} = -3$ mm to 3 mm. The angles A_{F11} B_{F11} at F11 are examined with the phase space restriction selected on X_{F11} and Y_{F11}. The

constant region for the angles at F11 are shown by the vertical lines in Figure 4.39.

The phase space is restricted for all the positions and angles at F9 and F11 for the carbon isotopes and at F11 for calcium. R_{Tin} and R_{Tout} were calculated by integrating over the constant transmission region after implementing the restrictions. The charge changing cross-section is determined using these R_{in} and R_{out} which will be discussed in the following chapter.

Chapter 5

Results and discussion

In this chapter, the results and determination of point proton radii are discussed. The process of determining the σ_{cc} with uncertainties from the transmission ratios is discussed at the beginning. The extraction of proton radii from the measured σ_{cc} using the Glauber model is explained in the following section. Finally, we examine the proton radii as a function of neutron number for the carbon isotopes.

5.1 Charge-Changing cross-section (σ_{cc})

The σ_{cc} is measured based on the transmission technique described in section 3.5, where R_{Tin} and R_{Tout} are the transmission ratios of the incident and the outgoing particles with and without the reaction target, respectively, and t is the number of target atoms per cm^2 described by the equation:

$$t = d \times \frac{N_a}{M_u} \tag{5.1}$$

where $N_a = 6.022 \times 10^{23}$ is Avogadro's number, $M_u = 12.0107u$ is the molar mass of carbon, and d = 2.5 g/cm^2 (and 0.644 g/cm^2) is the areal density of the two carbon reaction targets used during the experiment.

5.1.1 Measured σ_{cc} of carbon isotopes

The transmission ratios R_{Tin} and R_{Tout} are determined for the neutron rich-carbon isotopes (^{20,22}C) integrating over the constant transmission region in the horizontal position (x), vertical position (y), angles A and B at different focal planes as discussed in the previous chapter 4.7. The points shown in green and purple color represent

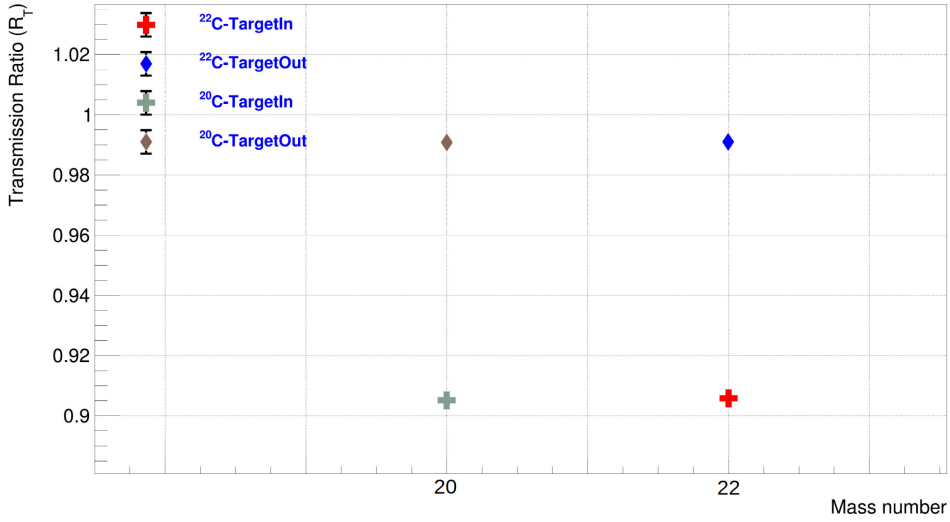

Figure 5.1: Tranmission ratios for Target (In/Out) integrated over the constant transmission region at different focal planes for the carbon isotopes.

R_{Tin} and R_{Tout} of ^{20}C determined from the data for where BigRIPS and ZDS were centered for ^{20}C. The red and blue points represent R_{Tin} and R_{Tout} of ^{22}C determined from the data where BigRIPS and ZDS was centered for ^{22}C. The uncertainties are within the sizes of the symbols in Figure 5.1.

The measured σ_{cc} for ^{20,22}C as a function of the mass number is shown in Figure 5.2. The error bars represent the statistical uncertainty, which is discussed in the following section.

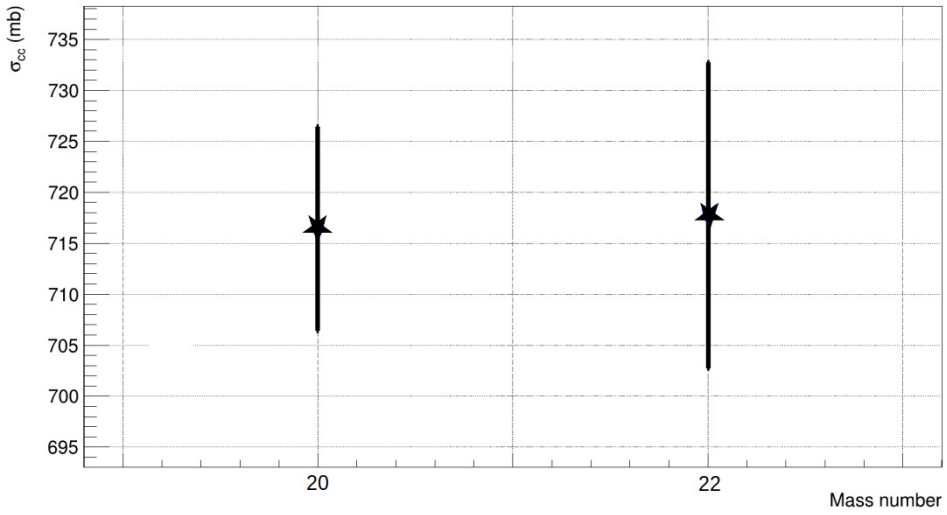

Figure 5.2: Measured charge-changing cross-section (σ_{cc}) of carbon isotopes.

5.2 Uncertainty in the measured charge-changing cross-section

The uncertainty in the σ_{cc} arises from the statistical uncertainty in the number $N_{out\geq Z}$ of events after the target, the target thickness measurement, and the selection region for counting the $N_{out\geq Z}$ events. The systematic and the statistical uncertainties were determined for the σ_{cc} measured for all the isotopes. The number of incident particle events (N_{in}) selected for each isotope explained in section (4.5) has no statistical uncertainty as these counts are from the desired event-by-event selection of the secondary beam. The same Data Acquisition system (DAQ) was used for counting the incident events (N_{in}) and the events after the target ($N_{out\geq Z}$). Therefore, there is no uncertainty related to dead time losses. The particles per second (pps) for ^{20}C and ^{22}C were 300 pps and 15 pps at F11, respectively and much higher for the stable isotope ^{48}Ca. The systematic uncertainty arises from the measurement of the target thickness. The expression used for the statistical and systematic uncertainty will be explained in the following sections.

5.2.1 Statistical uncertainty in σ_{cc}

The statistical uncertainty is the major source of error in this experiment. The standard deviation of the measured charge-changing cross-section for the statistical uncertainty is given by the equation:

$$\Delta\sigma_{cc} = \sqrt{\left(\frac{\partial\sigma_{cc}}{\partial R_{Tin}}\right)^2 \Delta R_{Tin}^2 + \left(\frac{\partial\sigma_{cc}}{\partial R_{Tout}}\right)^2 \Delta R_{Tout}^2} \tag{5.2}$$

where ΔR_{Tin} and ΔR_{Tout} are the standard deviations of the transmission ratios R_{Tin} and R_{Tout}, respectively. The transmission ratio ($R_T = \frac{N_{out\geq Z}}{N_{in}}$) is the ratio of the particles after and before the reaction target, which are part of the statistics. The partial derivatives for R_T are given by:

$$\begin{aligned} \frac{\partial\sigma_{cc}}{\partial R_{Tin}} &= \frac{1}{t}\,\frac{1}{R_{Tin}} \\ \frac{\partial\sigma_{cc}}{\partial R_{Tout}} &= \frac{1}{t}\,\frac{1}{R_{Tout}} \end{aligned} \tag{5.3}$$

The partial derivatives given in Equation (5.3) are substituted in Equation 5.2, and the $\Delta\sigma_{cc}$ can be written as

$$\Delta\sigma_{cc} = \sqrt{\frac{1}{t^2}\left[\left(\frac{\Delta R_{Tin}}{R_{Tin}}\right)^2 + \left(\frac{\Delta R_{Tout}}{R_{Tout}}\right)^2\right]} \tag{5.4}$$

As mentioned in the previous chapter, there is no uncertainty in the counts from the desired selection of the secondary beam. The variance from the binomial distribution is used to obtain the ΔR_{Tout} and ΔR_{Tin}, given by:

$$\left(\frac{\Delta R_{Tin}}{R_{Tin}}\right)^2 = \frac{N_{in}^T R_{Tin}(1-R_{Tin})}{(N_{in}^T R_{Tin})^2} = \frac{1-R_{Tin}}{N_{in}^T R_{Tin}} \tag{5.5}$$

$$\left(\frac{\Delta R_{Tout}}{R_{Tout}}\right)^2 = \frac{1 - R_{Tout}}{N_{in}^{To} R_{Tout}} \tag{5.6}$$

where N_{in}^{T} and N_{in}^{To} represent the incident beam selection of the events for with and without target data, respectively. The denominators in both the Equations 5.5, 5.6 are equal to the events $N_{out\geq Z}^{T}$ and $N_{out\geq Z}^{To}$ after the target for with and without target data, respectively. Substituting for the standard deviations of ΔR_{Tout} and ΔR_{Tin} into Equation 5.4, the statistical uncertainty of the cross-section, $\Delta\sigma_{cc}^{stat}$ is given as:

$$\left(\Delta\sigma_{cc}^{stat}\right)^2 = \frac{1}{t^2}\left[\frac{1 - R_{Tin}}{N_{in}^{T} R_{Tin}} + \frac{1 - R_{Tout}}{N_{in}^{To} R_{Tout}}\right] \tag{5.7}$$

The statistical uncertainties for all the isotopes are discussed in Section 5.4.

5.2.2 Systematical uncertainty in σ_{cc}

The target thickness measurement also has an uncertainty that needs to be considered. The standard deviation of the measured charge-changing cross-section for the systematical uncertainty is given by the equation:

$$\Delta\sigma_{cc} = \sqrt{\left(\frac{\partial\sigma_{cc}}{\partial t}\right)^2 \Delta t^2} \tag{5.8}$$

Δt is the standard deviation in the measurement of the target thickness, which is the systematic uncertainty in the measured σ_{cc}. The partial derivative is given by:

$$\frac{\partial\sigma_{cc}}{\partial t} = \frac{1}{t^2} \ln\frac{R_{Tout}}{R_{Tin}} \tag{5.9}$$

Substituting Equation 5.9 into Equation 5.8 gives:

$$\frac{\Delta\sigma_{cc}}{\sigma_{cc}} = \sqrt{\left(\frac{1}{t}\ln\frac{R_{Tout}}{R_{Tin}}\right)^2 \left(\frac{\Delta t}{t}\right)^2} \tag{5.10}$$

Substituting Equation 3.8 into 5.10, the systematical uncertainty of the cross-section, $\Delta\sigma_{cc}^{syst}$ is given as

$$\left(\frac{\Delta\sigma_{cc}^{syst}}{\sigma_{cc}}\right)^2 = \left(\frac{\Delta t}{t}\right)^2 \tag{5.11}$$

The C reaction target (2.5 g/cm^2) used for the carbon isotopes at F11 was measured to have a thickness of 13.704 mm with a standard deviation of $\Delta t = 0.014$ mm. The second C reaction target (0.644 g/cm^2) used for the calcium isotope at F11 was measured to have a thickness of 3.53 mm with a standard deviation of $\Delta t = 0.0086$ mm. The standard deviation found for the target thickness is substituted into Equation 3.8 to find Δt. The systematic uncertainties for different isotopes are given in the final table of charge-changing cross-sections 5.2.

5.2.3 Total uncertainty of the measured σ_{cc}

The total uncertainty of the charge-changing cross-section is given by the standard deviations of systematic $\Delta\sigma_{cc}^{syst}$ and statistical uncertainties $\Delta\sigma_{cc}^{stat}$:

$$\Delta\sigma_{cc}^{total} = \sqrt{\left(\frac{\partial\sigma_{cc}}{\partial R_{Tin}}\right)^2 \Delta R_{Tin}^2 + \left(\frac{\partial\sigma_{cc}}{\partial R_{Tout}}\right)^2 \Delta R_{Tout}^2 + \left(\frac{\partial\sigma_{cc}}{\partial t}\right)^2 \Delta t^2} \tag{5.12}$$

The partial derivatives of N_t, R_{Tin} and R_{Tout} given in the previous sections are used to get the total $\Delta\sigma_{cc}$:

$$\frac{\Delta\sigma_{cc}^{total}}{\sigma_{cc}} = \sqrt{\left[\left(\frac{\Delta R_{Tin}}{R_{Tin}}\right)^2 + \left(\frac{\Delta R_{Tout}}{R_{Tout}}\right)^2\right]\left(\ln\frac{R_{Tout}}{R_{Tin}}\right)^{-2} + \left(\frac{\Delta t}{t}\right)^2} \tag{5.13}$$

Substituting the variance of ΔR_{Tout} and ΔR_{Tin} in Equation 5.13. The total uncertainty is given by :

$$\left(\frac{\Delta\sigma_{cc}^{total}}{\sigma_{cc}}\right)^2 = \left[\frac{1-R_{Tin}}{N_{in}^T R_{Tin}} + \frac{1-R_{Tout}}{N_{in}^{To} R_{Tout}}\right]\left(\frac{1}{\sigma_{cc} t}\right)^2 + \left(\frac{\Delta t}{t}\right)^2 \tag{5.14}$$

The estimated total uncertainty is given in the final table of charge-changing cross-sections 5.2.

5.2.4 Uncertainty from the $N_{out} < Z$ in the $N_{out \geq Z}$ events

The $N_{out \geq Z}$ events after the target were counted by setting a lower limit on the 3.5σ region around the mean position of the Z of interest. $N_{out \geq Z}$ are the events that did not interact with the protons of the incident beam. As discussed in the previous Chapter 4, the selection of these events also contains some contamination from the lower Z and missing events from the Z of interest. The contribution from the lower Z events leads to an uncertainty in the determination of the σ_{cc}. Figure 5.3 shows the Z spectrum

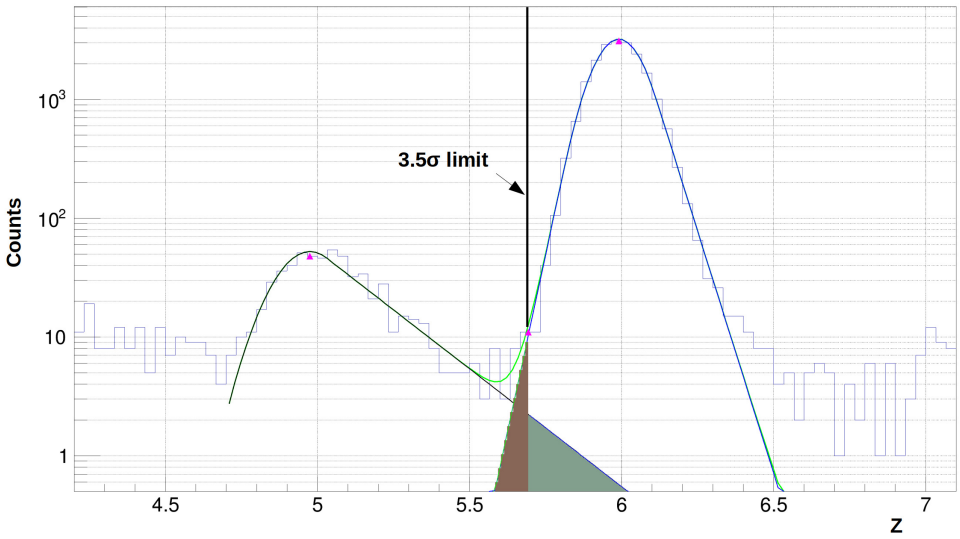

Figure 5.3: MUSIC2 (Z) spectrum for the target-in measurements of ^{22}C fitted using the "GausExp" function.

obtained from MUSIC2 fitted using the "GausExp" function for the ^{22}C data. The vertical limit shows the 3.5σ region selection for $Z = 6$. The estimated contamination shown by the green shaded region in Figure 5.3 for the with target data from $Z = 5$ (Z^{cont}) is 7×10^{-4}. The contamination level estimated for the without target data is 5×10^{-4}. The uncertainty in the measured charge-changing cross-section , $\Delta\sigma_{cc}^{cont}$ was estimated to be $\pm$ 2.80 mb in the measured σ_{cc} of ^{22}C.

As can be seen in Figure 5.3, the peak of interest, $Z = 6$, has non-negligible counts shown by the brown shaded region (Z^{add}) outside the lower limit set for counting the $N_{out} \geq Z$ particles. Therefore, these counts should be added to the $N_{out} \geq Z$ counts. The absolute value of σ_{cc} is determined using the transmission ratios, $R_{Tin} = \frac{N_{out \geq Z}}{N_{in}}$ as discussed in Section 5.1. The transmission ratio equation is modified to take into account the contamination from $Z = 5$ and the addition of $Z = 6$ events in $N_{out \geq Z}$:

$$N^{*}_{out \geq Z} = N_{out \geq Z} \ + (Z^{add} - Z^{cont}) \tag{5.15}$$

The modified equation for the transmission ratio $R_{Tin} = \frac{N^{*}_{out \geq Z}}{N_{in}}$ was used for determining the transmission ratio. The uncertainty in the measured charge-changing cross-section, $\Delta\sigma_{cc}^{add}$, was estimated to be $\pm$ 2.20 mb if $Z = 6$. The contamination from the lower Z, $\Delta\sigma_{cc}^{cont}$, and the counts for the peak of interest outside the lower limit, $\Delta\sigma_{cc}^{Zadd}$, for each isotope are discussed in Section 5.4.

5.3 Incident beam energies before the reaction target

As discussed in the previous chapter, the velocities of the incident particles were measured using the plastic detectors. The velocities (β) of the particles was determined by the plastic scintillators at F11 and F8 (F7). The flight paths for all the isotopes are listed in Table 4.1. β determined for the flight path between the plastic scintillators ($PS_{11} - PS_{8}$) for ^{20}C is shown in Figure 5.4. The mean value of the peak is 0.5955, which is 228A MeV in terms of energy. The energy lost by the incident particle between the plastic detector (PS_{11}) and the reaction target at F11 was calculated using the LISE++ [125].

The total energy lost by the incident particle was subtracted from the $E = 228A$ MeV measured at PS_{11} in order to obtain the beam energy before the target. The energies for different isotopes are given in Table 5.1.

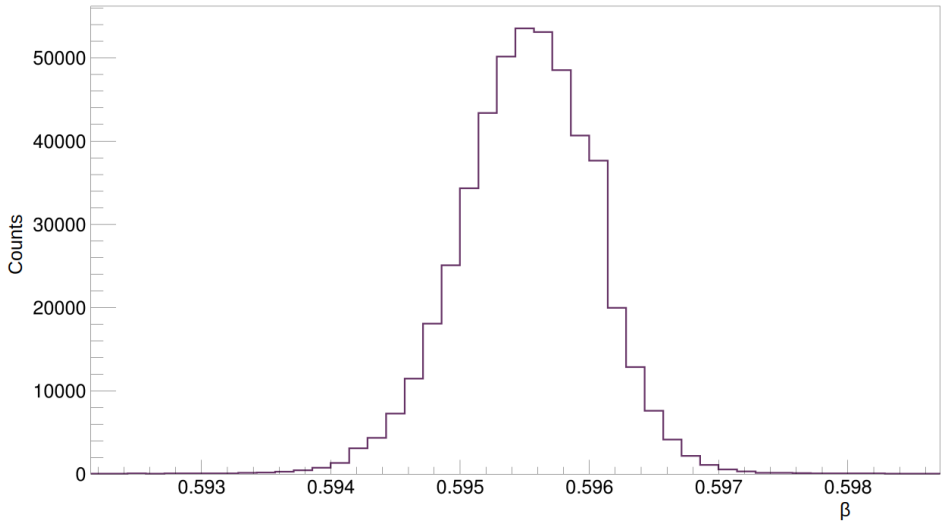

Figure 5.4: Velocity measured for the ^{20}C particles at F11PL.

Table 5.1: Beam energy for different isotopes at F11.

		E/A in MeV		
Isotope	Flight Path	At PS_{11}	Before the target	At Mid-target
^{20}C	$PS_{11} - PS_8$	228	219	211
^{22}C	$PS_{11} - PS_8$	210	200	192
^{48}Ca	$PS_{11} - PS_7$	316	300	291

5.4 Charge-changing cross-section σ_{cc} of different isotopes

The σ_{cc} determined for different isotopes with their uncertainties, and the incident beam energy before the target are listed in Table 5.2. The absolute values of the mea-

Table 5.2: Charge-changing cross-sections with uncertainties.

Isotope	E/A	σ_{cc}	Statistical	Systematic			Total
	MeV		$\Delta\sigma_{cc}^{st}$	$\Delta\sigma_{cc}^{cont}$	$\Delta\sigma_{cc}^{add}$	Δt	$\Delta\sigma_{cc}^{total}$
		mb					
^{20}C	219	716	10	2.9	2.5	0.73	10
^{22}C	200	718	15	2.8	2.4	0.73	15
^{48}Ca	300	1261	26	0.3	0.2	3.0	27

sured σ_{cc} of the neutron-rich carbon isotopes are almost the same as shown in Table 5.2. The σ_{cc} of ^{48}Ca was recently measured by Tanaka *et al.* [126] on a carbon target at around 280A MeV. The absolute σ_{cc} of ^{48}Ca reported in Ref. [126] is 1259 (14) mb which is similar to the cross-section determined in this experiment within the un-

certaintites. The proton radii are determined using the finite range Glauber model. Point proton root mean square (rms) radii determination from σ_{cc} is discussed in the following section.

5.5 Point proton radii from the measured σ_{cc}

The evolution of the experimentally determined point proton distribution radii for an isotopic chain is the testing ground for the state-of-the-art nuclear (*ab initio*) theory. The finite range Glauber model described in Section 2.6.1 is used to determine the proton distribution radii. The target nucleus (^{12}C) density distribution is well known. Therefore, in Equation 2.16, the $P_{cc}(b)$ depends only on the projectile's proton density. Harmonic-oscillator (HO)-type density distribution [127,128] is assumed for both the projectile and the target for deriving the proton distribution radii (R_p) from the σ_{cc}. The σ_{cc} calculated for five different HO width parameters of density distribution with different R_p are shown in Figure 5.5. The linear fit of R_p corresponding to the calculated σ_{cc} is shown by the red line. The σ_{cc} determined for ^{22}C = 718 $\pm$ 15 mb is

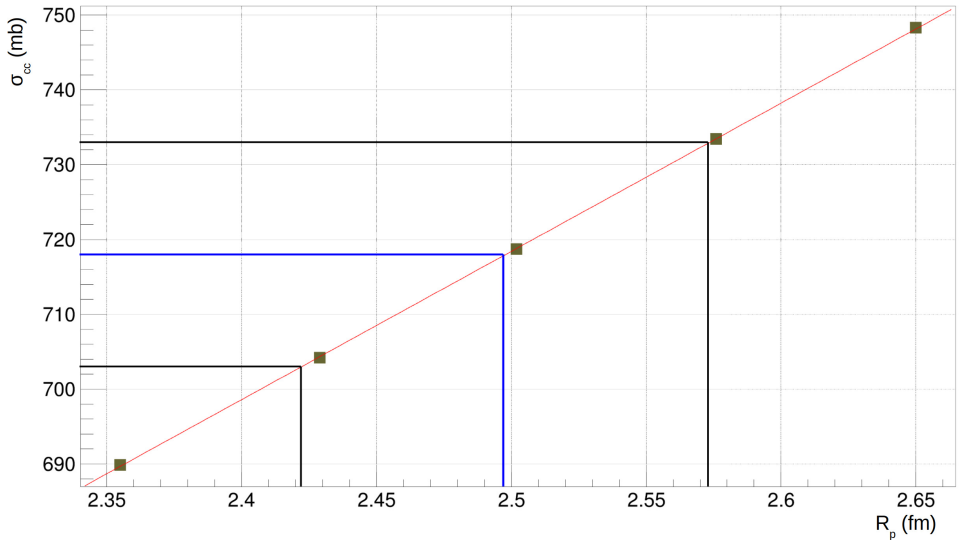

Figure 5.5: The σ_{cc} calculated for ^{22}C using five different HO width parameters of the density distributions with different R_p is represented by the green squares. The blue lines show the proton radii corresponding to the central value of the measured σ_{cc}. The black lines represent the proton radii corresponding to the uncertainty of the measured σ_{cc}. The linear fit is shown by the red line.

shown by the horizontal blue line. The R_p of ^{22}C corresponding to the determined σ_{cc} is given by the vertical blue line. The proton radii of ^{20}C and ^{48}Ca are extracted using the same method. The proton radius of Borromean nucleus, ^{22}C, has been determined experimentally for the first time. The absolute values of the extracted proton radius (R_p) from the σ_{cc} of all the isotopes are shown in Table 5.3. The central values of the proton radii of ^{22}C and ^{20}C varies by less than 3% and within uncertainties they are similar.

Table 5.3: Proton radii R_p extracted from the measured σ_{cc}.

Isotope	R_p^{exp} (fm)	$R_p^{e^-}$ (fm)
^{48}Ca	3.44 (8)	3.451 (9) [127]
^{20}C	2.54 (5)	
^{22}C	2.50 (8)	

5.6 Spatial correlation between proton and matter radii

The matter radii of the neutron-rich carbon isotopes (^{20,22}C) are known from the interaction cross-sections measured on a carbon target [26]. The interaction cross-section determined for ^{22}C is significantly larger than ^{20}C, supporting the presence of a two-neutron halo in ^{22}C. The neutron radii (R_n) of ^{20,22}C can be determined using the matter radii together with the proton radii. R_n can be determined from the following equation:

$$A(R_m^2) = Z(R_p^2) + N(R_n^2) \tag{5.16}$$

The neutron skin thickness defined as the neutron-proton rms radius difference, $\Delta R_{np} = R_n - R_p$, is determined from R_n and R_p. The proton R_p^{exp} and matter radii R_m^{exp} from Ref [46] have been used to determine the neutron skin thickness for $^{12-19}$C shown by the blue squares in Figure 5.6. The R_p^{exp} of ^{20,22}C together with the matter radii [26] is used to determine the neutron skin thickness of these neutron-rich carbon isotopes. The neutron skin thickness is rapidly increasing, approaching the neutron-drip line

as discussed in Section 2.4.2. The neutron skin ΔR_{np} of 1.23 $\pm$ 0.20 fm for the two-neutron halo, ^{22}C, shows the presence of a thicker neutron surface in this nucleus compared to the one neutron halo, ^{19}C, as shown in Figure 5.6. The green dashed lines represent the relativistic-mean field (RMF) calculations [29] and the red line shows the radii calculated from the dynamical model [31].

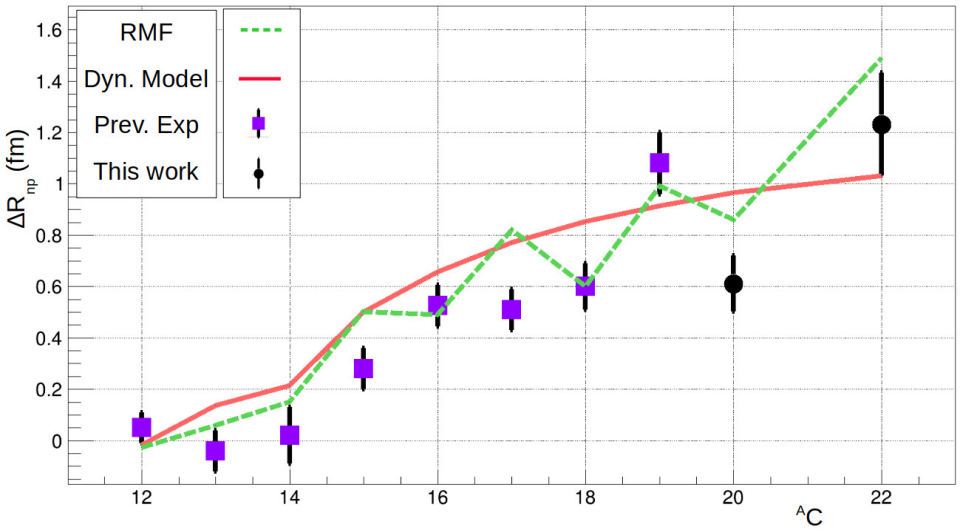

Figure 5.6: The neutron skin thickness determined from the measured R_p^{exp} ($^{12-19}$C [46]) and the measured R_m^{exp} [26]. The RMF [29] and dynamical model calculations [31] are shown by the green-dashed and red lines, respectively.

The dynamical model was used to improve the wave functions described by the Slater determinant from a phenomenological mean-field potential. This model is generated by eliminating the effect of center-of-mass motion. The neutron skin thickness determined from the densities found from the dynamical version is larger than the experiment. For example, the dynamical version of the core+n model used for ^{17}C is not very realistic and needs further sophistication of the structure model. The RMF calculations done in terms of the relativistic-impulse approximation (RIA) determine the distribution which are hadron densities in relativistic expression. The results provided by RMF reproduce the trend for most of the carbon isotopes qualitatively. Although the RMF overestimates for ^{15,17}C it better matches the trend of carbon isotopes than the dynamical model.

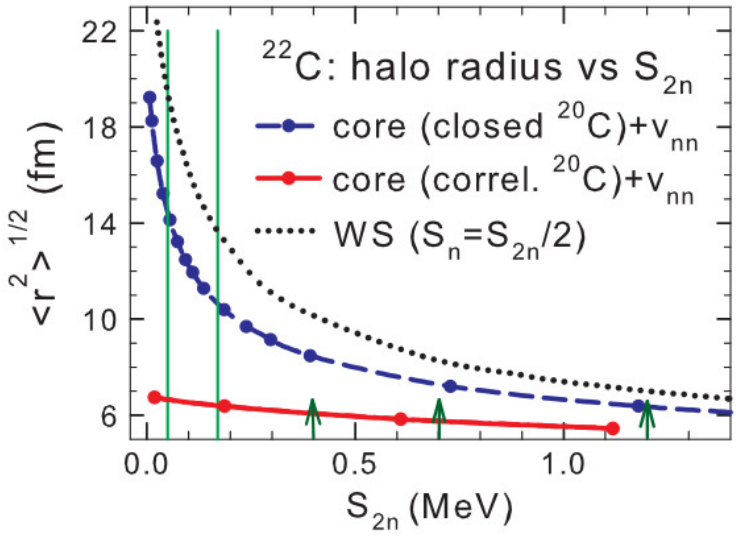

Figure 5.7: The rms radius of the halo neutrons as a function of two-neutron separation energy S_{2n}. The results obtained from the closed-shell core (^{20}C) approach is shown by the blue dashed line and filled circle. The correlated core approach is shown by red line and filled circle. The Woods-Saxon potential with μ_{nn} is shown by the black-dotted line. The range of S_{2n} is denoted by the green vertical lines [130]. Green arrows denote the S_{2n} determined by Kobayashi *et al.* [20]. Figure taken from [129].

The halo radius of the Borromean nucleus, ^{22}C is determined from the matter and proton radii of the halo nucleus and its core nucleus as discussed in Section 2.3. A large root-mean square halo radius of 6.6 $\pm$ 1.1 fm is found in ^{22}C which is as large as ^{11}Li. The halo radius was found to be between $\sim$6 fm and $\sim$7 fm for the ^{22}C from the shell-model calculations reported by Suzuki *et al.* [129] as shown in Figure 5.7. The result obtained in this experiment is in agreement with the halo radius ($6.79^{0.70}_{-0.66}$ fm) obtained from the recently measured matter radius [26] and the extended shell-model calculations. The value obtained for the halo radius is small for such small separation energy which can be explained by a simple relation of halo radius > 10 fm for S_{2n} < 0.3 MeV [129].

5.7 Discussion of results

This study is the first attempt to determine the proton radii of neutron-rich carbon isotopes ^{20,22}C experimentally. The Borromean nucleus, ^{22}C is particularly of interest

because of the presence of halo and also having N = 16, which is a new magic number at the neutron-drip line [14, 17, 18, 131]. The charge-changing cross-section σ_{cc} was used to determine the proton distribution radius, which is the cross-sections of all the processes that decreases the proton number of the projectile nucleus.

The R_p of the neutron-rich carbon isotopes (^{20,22}C) are similar within the uncertainties but the radius of ^{20}C is higher than the radii of $^{12-19}$C. The root-mean square

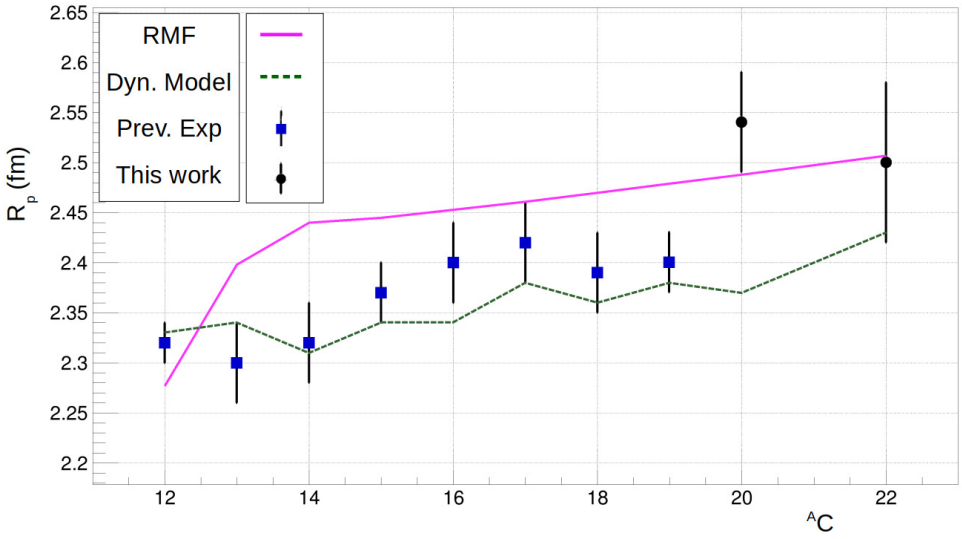

Figure 5.8: Proton radii. The blue-filled squares are the proton distribution radii of $^{12-19}$C from Ref. [46]. The black-filled circles represent the R_p of ^{20,22}C from this experiment. The error bars for the blue-filled squares and black-filled circles include the statistical and systematical uncertainties from the experiment. The pink and the dashed green curve are the predictions from the RMF [29] and the dynamical model [31].

radius of protons predicted using the density distributions from the RMF results, and calculated using RIA are shown by the pink curve [29] in Figure 5.8. The results obtained from the improved version of Slater determinant model (dynamical model) are shown by the the dotted green curve in Figure 5.8 [31]. The dynamical model reproduces the proton radii of carbon isotopes but underestimates the R_p^{exp} of ^{20}C. The RMF calculations show a constant increase of proton radii with the neutron number and overestimate the measured R_p^{exp} of C isotopes except for the ^{20,22}C determined in this experiment. The Dynamical model provides a better description of proton distribution

radii of the C isotopic chain than the RMF model.

The measured proton radius of ^{20}C shows an increase at $N = 14$. This is due to the tensor monopole interaction which is replusive between the protons in the $1p_{3/2}$ orbital and neutrons in the $1d_{5/2}$ orbital. This leads to these orbitals being pushed higher in energy resulting in the disappearance of $N = 14$ shell gap. Therefore, the increase in R_p^{exp} may indicate an absence of a shell gap at $N = 14$ [7]. In oxygen isotopes, this interaction is attractive which gives rise to a new gap of about 4.7 MeV at $N = 14$ between the $1d_{5/2}$ and $2s_{1/2}$ orbitals [32]. The R_p of ^{22}O decreases as a result of this as shown in Figure 5.9 which indicates the presence of a shell gap at $N = 14$ [40]. Typically, the local minima in the radii are the fingerprints for the shell gaps along an isotopic chain [131]. However, they also carry information on the nuclear force. The absence of shell gap at $N = 14$ for the carbon isotope is also supported from the systematics of the 2_1^+ energies investigated by in-beam γ spectroscopy for ^{20}C [32]. The two-neutron removal from the ^{20}C results in a much broader momemtum distribution [20]. A large spectroscopic factor of $C^2S = 3.649$ is observed for the population of $5/2_1^+$ state in ^{19}C. However, it is less than the full occupancy of the $1d_{5/2}$ obital which might indicate the disappearance of the $N = 14$ shell gap.

The systematic study of neutron separation energies (S_n) [14], Q-values, and the energies of the excited state for even-even neutron-rich nuclei showed sharp kinks and confirmed the shell closure at $N = 16$ [17] for the oxygen isotope. The central value of the measured R_p^{exp} of ^{22}C at $N = 16$ does decrease slightly compared to the ^{20}C. The one and two-neutron removal reactions were used to determine the spectroscopic factor of ^{22}C [20] which showed the two final states ($1/2_1^+$, $5/2_1^+$) in the ^{21}C intermediate state having equal contributions to the measured neutron removal cross-sections. The theoretical momentum distribution for ^{22}C two-neutron removal from the $2s_{1/2}$ orbital to ^{20}C is well in agreement with the data supporting the $2s_{1/2}^2$ configuration for the ^{22}C ground state. The large spectroscopic factor ($\sim$1.4) for $2s_{1/2}$

neutron removal to an unbound ^{21}C in Ref. [20] is also suggestive of an extended matter density responsible for the halo formation at ^{22}C [25, 26, 36]. Based on this, there should be a significant decrease in the measured R_p^{exp} of ^{22}C as observed for ^{24}O at

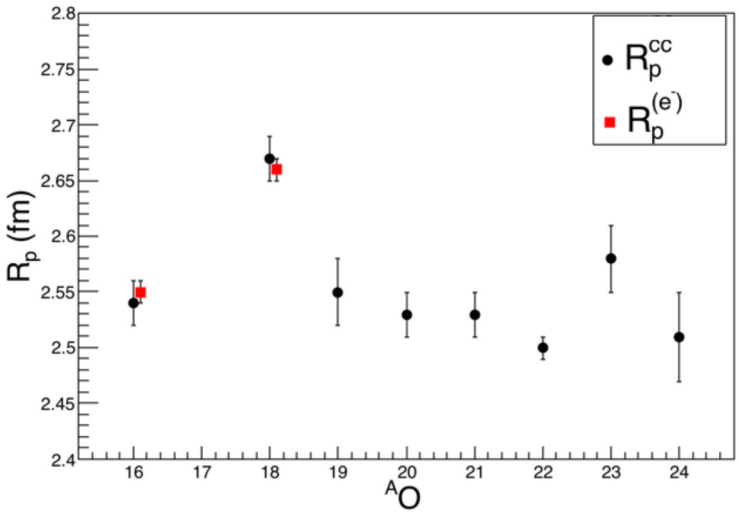

Figure 5.9: Proton radii of oxygen isotopes (black circles). Red squares represent the measurement from e^- scattering experiment. Image taken from Ref. [40].

$N = 16$ with a nearly pure $\nu s^2_{1/2}$ spectroscopic factor [17].

The oxygen isotopes show a different trend for the proton radii at both the shell closures of $N = 14$ and $N = 16$ as shown in Figure 5.9. The proton radii for the oxygen isotopes decrease at $N = 14$ within the uncertainties, which is opposite to the behavior observed for ^{20}C. The local minima in the proton distribution radii along the oxygen isotopic chain was observed at $N = 14$ and $N = 16$ by Kaur *et al.* [40]. But, for the carbon isotopes the R_p increases by 5% for ^{20}C and ^{22}C compared to the $^{12-19}$C isotopes. The increase in proton radii for $N = 14$ may indicate an absence of shell closure for the carbon isotope (^{20}C). The decrease in the point-proton distribution of ^{22}C is not as prominent as observed for ^{24}O at $N = 16$ which might indicate the disappearance of shell closure at $N = 16$. One of the reasons could be the mixture of sd orbitals due to the deformation effects as predicted in Ref. [33]. The recently developed Gamow shell model calculations have predicted the first excited state of

^{22}C, which is also significantly smaller than the one in ^{24}O. This also hints toward the disappearance of the shell closure at $N = 16$ [78].

5.8 Knowledge transfer Plan

This work represents an important step in attaining the first measurement of the proton radius of the two-neutron halo nucleus, ^{22}C. The halo nuclei have been the testing grounds for the development of nuclear models for the system of decoupled protons and neutrons, and the Borromean system. The neutron halos identified in the carbon isotopes are mainly caused by the loosely bound $s-$orbital [2,25,26]. The formation of neutron halos along this isotopic chain is closely connected to the shell evolution and changes of nuclear magicities around drip-lines [7]. As shown in Figure 5.8 the proton radius of ^{20}C is higher than that of ^{19}C. This suggests absence of proton shell closure at $Z = 6$ in ^{20}C, contrary to the discussion in Ref. [37]. The $s-$orbit ($\nu 2s_{1/2}$) is lower than $d-$orbit ($\nu 1d_{5/2}$) in $^{15-19}$C as compared with single particle levels in stable nuclei, as pointed out in Ref. [7]. This inversion results in the formation of one-neutron halo in ^{15}C. The ground state configurations of neutron-rich carbon isotopes ^{16,18,20}C, are mixtures of ($\nu 2s_{1/2}$, $\nu 1d_{5/2}$). The disappearance of the shell gap at $N = 14$ for the carbon isotopes makes the Borromean nucleus, ^{22}C, a key nucleus to investigate if the $N = 16$ shell closure is present or not for this isotopic chain [15, 23, 32].

The proton distribution radii are essential data required for understanding the structure of the halo nucleus. The calibration procedures and the data analysis techniques explained in this thesis can be used in future work on the BigRIPS and ZDS setup (RIKEN) to measure the cross-section of different nuclides. As explained in Section 2, the proton distribution radii of halo nuclei in many cases are enhanced compared to the core nuclei without the halo neutrons [2]. The proton radius of the halo nucleus ^{22}C is similar to that of the core nucleus, ^{20}C, which deviates from the known trend of proton distribution radii in neutron-rich light nuclides. This shows the chang-

ing nature of the new sub-shell closures at these neutron numbers. The proton radii show different behavior at $N = 14$ and $N = 16$ for the carbon isotopes compared to the oxygen isotopes. The increase in proton distribution radii at these shell closures raise intriguing questions on the evolution of proton radii away from stability which poses a major challenge in the search for a unified description of the atomic nucleus.

The neutron skin thickness increases for the neutron-rich carbon isotopes isotopes ^{20,22}C, approaching the neutron drip-line. The halo radius of ^{22}C determined in this experiment agrees with the recent predictions [26,129] and the value obtained is small for such small separation energy based on the simple relation of halo radius > 10 fm for $S_{2n} < 0.3$ MeV [129]. This unusual formation of a two-neutron halo in ^{22}C can be described with the combination of shell evolution and dynamical correlations [7].

Is there a local minimum at $N = 16$ for ^{22}C? This can be answered by performing the charge-changing cross-section measurements for the extremely neutron-rich carbon isotopes with reduced uncertainties. There is an ambiguity in the separation energy S_{2n} of ^{22}C with the new radius measurement of 3.44 (8) fm by Togano $et\ al.$ [4]. To determine whether the $S_{2n} < 0.2$ MeV or it lies closer to the upper limit of S_{2n} $\sim$0.4 MeV needs a more precise measurement of the matter radius of these drip-line carbon isotopes [64].

The method of charge-changing cross-section used in this experiment can also be used for the interpretation of the interstellar production of secondary fragments during cosmic-ray propagation in the galaxy [91]. As explained in section 2.6.1, the direct and indirect method of σ_{cc} were used to determine cross-sections at different incident energies. It was found that at energies $E > 600$ MeV the σ_{pn}^{tot} is smaller than σ_{pp}^{tot} and becomes larger at lower energies [71]. Hence, the nuclear physics involved in these peripheral collisions can be understood from the basic systematics like the energy dependence, charge, and target. The method of calculating σ_{cc} can be used to probe the charge distributions of different neutron-rich isotopes to understand the shell evolu-

tion at the drip-line. The charge-changing cross-section (σ_{cc}) measurement employed in this experiment provides ground for further development of the state-of-the-art $ab\ initio$ nuclear theories and the interactions employed in different calculations.

Bibliography

[1] *CF Von Weizscker, "Zur theorie der kernmassen" Z. Phys. 96, 431 (1935).*

[2] *I. Tanihata et al., "Progress in Particle and Nuclear Physics", 68, 215 (2013).*

[3] *Maria Goeppert Mayer, "On Closed Shells in Nuclei. II", Phys. Rev. 75, 1969 (1949).*

[4] *Maria Goeppert Mayer, "On the "magic numbers" in nuclear structure",Phys. Rev. 75, 1766 (1949).*

[5] *Maria Goeppert Mayer, "The Shell model", Nobel Lectures: Physics, 3 (1963).*

[6] *H. Koura et al., "Nuclidic Mass Formula on a Spherical Basis with an Improved Even-Odd Term", Prog. Theor. Phys., 113 2 (2005).*

[7] *T. Otsuka et al., "Evolution of shell structure in exotic nuclei", Rev. Mod. Phys. 92 (1) 015002 (2020).*

[8] *I. Tanihata et al., "Measurements of Interaction Cross Sections and Nuclear Radii in the Light p-Shell Region", Phys. Rev. Lett. 55, 2676 (1985).*

[9] *I. Tanihata et al., Proc. for Conf. "Radioactive Nuclear Beams", 429 (1989).*

[10] *H. J. Wollersheim, "Limits of Stabiliy:Halo nuclei", IIT Ropar Lecture.*

[11] *C. Thibault et al., "Direct measurement of the masses of ^{11}Li and $^{26-32}$Na with an on-line mass spectrometer", Phys. Rev. C 12, 644 (1975).*

[12] *T. Motobayashi et al., "Large deformation of the very neutron-rich nucleus ^{32}Mg from intermediate-energy Coulomb excitation", Phys. Lett. B 346, 9 (1995).*

[13] *B. V. Pritychenko et al., "Role of intruder configurations in $^{26,28}Ne$ and $^{30,32}Mg$", Phys. Lett. B 461, 322 (1999).*

[14] *A. Ozawa et al., "New Magic Number, N = 16, near the Neutron Drip Line", Phys. Rev. Lett. 84, 5493 (2000).*

[15] *O. Sorlin et al., "Nuclear magic numbers: New features far from stability", Prog. Part. Nucl. Phys. 61 (2) 602-673 (2008).*

[16] *R. Taniuchi et al., "^{78}Ni revealed as a doubly magic stronghold against nuclear deformation", Nature 569, 53-58 (2019).*

[17] *R. Kanungo et al.,"One-neutron removal measurement reveals ^{24}O as a new doubly magic nucleus", Phys. Rev. Lett. 102 (15) 152501-4 (2009).*

[18] *K. Tshoo et al., "N = 16 Spherical Shell Closure in ^{24}O", Phys. Rev. Lett. 109, 022501 (2012).*

[19] *C. R. Hoffman et al., "Evidence for a doubly magic ^{24}O", Phys. Lett. B 672, 17 (2009).*

[20] *N. Kobayashi et al., "One- and two-neutron removal reactions from the most neutron-rich carbon isotopes", Phys. Rev. C 86, 054604 (2012).*

[21] *I. Tanihata, Nuclear Phys. A 682 114c-123c (2001).*

[22] *T. Nagahisa et al., "Examination of the ^{22}C radius determination with interaction cross-sections", Phys. Rev. C 97 (5) 05614 (2018).*

[23] *W. Horiuchi et al., "^{22}C: An s-wave two-neutron halo nucleus", Phys. Rev. C 74 (3), 034311-5 (2006).*

[24] *L. Corragio et al., "Shell-model calculations for neutron-rich carbon isotopes with a chiral nucleon-nucleon potential", Phys. Rev. C 81 (2010) 064303 (2010).*

[25] *K. Tanaka et al., "Observation of a large reaction cross-section in the drip-line nucleus ^{22}C", Phys. Rev. Lett. 104, 062701 (2010).*

[26] *Y. Togano et al., "Interaction cross-section study of the two-neutron halo nucleus ^{22}C", Phys. Lett. B .761, 412 (2016).*

[27] *A. Ozawa et al. "Measurements of interaction cross-sections for light neutron-rich nuclei at relativistic energies and determination of effective matter radii", Nucl. Phys. A691, 599 (2001).*

[28] *R. Sanchez et al., "Nuclear Charge Radii of : $^{9,11}Li$ The Influence of Halo Neutrons", Phys. Rev. Lett. 96, 033002 (2006).*

[29] *K. Kaki et al., "Reaction cross-sections of proton scattering from carbon isotopes (A=8-22) by means of the relativistic impulse approximation", Prog. Theor. Exp. Phys., 093D01 (2017).*

[30] *B. Abu-Ibrahim et al., "Reaction cross-sections of carbon isotopes incident on a proton", Phys. Rev. C 77, 034607 (2008).*

[31] *W. Horiuchi et al., "Systematic analysis of reaction cross-sections of carbon isotopes", Phys. Rev. C 75, 044607 (2007).*

[32] *M. Stanoiu et al., "Disappearance of the N = 14 shell gap in the carbon isotopic chain", Phys. Rev. C 78, 034315 (2008).*

[33] *Xiang- Xiang Sun et al., "Shrunk halo and quenched shell gap at N = 16 in ^{22}C: Inversion of sd states and deformation effects", Phys. Lett. B 785, 530 (2018).*

[34] *P. G. Hansen and B. Jonson., "The neutron halo of extremely neutron-rich nuclei", Europhys. Lett. 4, 4409 (1987).*

[35] *K. Tanaka et al., "Observation of a large reaction cross-section in the drip-line nucleus ^{22}C", Phys. Rev.Lett. 104, 062701 (2010).*

[36] *L. Gaudefroy et al., "Direct mass measurements of ^{19}B, ^{22}C, ^{29}F, ^{31}Ne, ^{34}Na and other light exotic nuclei", Phys. Rev.Lett. 109, 202503 (2012).*

[37] *D. T. Tran et al., "Evidence of Z = 6 'magic number' in neutron rich carbon isotopes", Nature Comm. 9, 1594 (2018).*

[38] *M. Stanoiu et al., "N = 14 and 16 shell gaps in neutron rich oxygen isotopes", Phys. Rev. C 69, 034312 (2004).*

[39] *B. A. Brown et al., "Magic numbers in the neutron rich oxygen isotopes", Phys. Rev. C 72, 057301 (2005).*

[40] *S. Kaur et al.,"Proton Distribution Radii of $^{16-24}O$: Signatures of New Shell Closures and Neutron Skin", Phys. Rev. Lett 129, 142502 (2022).*

[41] *B . Blank et al., "Charge-changing cross-sections of the neutron-rich isotopes $^{8,9,11}Li$", Z. Phys. A - Hadrons and Nuclei 343, 375 (1992).*

[42] *L. -B. Wang et al., "Laser Spectroscopic Determination of the ^{6}He Nuclear Charge Radius", Phys. Rev. Lett. 93, 142501 (2004).*

[43] *A. Estradé et al., "Proton Radii of $^{12-17}B$ Define a Thick Neutron Surface in ^{17}B", Phys. Rev. Lett. 113, 132501 (2017).*

[44] *W. Noerterhauser et al., "Nuclear Charge Radii of $^{7,9,10}Be$ and the One-Neutron Halo Nucleus ^{11}Be", Phys. Rev. Lett. 102, 062503 (2009).*

[45] *S. Terashima et al., "Proton radius of ^{14}Be from measurement of charge-changing cross-sections", Prog. Theor. Exp. Phys. 101D02 (2014).*

[46] *R. Kanungo et al., "Proton Distribution Radii of $^{12-19}C$ week ending Illuminate Features of Neutron Halos", Phys. Rev. lett. 117, 102501 (2016).*

[47] *H. Yukawa et al., "On the interaction of elementary particles", Proc. Phys. Math. Soc. Japan 17, 48 (1935).*

[48] *R. Machleidt and D. R. Entem,"Chiral effective field theory and nuclear forces", Phys. Reports 503, 1 (2011).*

[49] *V. G. J. Stoks et al., "Construction of high-quality NN potential models", Phys. Rev. C 49, 2950 (1994).*

[50] *R. Machleidt, "The High precision, charge dependent Bonn nucleon-nucleon potential (CD-Bonn)", Phys.Rev. C63, 024001 (2001).*

[51] *R. B. Wiringa et al., "Accurate nucleon-nucleon potential with charge-independence breaking", Phys. Rev. C 51, 38 (1995).*

[52] *J. L. Friar et al., "Triton calculations with the new Nijmegen potentials", Phys.Lett., B311, 4 (1993).*

[53] *J.-i. Fujita and H. Miyazawa, "Pion theory of three-body forces", Progress of Theoretical Physics. 17, 360 (1957).*

[54] *L.-B. Wang, "Determination of the using high-resolusion laser ^{6}He nuclear spectroscopy", University of Illinois at Urbuna-Champaign, Ph.D Theses (2004).*

[55] *B. S. Pudliner, "Quantum monte carlo calculations of $A \leq 6$ nuclei", Phys. Rev. Lett. 74 (1995).*

[56] *S. C. Pieper and R. B. Wiringa, "Quantum monte carlo calculations of light nuclei", Annual Review of Nuclear and Particle Science. 51, 53 (2001).*

[57] *S. A. Coon et. al., "The Three-Body Force, Off-Shell Pion Nucleon Scattering, and Binding Energies in Nuclear Matter", Nuclear Phys. A. 242, 467 (1975).*

[58] *S. A. Coon et. al., "The two-pion-exchange three-nucleon potential and nuclear matter", Nuclear Phys. A. 317, 242 (1979).*

[59] *H. T. Coelho et. al., "The two-pion-exchange three-nucleon force and the ^{3}H and ^{3}He nuclei", Phys. Rev. C 28, 1812 (1983).*

[60] *E. Epelbaum et al., "Modern theory of nuclear forces", Phys. 81, 1773 (2009).*

[61] *S. Weinberg et al., "Nuclear forces from chiral lagrangians", Physics Letters B. 251, 288 (1990).*

[62] *St Kistryn and E Stephan, "Deuteron-proton breakup at medium energies", J. Phys. G: Nucl. Part. Phys. 40 063101 (2013).*

[63] *Maria Piarullu and Ingo Tews, "Local Nucleon-Nucleon and Three-Nucleon Interactions Within Chiral Effective Field Theory", Front. Phys. 7, 2296 (2020).*

[64] *J. W. Hammer et al., "Effective field theory description of halo nuclei", J. Phys. G: Nucl. Part. Phys. 44 103002 (2017).*

[65] *Mosby S et al., "Search for ^{22}C and constraints on ^{22}C", Nucl. Phys. A 909 69–78 (2013).*

[66] *M. Hongo et al., "Universal Properties of Weakly Bound Two-Neutron Halo Nuclei", Phys. Rev. Lett, 128, 212501 (2022).*

[67] *J. Vanasse et al., "Charge and matter form factors of two-neutron halo nucle in halo effective field theory at next-to-leading order", Phys. Rev. C 95, 024318 (2017).*

[68] *SK Bogner et al., "From low-momentum interactions to nuclear structure, Prog. Part. Nucl. Phys. 65, 1 (2010).*

[69] *G. R. Jansen et al., "Ab Initio Coupled-Cluster Effective Interactions for the Shell Model: Application to Neutron-Rich Oxygen and Carbon Isotopes", Phys. Rev. Lett. 113, 142502 (2014).*

[70] *B. R. Barrett et al., "Ab initio no core shell model", Prog. Part. Nucl. Phys. 69, 131 (2013).*

[71] *Y. Suzuki et al., "Parameter-free calculation of charge-changing cross-sections at high energy", Phys. Rev. C 94, 011602(R) 2016.*

[72] *R. J. Barlett and M. Musial, "Coupled-cluster theory in quantum chemistry", Rev. Mod. Phys. 79, 291 (2007).*

[73] *J. R. Gour et al., "Coupled-cluster calculations for valence systems around ^{16}O", Phys. Rev. C 74, 024310 (2006).*

[74] *G. Hagen et al., "Coupled-cluster computations of atomic nuclei", Rep. Prog. Phys. 77, 096302 (2014).*

[75] *G. Hagen et al., "Charge, neutron distribution and weak size of the atomic nucleus", Nat. Phys. 12, 186 (2016).*

[76] *Y. Kanada-En'yo, "Proton radii of Be, B, and C isotopes.", Phys. Rev. C 91, 014315 (2015).*

[77] *L. S. Geng et al., "Masses, deformations and charge radii- nuclear ground-state properties in the relativistic mean field model.", Prog. Theor. Phys. 113, 785-800 (2005).*

[78] *B. S. Hu et al., "Ab initio Gamow in-medium similarity renormalization group with resonance and continuum", Phys. Rev. C 99, 061302 (2019).*

[79] *R. Hofstadter et al., "Electron Scattering and Nuclear Structure", Rev. Mod. Phys. 28, 214 (1956).*

[80] *F. -P. Juster, et al., "Tritium Electromagnetic Form Factors", Phys. Rev. Lett. 55, 2261 (1985).*

[81] *F. J. Kline, et al., "Elastic electron scattering from ^{14}C", Nuclear Phys. A 209, 381 (1973).*

[82] *T. Ohnishi et al., "The SCRIT electron scattering facility project at RIKEN RI beam factory", Phys. Scripta T166, 014071 (2015).*

[83] *K. Tsukada et al., "First Elastic Electron Scattering from Facility", Phys. Rev. Lett. 118, 262501 (2017).*

[84] *G. Fricke, et al., "Nuclear ground state charge radii from electromagnetic interactions", At. Data Nucl. Data Table 60 177 (1995).*

[85] *I. Angeli and K. Marinova, "Table of experimental nuclear ground state charge radii: An update", At. Data Nucl. Data Tables 99, 69 (2013).*

[86] *A. Adamczak et al., "Nuclear structure with radioactive muonic atoms", EPJ Web of Conferences 193, 04014 (2018)*

[87] *G. Ewald et al., "Nuclear Charge Radii of ^{8,9}Li Determined by Laser Spectroscopy", Phys. Rev. Lett. 94, 039901 (2005).*

[88] *P. Mueller et al.,"Nuclear Charge Radius of ^{8}He" Phys. Rev. Lett. 99, 252501 (2007).*

[89] *R. F. Garcia Ruiz et al., "Unexpectedly large charge radii of neutron-rich calcium isotopes", Nat. Phys. 12, 594 (2016).*

[90] *D. T. Tran et al., "Charge-changing cross-section measurements of $^{12-16}$C at around 45A MeV and development of a Glauber model for incident energies 10A-2100A MeV" Phys. Rev. C 94, 064604 (2016).*

[91] *W. R. Webber et al., "Individual charge-changing fragmentation cross-sections of relativistic nuclei in hydrogen, helium, and carbon targets", Phys. Rev. C 41, 520 (1990).*

[92] *J. R. Cummings et al., "Determination of the cross sections for the production of fragments from relativistic nucleus-nucleus interactions. I. Measurements", Phys Rev. C 42, 2508 (1990).*

[93] *B. Blank et al., "Charge-changing cross-sections of the neutron-rich isotopes ^{8,9,11}Li", Z. Phys. A - Hadrons and Nuclei 343, 375 (1992).*

[94] *L. V. Chulkov et al., "Total charge-changing cross sections for neutron-rich light nuclei", Nucl. Phys. A 674, 330 (2000).*

[95] *R. J. Glauber, "Lectures in Theoretical Physics", vol.1, ed. W. E. Brittin et al. 1, 315 (1959).*

[96] *Y. Suzuki et al., "Structure and Reactions of Exotic Nuclei", Taylor & Francis, London, (2003).*

[97] *P. J. Karol, "Nucleus-nucleus reaction cross sections at high energies: Soft-spheres model", Phys. Rev. C 11, 1203 (1975).*

[98] *M. Kimura et al., "Deformed-basis antisymmetrized molecular dynamics and its application to ^{20}Ne", Phys. Rev. C 69, 044319 (2004).*

[99] *T. Yamaguchi et al., "Scaling of Charge-Changing Interaction Cross Sections and Point-Proton Radii of Neutron-Rich Carbon Isotopes", Phys. Rev. Lett.107, 032502 (2011).*

[100] *Y. Yano et al., "The RIKEN RI Beam Factory Project: A status report", Nucl. Instrum. Methods Phys. Res. 261, 1009 (2007).*

[101] *T. Kubo at al., "In-flight RI beam separator BigRIPS at RIKEN and elsewhere in Japan", Nucl. Instrum. Methods Phys. Res. 204, 97 (2003).*

[102] *T. Kubo et al., "Status and Overview of Superconducting Radioactive Isotope Beam Separator BigRIPS at RIKEN", IEEE Trans. Appl. Supercond. 17, 1069 (2007).*

[103] *T. Kubo et al., "BigRIPS separator and Zero Degree spectrometer at RIKEN RI Beam Factory", Prog. Theor. Exp. Phys., 03C003 (2012).*

[104] *M. Tanaka, "Determination of nuclear matter radii of Ca isotopes across the neutron magic number N = 28 via interaction cross-section measurements", Osaka University, P.hD Thesis (2018).*

[105] *Y. Mizoi et al., RIKEN Accel. Prog. Rep. 38, 297 (2005).*

[106] *J.P.Dufour et al., "Projectile fragments isotopic separation: Application to the lise spectrometer at GANIL" Nucl. Instrum. Methods Phys. Res., Sect. A 248, 267 (1986).*

[107] *K. -H. Schmidt et al.,"The momentum-loss achromat - A new method for the isotopical separation of relativistic heavy ions" Nucl. Instrum. Methods Phys.Res., Sect. A 260, 287 (1987).*

[108] *A. Ozawa et al., "Nuclear size and related topics", Nuclear Phys. A 693, 32 (2001).*

[109] *H. Kumagai et al., "Delay-line PPAC for high-energy light ions", Nucl. Instrum. Methods Phys. Res. 470, 562 (2001).*

[110] *S. Bagchi et al., "2n Halo unveiled in ^{29}F", Phys. Rev. Lett. 124, 222504 (2020)*

[111] *Bigrips Information, "http://ribf.riken.jp/BigRIPSInfo/".*

[112] *H. Kumagai et al., "Development of Parallel Plate Avalanche Counter PPAC for BigRIPS fragment separator", Nucl. Instrum. Methods Phys. Res. 370, B 717 (2013).*

[113] *G. Charpak and F. Sauli, "MULTIWIRE PROPORTIONAL CHAMBERS AND DRIFT CHAMBERS", Nucl. Instrum. Methods 162 405 (1979).*

[114] *K. Kimura et al., "High-rate particle identification of high-energy heavy ions using a tilted electrode gas ionization chamber", Nucl. Instr. and Meth. A 538, 608 (2005).*

[115] *S. P. Ahlen, "Theoretical and experimental aspects of the energy loss of relativistic heavily ionizing particles", Rev. Mod. Phys. 52, 121 (1980).*

[116] *Mesytec-32 ADC Datasheet, "https://www.mesytec.com/products/datasheets/MADC-32.pdf".*

[117] *K. Wang et al., "Plastic Scintillation Detectors for Time-of-Flight Mass Measurements", Nucl. Instrum. Methods Phys. Res. A 974, 164199 (2020).*

[118] *G. F. Knoll, "Radiation Detection and Measurement", John Wiley & Sons, New Yorl, 2010.*

[119] *J. W. Zhao et al.,"Reaching time resolution of less than 10 ps with plastic scintillation detectors", NIM A, Vol. 823, 41 (2016).*

[120] *Experiment circuit setup, "https://ribf.riken.jp/BigRIPSInfo/".*

[121] *T. Ohnishi et al., "Identification of New Isotopes ^{125}Pd and ^{126}Pd Produced by In-Flight Fission of 345 MeV/nucleon ^{238}U: First Results from the RIKEN RI Beam Factory", J. Phys. Soc. Jpn 77, 083201 (2008).*

[122] *T. Ohnishi et al., "Identification of 45 New Neutron-Rich Isotopes Produced by In-Flight Fission of a ^{238}U Beam at 345 MeV/nucleon", J. Phys. Soc. Jpn 79 073201 (2010).*

[123] *T. Baumann et al., "Longitudinal Momentum Distributions of ^{8}B and ^{19}C:Signatures for One-Proton and One-Neutron Halos", P.hD. Thesis, Darmstadt University (1999).*

[124] *S. Das et al., "A simple alternative to the Crystal Ball function", Thesis submitted (2016).*

[125] *D. Bazin et al., "The program LISE: a simulation of fragment separators", Nucl. Instr. Meth. Phys. Res. A 482 307327 (2002).*

[126] *M. Tanaka et al., "Charge-changing cross-sections for $^{42-51}$Ca and effect of charged-particle evaporation induced by neutron removal reaction", Nucl-ex, arXiv 2111 13340 (2021).*

[127] *H. De Vries et al., "Nuclear charge-density-distribution parameters from elastic electron scattering", At. Data Nucl. Data Tables 36, 495 (1987).*

[128] *B. Abu-Ibrahim et al., "Elastic and Total Reaction Cross Sections of Oxygen Isotopes in Glauber Theory", J. Phys. Soc.Jpn. 78, 044201 (2009).*

[129] *T. Suzuki et al., "Two-neutron "halo" from the low-energy limit of neutron–neutron interaction: Applications to drip-line nuclei ^{22}C and ^{24}O", Phys. Lett. B 753, 199-203 (2016).*

[130] *http://www.nndc.bnl.gov/nudat2/chartNuc.jsp*

[131] *I. Angeli et al., "N and Z dependence of nuclear charge radii", Nucl. Part. Phys. 36 085102 (2009).*